

AD-A124-017

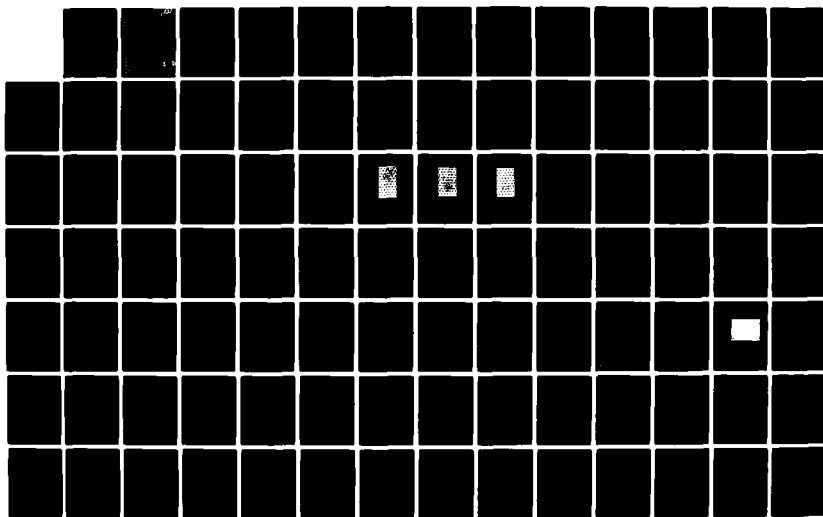
STUDIES OF HEAT TRANSFER IN COMPLEX INTERNAL FLOWS(U)
MINNESOTA UNIV MINNEAPOLIS DEPT OF MECHANICAL
ENGINEERING E M SPARROW JAN 83 N00014-79-C-0621

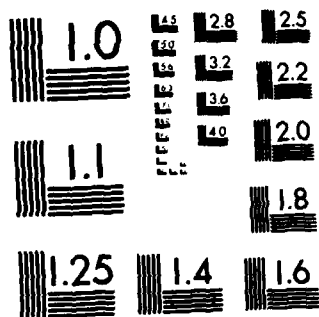
1/2

UNCLASSIFIED

F/G 13/1

NL





MICROCOPY RESOLUTION TEST CHART
NATIONAL BUREAU OF STANDARDS-1963-A

ADA 124017

12

STUDIES OF HEAT TRANSFER IN COMPLEX INTERNAL FLOWS

E. M. Sparrow

Third Summary Report
Contract N00014-79-C-0621
Office of Naval Research

January, 1983

Department of Mechanical Engineering
University of Minnesota
Minneapolis, Minnesota 55455

DTIC
ELECTE
FEB 1 1983
S D

DTIC FILE COPY

DISTRIBUTION STATEMENT A

Approved for public release;
Distribution Unlimited

88 01 31 077

REPORT DOCUMENTATION PAGE		READ INSTRUCTIONS BEFORE COMPLETING FORM
1. REPORT NUMBER N00014-79-C-0621-1983A	2. GOVT ACCESSION NO. AD-A124 017	3. RECIPIENT'S CATALOG NUMBER
4. TITLE (and Subtitle) STUDIES OF HEAT TRANSFER IN COMPLEX INTERNAL FLOWS		5. TYPE OF REPORT & PERIOD COVERED Summary Report Dec.15,1981 to Dec.15,1982
		6. PERFORMING ORG. REPORT NUMBER
7. AUTHOR(s) E. M. Sparrow		8. CONTRACT OR GRANT NUMBER(s) N00014-79-C-0621
9. PERFORMING ORGANIZATION NAME AND ADDRESS Department of Mechanical Engineering University of Minnesota, Minneapolis, MN. 55455		10. PROGRAM ELEMENT, PROJECT, TASK AREA & WORK UNIT NUMBERS Work Unit NR097-437
11. CONTROLLING OFFICE NAME AND ADDRESS Office of Naval Research 800 North Quincy Street Arlington, Virginia 22217		12. REPORT DATE January, 1983
		13. NUMBER OF PAGES 102
14. MONITORING AGENCY NAME & ADDRESS (if different from Controlling Office)		15. SECURITY CLASS. (of this report) Unclassified
		15a. DECLASSIFICATION/DOWNGRADING SCHEDULE
16. DISTRIBUTION STATEMENT (of this Report) Approved for public release; distribution unlimited		
17. DISTRIBUTION STATEMENT (of the abstract entered in Block 20, if different from Report)		
18. SUPPLEMENTARY NOTES		
19. KEY WORDS (Continue on reverse side if necessary and identify by block number) heat exchangers, flow maldistribution, heat transfer coefficient, pressure drop, tube bank, plenum chamber, swirl		
20. ABSTRACT (Continue on reverse side if necessary and identify by block number) Experiments have been performed to determine the heat transfer and pressure drop response of heat exchange devices subject to highly complex fluid flows. Three research problems were undertaken and completed, each dealing with a different aspect of heat exchanger performance. In one case, per-tube transfer coefficients were measured in a tube bank in the presence of an abrupt upstream enlargement of the flow cross section. → cont		

DD FORM 1 JAN 73 1473

EDITION OF 1 NOV 65 IS OBSOLETE
S/N 0102-LF-014-6601

Unclassified

SECURITY CLASSIFICATION OF THIS PAGE (When Data Entered)

Enhancement of the heat transfer was found to occur as a result of the flow disturbances caused by the enlargement. In the second research problem, the effect on heat transfer of the competition between tubes which draw air from a common plenum was investigated. This competition resulted in a skewing of the flow entering the tubes. Significant effects of the skewing occurred when the tubes were relatively close together (pitch \approx 1.5 tube diameters), but for larger spacings the heat transfer coefficients were virtually identical to those for a single tube.

In the last of the problems, the effects of flow maldistribution caused by partial blockage of the inlet of a flat rectangular duct were investigated. Large spanwise nonuniformities of the local heat transfer coefficient were induced by the maldistributed flow. The spanwise-average heat transfer coefficients in the downstream portion of the duct were found to be enhanced due to the flow maldistribution, whereas at more upstream locations a reduction of the coefficients occurred.

Accession For	
NTIS GRA&I	<input checked="" type="checkbox"/>
DTIC TAB	<input type="checkbox"/>
Unannounced	<input type="checkbox"/>
Justification	
By	
Distribution/	
Availability Codes	
Dist	Avail and/or Special
A	



Unclassified

SECURITY CLASSIFICATION OF THIS PAGE (When Data Entered)

INTRODUCTION TO THE REPORT

The heat exchange devices that are employed in power producing systems are subject to highly complex fluid flows whose effect on performance is generally unknown. In this regard, information available in the literature is not readily applicable since, for the most part, it is based on studies of relatively simple flows and of elementary geometrical configurations. Even when more complex devices are studied, only overall data are collected, so that the causes of observed effects have not been identified.

As an example of the encountered flow complexities, attention may be called to the possible maldistribution of the flow delivered to the heat exchanger inlet, a case in point being Navy shipboard heat recovery which utilizes hot gases exhausted from gas turbines. The maldistribution may result from changes in cross section (e.g., sudden enlargement), partial blockages due to valves and other control devices, changes in direction due to bends and elbows, and branching and merging of flow passages. Frequently, more than one of these features occur in a single system. The maldistribution may be accompanied by flow separation, recirculation, and swirl.

Departures from ideal inlet conditions may also occur when parallel flow passages draw fluid from a common plenum and, in the process, compete with each other. Skewing of the flow entering the respective passages will occur unless the plenum is very large, and the skewing will be accentuated if there is any imbalance among the flow rates in the individual passages.

It is interesting to note that the turbulence and mixing inherent in highly complex flows might serve to enhance the overall heat transfer performance. Such an outcome, if true, would be an unexpected dividend, but it would have to be weighed along with the inevitable pressure drop penalty. Whether or not there

is a net enhancement or degradation of heat exchanger performance depends on the conditions under which the system is to be operated. For example, in certain instances, the pressure drop in the heat exchanger may not be a critical factor, as would occur if there were relatively large pressure drops in other portions of the piping circuit. On the other hand, if significant reductions in flow rate are required in response to the larger maldistribution-related pressure drop, then the performance of the heat exchanger may be degraded.

The foregoing discussion serves to motivate and focus the research that is described in this report. The underlying thrust of the work is to deal with problems related to the realities of actual heat exchange devices, where the fluid flow configuration is sufficiently complex that available information is inapplicable. The report describes three research problems on which work was performed and completed during the current reporting period. These problems are

1. Heat transfer in a tube bank in the presence of upstream
cross-sectional enlargement
2. In-tube heat transfer for skewed inlet flow caused by competition
among tubes fed by the same plenum
3. Maldistributed-inlet-flow effects on turbulent heat transfer
and pressure drop in a flat rectangular duct

Journal articles have been prepared for each of these problems. The manuscripts for these articles have been brought together here to form the report for the year's research activities.

HEAT TRANSFER IN A TUBE BANK IN THE PRESENCE
OF UPSTREAM CROSS-SECTIONAL ENLARGEMENT

ABSTRACT

Per-tube heat transfer coefficients were determined in a tube bank in the presence of an abrupt upstream enlargement of the flow cross section. The enlargement occurred either at the inlet face of the tube bank or at the upstream end of a duct which delivered the flow to the inlet. Three different magnitudes of enlargement were investigated along with three lengths of the delivery duct. Axial pressure distributions were measured both in the tube bank and in the delivery duct, and flow visualization was performed to observe the fluid motions in the tube bank. It was found that the enlargement can give rise to appreciable increases in the tube-bank heat transfer coefficients compared with those for the no-enlargement case. The enlargement also causes an additional pressure drop which depends on the magnitude of the enlargement and, to a lesser extent, on the distance between the enlargement and the tube bank.

NOMENCLATURE

A_{\min}	minimum free flow area between tubes
D	tube diameter
\mathcal{D}	diffusion coefficient
f	friction factor
K	per-tube mass transfer coefficient
\dot{m}	rate of mass transfer per unit area
$Nu_{0.7}$	Nusselt number corresponding to $Pr = 0.7$
Pr	Prandtl number

p	pressure
p_{atm}	ambient pressure
Δp_{incr}	enlargement-related incremental pressure drop
Re	Reynolds number $\rho V D / \mu$
S	side of square duct
Sc	Schmidt number
Sh	per-tube Sherwood number, KD/\mathcal{D}
S_L	longitudinal pitch
S_T	transverse pitch
V	maximum velocity, $\dot{w}/\rho A_{min}$
\dot{w}	mass flow rate
X	axial coordinate
μ	viscosity
ν	kinematic viscosity
ρ	air density
ρ_{nw}	naphthalene vapor density at tube surface
ρ_{nb}	naphthalene vapor density in bulk flow

INTRODUCTION

In tube-bank crossflow heat exchangers, the crossflow fluid may be delivered to the bank via a duct whose cross section differs from the inlet-face cross section of the bank. Frequently, the area of the inlet face is substantially larger than the cross-sectional area of the duct, necessitating an enlargement either at or upstream of the inlet. Cross-sectional enlargements generally give rise to separation and accompanying flow disturbances, except for gradually tapered enlargements which are rarely encountered in heat exchanger practice because of space limitations. Most commonly, the enlargement is accomplished either abruptly or by means of a rapid taper. Depending on the distance upstream of the tube bank inlet at which the enlargement occurs, the highly disturbed flow which it spawns may have a significant effect on the heat transfer and pressure drop characteristics of the bank.

The objective of the experiments to be reported here is to determine the heat transfer and pressure drop response of a tube bank to an abrupt enlargement of the flow cross section which occurs either upstream of or at the bank inlet. Measurements were made of the per-tube heat transfer coefficient at each tube in each successive row, starting at the first row and proceeding downstream until fully developed conditions were encountered. Pressure drops were also measured on a row-by-row basis. To supplement the heat transfer and pressure drop data, flow visualizations were performed within the tube bank to observe the paths followed by the disturbances generated by the upstream cross-sectional enlargement.

The experiments encompassed a total of nine different ducting arrangements. These included three lengths of the duct which delivers the flow to the tube bank inlet face and three enlargements of the flow cross section. The enlargement occurs at the upstream end of the delivery duct, so that the chosen ducting arrangements position the enlargement at various distances from the tube bank inlet face. To provide a basis for assessing the effect of the enlargement, the aforementioned experiments included the case of no enlargement. For each of the ducting arrangements,

measurements were made for two Reynolds numbers which spanned an order of magnitude.

The heat transfer results will be presented in a format designed to provide an immediate indication of the effect of the enlargement. At each tube in the bank, the heat transfer coefficient in the presence of enlargement is ratioed with that for the no-enlargement case, with all other geometrical and flow parameters being held fixed. If this ratio exceeds one, then the enlargement is enhancing, while values of the ratio below one indicate degradation. The ratios which pertain to the respective tubes are inscribed on a plan-view layout of the bank, thereby facilitating the identification of which portion of the bank is affected by the enlargement.

The measured pressure distributions yielded fully developed friction factors in the tube bank and incremental pressure losses associated with the presence of the enlargement. The flow visualization work was carried out using the oil-lampblack technique, and representative photographs of the flow traces are included in the paper.

The flow nonuniformity induced by an abrupt enlargement situated either at or upstream of the inlet face of a tube bank can be regarded as a maldistribution. In the heat exchanger literature, there is a keen awareness of the potential importance of maldistributed inlet flows on the performance of the exchanger, as witnessed by several papers in a just-published symposium volume {1}. However, a careful literature search did not reveal any published quantitative information on the effect of upstream cross-sectional enlargement on the heat transfer and pressure drop in a crossflow tube bank.

THE EXPERIMENTS

As noted earlier, the work included three types of experiments--heat transfer, pressure drop, and flow visualization. Both from the standpoint of higher accuracy and of experimental simplicity, mass transfer experiments offer several advantages compared with direct heat transfer experiments. In the present study, the naphthalene sublimation technique was employed to determine mass transfer coefficients which can be transformed to heat transfer coefficients by means of the analogy between the two processes.

The description of the experimental apparatus is facilitated by reference to Fig. 1. The diagram at the upper part of the figure shows the inlet face of the tube bank. As seen there, the cross section of the duct in which the tube bank is housed is a square of side S . The lower part of the figure is a plan view looking downward into the apparatus (as if the upper wall were removed). This diagram shows a portion of the tube bank and the entirety of the delivery duct which conveys fluid to the inlet face of the bank. The delivery duct is, in effect, an upstream extension of the duct which houses the tube bank. It is straight and of square cross section with side S .

The different lengths of the delivery duct employed during the experiments can be identified in Fig. 1. For the longest duct, the length is about $4.5S$, while the length of the intermediate duct is about $2.5S$. The shortest duct is of zero length.

The delivery duct--tube bank system was operated in the suction mode. Air was drawn from the laboratory room into the upstream end of the delivery duct or, for the delivery duct of zero length, directly into the inlet face of the tube bank. The air passed through the delivery duct and the tube bank, through a square-to-circular transition section, and then through an air-handling system consisting of flowmeters (calibrated rotameters), control valves, and blowers. The blowers were situated outside the laboratory so that their discharge, which was heated by compression and also contained naphthalene vapor, would not be recycled through the

experimental apparatus.

The cross-sectional enlargements were obtained by affixing plates with different opening apertures either at the upstream end of the delivery duct or at the inlet face of the tube bank (for the delivery duct of zero length). Figure 2 depicts the flow cross sections of the plates that were employed. At the left of the figure is the no-plate, no-enlargement case which serves as a baseline. The middle diagram shows a plate whose open area is one half that of the duct, resulting in a duct-to-aperture area ratio of two. In the plate in the right-hand diagram, the duct-to-aperture area ratio is four. The plates were of 0.318 cm aluminum and were machined with a downstream-facing bevel to ensure a clean flow separation.

Attention will now be turned to the tube bank. It consisted of fifteen rows of tubes deployed in a staggered, equilateral triangular array with six tubes in each row. Such an array is characterized by $S_L = 0.866S_T$ (S_L = longitudinal pitch, S_T = transverse pitch). The selected tube diameter D and transverse spacing yielded a pitch-to-diameter ratio $S_T/D = 2$. The key dimensions of the tube bank were the tube diameter $D = 0.635$ cm and the side of the square duct which housed the bank, namely, $S = 7.62$ cm.

It may be noted that the length-to-diameter ratio of the tubes is twelve, which is believed sufficiently large to minimize the role of end effects. Another measure to minimize end effects was the use of half tubes adjacent to the side walls in alternate rows as shown in Fig. 1.

In the main, the experiments were performed such that in each data run, only one of the tubes directly participated in the mass transfer process. In the various runs, the mass-transfer-active tube was deployed at different positions throughout the array. The other tubes in the array were made of steel rod stock (actually, drill rod). In a few selected data runs, as many as three rows of the array were entirely populated by mass-transfer active tubes.

For the effective implementation of the naphthalene sublimation technique,

it is necessary that there be rapid access to the test section for the installation or removal of the mass-transfer-active tubes. This is because sublimation, while much diminished, continues to occur even when there is no airflow in the test section. The required access was achieved by making the upper wall of the test section removable, with quick-acting clamps being used to lock the wall in place during the data runs.

The mass-transfer-active tubes consisted of a naphthalene coating over a cylindrical metal substrate. The surface of the substrate had been roughened by a screw-threading operation to provide better adhesion of the naphthalene. With regard to the coating process, it consisted of two distinct stages. In the first stage, the substrate was dipped repeatedly into a pool of molten naphthalene, which produced a somewhat rough, overly thick coating. The desired final dimensions and surface finish were obtained by machining the naphthalene surface on a lathe. The finished dimensions of the naphthalene-coated tubes were identical to those of the steel rods which comprised the other tubes of the array.

Each mass transfer data run consisted of two distinct parts: the equilibration period and the data run proper. During the equilibration period, the mass-transfer-active tube, situated in the test section and suitably covered to prevent sublimation, attained temperature equality with the airflow. The mass of the tube was measured prior to the data run proper. During the run, the tube was exposed to the airflow for a period of time which limited the change of thickness of the naphthalene coating to less than 0.0025 cm. At the termination of the run, the mass was measured again. After this second mass measurement, a mock data run was performed to determine the amount of sublimation that might have occurred during the installation, removal, and handling of the tube--after which the mass was once again measured. All mass measurements were performed with a Sartorius ultra-precision electronic balance capable of discriminating 10^{-5} g. The air temperature was read with an ASTM-certified thermometer with 0.1°F scale divisions.

Pressure drop measurements were made in data runs separate from the mass transfer runs. For this purpose, an axial array of pressure taps had been installed along the upper wall of the delivery duct and the test section, midway between the side walls. In the test section, the first tap was situated midway between the second and third rows, and subsequent taps were separated by twice the longitudinal pitch. Eight taps were installed in the delivery duct at axial stations which will be evident from the pressure drop data to be presented later. The pressure distributions were read with a Baratron capacitance-type pressure meter capable of resolving 10^{-4} mm Hg.

As noted earlier, flow visualization was carried out using the oil-lampblack technique. According to this method, a mixture of oil and lampblack powder of suitable fluidity is applied to the surface which bounds the airflow whose characteristics are to be determined. When the airflow is initiated, the mixture may move along the surface, following the paths of the fluid particles. In regions of low velocity (e.g., stagnation, separation), the mixture does not move, thereby indicating the presence of such regions. The attainment of the proper fluidity to achieve a true rendering of the flow pattern is a trial and error process. The oil-lampblack method is not very effective on vertical, inclined, or downfacing surfaces because the mixture tends to sag.

In the present study, the oil-lampblack mixture was applied to the lower wall of the test section, which had been coated with white contact paper to provide high contrast. The mixture was found to respond to the highest Reynolds numbers in the investigated range (~ 8400), but the forces imposed by low Reynolds number flows did not move the mixture. Because of this, all of the final visualization runs were performed at a Reynolds number of about 8400.

FLOW VISUALIZATION RESULTS

The greatest contrast between the tube bank flow patterns which correspond to different enlargements occurs when the enlargement takes place at the inlet face of the tube bank. The oil-lampblack visualization patterns will, therefore, be presented for that case (i.e., for the delivery duct of zero length). Photographs of the visualization patterns corresponding to no enlargement, two-fold enlargement, and four-fold enlargement are respectively presented in Figs. 3, 4, and 5. In each figure, the inlet of the tube bank corresponds to the lower edge of the photograph, and the mainflow direction is from the lower edge to the upper edge.

An overview of these figures indicates that while the flow in the tube bank is spanwise periodic and without large-scale transverse motions when there is no enlargement (Fig. 3), these features no longer prevail in the presence of enlargement, especially in the forwardmost rows (Figs. 4 and 5). This is to be expected since the blockage caused by the enlargement plate (middle and right-hand diagrams of Fig. 2) causes the flow to be concentrated in the central portion of the inlet cross section and, thereby, to enter the tube bank as a jet. As a consequence, the entering flow does not impinge directly on the sidewall-adjacent tubes of the forwardmost rows. The resulting lower velocities in those regions are unable to move the oil-lampblack mixture so that the initial black coating remains, as seen in the sidewall-adjacent regions in Fig. 5 and to a lesser extent in Fig. 4.

The lateral spreading of the entering jet is clearly in evidence in Fig. 4 and even moreso in Fig. 5, as manifested by the tongue-like streaks which are threaded between the tubes in the first several rows. It appears that for the two-fold enlargement (Fig. 4), the flow pattern beyond the fifth row tends to coincide with that for the no-enlargement case. On the other hand, the effects of the four-fold enlargement continue to be felt farther downstream (Fig. 5). For example, in the eighth row, a tongue of fluid is seen issuing from the side wall toward the center of the array. These lateral flows occur because the overly rapid

transverse spreading of the jet gives rise to an excess of fluid near the side walls, and corrective motions must occur before fully developed conditions can prevail.

From a close inspection of Figs. 4 and 5, it may be conjectured that the highest heat transfer coefficients in the presence of enlargement occur in the middle of the third row. This conjecture is based on what appears to be an intense scrubbing of the duct wall in that neighborhood by the fluid. In Fig. 3 (case of zero enlargement), the flow pattern about the first row is highly distinct from that of the downstream rows, as is to be expected. The second row displays small differences from the others, but for the third row and beyond the flow pattern appears to have a fixed shape.

HEAT (MASS) TRANSFER RESULTS

The data reduction for the mass transfer work will now be briefly described, followed by the presentation and discussion of the results. In view of the analogy between the two processes, the phrases mass transfer and heat transfer will be used interchangeably during the discussion.

Data reduction. The measured per-tube change of mass during a data run, when divided by the duration of the run and the surface area of the tube, yielded the quantity \dot{m} . In turn, when \dot{m} is divided by the concentration difference for mass transfer, $(\rho_{nw} - \rho_{nb})$, the per-tube mass transfer coefficient follows as

$$K = \dot{m} / (\rho_{nw} - \rho_{nb}) \quad (1)$$

In equation (1), ρ_{nw} is the density of the naphthalene vapor at the surface of the tube. It was evaluated from the Sogin vapor pressure--temperature relation {2} in conjunction with the perfect gas law. The quantity ρ_{nb} is the density of the naphthalene vapor in the fluid approaching the particular tube under consideration. As noted earlier, most of the data runs were made with only one mass-transfer active tube in the array, and for that case $\rho_{nb} = 0$. In those cases where mass transfer occurred upstream of the monitored tube, then $\rho_{nb} = \dot{M}/\dot{Q}$, where \dot{M} is the

sum of the mass transfer rates at all the upstream tubes and \dot{Q} is the volume flow rate.

In dimensionless terms, the mass transfer coefficient can be represented by the Sherwood number

$$Sh = KD/\delta = (KD/\nu)Sc \quad (2)$$

where, in the second form, the diffusion coefficient has been replaced by the kinematic viscosity via the Schmidt number. Note that the tube diameter D has been used as the characteristic length.

The Reynolds number will be defined in terms of the maximum velocity V and the tube diameter D , where $\rho V = \dot{w}/A_{\min}$ (\dot{w} is the mass flow and A_{\min} is the minimum free flow area between the tubes). Therefore,

$$Re = \rho V D / \mu \quad (3)$$

The Sherwood number results obtained here correspond to a Schmidt number $Sc = 2.5$, while for heat exchanger applications, the Nusselt number for a Prandtl number $Pr = 0.7$ (airflow) is needed. According to Zukauskas [3], for flow through a tube bank $Nu \sim Pr^{0.36}$, and by analogy $Sh \sim Sc^{0.36}$. Therefore,

$$Nu_{0.7} = 0.632 Sh_{2.5} \quad (4)$$

With the use of equation (4), the present Sherwood number results can be employed for airflow heat transfer in tube banks.

Heat (mass) transfer without enlargement. To provide a basis for evaluating the effect of upstream cross-sectional enlargement, the experimental results for the no-enlargement case will be presented first. These experiments were performed with a delivery duct of zero length as well as for delivery duct lengths equal to 2.5S and 4.5S (see Fig. 1).

The corresponding row-by-row variations of the Sherwood number are plotted in Fig. 6, respectively for $Re = 850$ in the lower part of the figure and for $Re = 8400$ in the upper part of the figure. To obtain the plotted values of the Sherwood number, mass transfer measurements were made at the middle three tubes

in the odd rows and at the middle two tubes in the even rows, and the average was taken to be the representative value for the row. The data are interconnected by lines to provide continuity. Different ordinate scales are used for the upper and lower parts of the figure, and both scales are highly expanded. To emphasize this, vertical distances corresponding to a five percent interval in the Sherwood number are shown in the figure.

The figure shows the expected increase of the Sherwood number in the initial rows, as the turbulence spawned by the tubes enhances the mass transfer. At larger downstream distances, a periodic flow pattern which repeats itself in each successive row is established, so that the Sherwood number becomes a constant.

Whereas the aforementioned behavior is wholly expected, the overshoot which appears in the respective Sherwood number distributions (and which was confirmed by numerous repetitive data runs) is quite unexpected. This overshoot amounts to 2 - 4 percent of the respective fully developed value and is, therefore, not of major practical importance. It appears to be somewhat more strongly manifested when the delivery duct is present.

The presence of the delivery duct and its length have a modest effect (< five percent) on the Sherwood numbers in both the development and fully developed regions. Without a delivery duct, the flow tends to separate at the sharp-edged inlet face of the tube bundle. With the delivery duct in place, the flow presented to the tube bank is either a partially or fully developed channel flow. Figure 6 shows that the Sherwood numbers corresponding to the longest delivery duct are the lowest among the three cases. In the development region, the highest Sherwood numbers correspond to the medium-length delivery duct, while in the fully developed region the highest values are for the no-delivery-duct case.

The trends discussed in the foregoing paragraphs are common to both of the investigated Reynolds numbers. The thermal development of the flow is achieved somewhat more rapidly at the higher Reynolds number than at the lower Reynolds

number, with fully developed conditions being attained after four to five rows.

The fully developed Sherwood numbers will now be compared with the widely quoted tube bank heat transfer correlation of Zukauskas {3}. For this purpose, for each Reynolds number, the fully developed Sherwood numbers for the three delivery-duct configurations were averaged, yielding $Sh = 29.3$ and 117.1 , respectively for $Re = 850$ and 8400 . The corresponding Sherwood numbers from the Zukauskas correlation are 28.7 and 113.3 . The deviations are in the 2 - 3 percent range, which can be regarded as very good agreement.

The results which have been presented in the preceding portion of this section were obtained from experiments in which mass transfer occurred at only one tube in the array. Attention will now be turned to results of experiments in which there were many mass-transfer-active tubes in the array. For these experiments, all of the whole tubes in rows four, five, and six--a total of seventeen tubes--were naphthalene coated. The wall-adjacent half tubes in the fifth row could not be coated, but this limitation did not affect the Sherwood numbers, which were purposefully evaluated at the tubes in the middle of the sixth row. The tubes in the other rows were metallic. Although it would have been desirable to have populated additional rows with mass-transfer-active tubes, it was not possible to execute the experiment with any more than the seventeen active tubes that were employed.

For both $Re = 850$ and 8400 , four data runs were carried out with the multi-active-tube arrangement. The Sherwood numbers for each Reynolds number were averaged and then compared with the corresponding values obtained from the experiments performed with a single mass-transfer-active tube. For $Re = 8400$, the Sherwood numbers for the two cases were virtually identical, while for $Re = 850$, the Sherwood number for the multi-active case was 2.8 percent above that for the single-active case. This finding lends support to the use of results from single-active-tube experiments for predicting the performance of fully active arrays.

Heat (mass) transfer with enlargement. The per-tube heat (mass) transfer

results in the presence of upstream cross-sectional enlargement are presented in Figs. 7 - 10. These figures convey a great deal of information and, before discussing the substance of the results, it is appropriate to describe the format, which is common to all of the figures.

Each figure corresponds to a given enlargement and a given Reynolds number. Figures 7 and 8 are both for a four-fold enlargement and, respectively, for $Re = 850$ and 8400 . Similarly, Figs. 9 and 10 are both for a two-fold enlargement, with $Re = 850$ and 8400 respectively. An indication of the extent of the enlargement is shown by the dashed lines at the bottom of each figure. The direction of the mainflow is from the bottom to the top of the figure. To facilitate the discussion of the format, attention may be focused on any one among Figs. 7 - 10, say, Fig. 7.

Figure 7 is a plan view of the array, and numbers are inscribed adjacent to each tube. There are, in fact, two sets of numerical results that are presented, one set being a Sherwood number ratio and the other set being the Sherwood number itself. The values of the Sherwood number ratio are inscribed in the left-hand half of the array while the Sherwood numbers are inscribed in the right-hand half. The two halves of the array may be thought of as being separated by a symmetry line which runs parallel to the two sidewalls, midway between them. Because the area enlargement plates were centered in the cross section (Fig. 2), symmetry prevailed both with and without enlargement. Any slight data scatter at symmetric tube locations was averaged out, and the thus-obtained average values are reported.

The Sherwood number ratios that appear in the left-hand half of the figure will now be explained. Adjacent to each tube, three numbers are generally inscribed (at downstream rows, only one or two numbers may appear). The uppermost of the three numbers pertains to the case where the enlargement occurs at the inlet face of the tube bundle (i.e., no delivery duct). Similarly, the middle and lowermost numbers correspond, respectively, to the cases where the enlargement

occurs at the upstream end of the intermediate and longest delivery ducts (Fig. 1).

Each number represents the ratio

$$\frac{\text{Sh (with enlargement)}}{\text{Sh (without enlargement)}} \quad (5)$$

where both the numerator and denominator of (5) correspond to the same tube position, the same delivery duct length, and the same Reynolds number. The Sh values for the denominator are those of Fig. 6. Note that for the trio of numbers inscribed adjacent to a particular tube location, the denominators are not quite equal.

The Sherwood number ratios are listed to the left of the tube location to which they pertain. The listing of the ratios is continued in the downstream direction until they are more or less equal to unity and then is terminated. The attainment of this condition is more rapid when the delivery duct is in place, and this explains the early termination of the listings for those cases.

The format of the Sherwood number listing in the right half of the figure will now be illuminated. The numbers that appear to the right of each tube location are the Sherwood numbers for that location. For each set of numbers, the upper, middle, and lower entries correspond respectively to enlargement at the tube bundle inlet face and at the upstream end of the intermediate and longest delivery ducts. The row-by-row listing for each delivery duct is continued downstream until a fully developed value is obtained, at which point the listing is terminated.

The reason for presenting both Sherwood number ratios and Sherwood numbers is that each conveys a different type of information. The Sherwood number ratios provide a direct measure of whether enlargement enhances or degrades the per-tube Sherwood number, with ratios larger than one indicating enhancement and ratios below one indicating degradation. However, the largest ratios do not correspond to the

largest Sherwood numbers nor do the smallest ratios correspond to the smallest Sherwood numbers. It is for this reason that the actual Sherwood numbers are also listed.

The discussion will now be directed to the trends in the Sherwood number ratio. From an overview of Figs. 7 - 10, it is seen that the ratios in excess of one far outweigh the ratios that are less than one. Even among the ratios whose values are less than one, most are only a few percent below, and only two values are less than 0.9 (0.86 and 0.89, respectively). Therefore, the presence of the enlargement enhances the tube bundle heat transfer. Furthermore, the larger the enlargement ratio, the greater is the enhancement, as can be seen by comparing Figs. 7 and 8 with Figs. 9 and 10. The extent of the enhancement is also strongly influenced by the location of the enlargement, with greater enhancements being encountered when the enlargement occurs closer to the bundle inlet.

On the other hand, the closer the enlargement to the bundle inlet and the greater the enlargement ratio, the larger is the overall nonuniformity of the Sherwood number ratio in a given row. These intra-row nonuniformities result because the fluid flow entering the tube bundle is concentrated in the central region of the inlet cross section. Therefore, in the initial rows of the bundle, lower values of the Sherwood number ratio are encountered adjacent to the side walls. These nonuniformities disappear with increasing downstream distance.

However, in the extreme case when the largest enlargement ratio occurs at the bundle inlet face, a secondary intra-row nonuniformity appears downstream, whereby the highest Sherwood number ratio in the row occurs adjacent to the side walls (Figs. 7 and 8). This behavior is consistent with the findings of the flow visualization studies, where it was noted that overly rapid transverse spreading of the flow in the initial rows gives rise to an excess of fluid adjacent to the side walls in the later rows. The secondary intra-row nonuniformity dies away at sufficient downstream distances.

The greatest enhancements occur in the first row of the tube bundle. The extent of the enhancement encountered there increases somewhat with the Reynolds number and markedly with the enlargement ratio and with closer proximity of the enlargement to the bundle inlet. It is also interesting to observe that for the greatest enlargement ratio and closest proximity, concerns about a possible "dead-water," degraded-Sherwood-number zone directly behind the enlargement step did not materialize. In Fig. 8, first-row enhancements that exceed a factor of two are in evidence, and enhancements almost as large occur in the first three rows in both Figs. 7 and 8.

Significant effects of the enlargement (ten percent or greater) persist to the eighth row for the four-fold enlargement positioned at the inlet face of the bundle (Figs. 7 and 8). This deep penetration into the bundle is associated with the just-discussed secondary fluid flow nonuniformity. For the inlet-positioned two-fold enlargement, ten percent effects are felt through the fourth row (Figs. 9 and 10).

When the enlargement occurs at the upstream end of the delivery duct, its effect does not penetrate as far into the bundle as when the enlargement occurs at the bundle inlet. For example, in the case of the longest delivery duct and a four-fold enlargement, the effect persists to the third row for $Re = 850$ (Fig. 7) and only to the second row for $Re = 8400$ (Fig. 8). Even shorter penetrations are in evidence for the two-fold enlargements (Figs. 9 and 10).

The row-by-row progression of the Sherwood number ratios toward a downstream value of unity is not necessarily monotonic. This is because both the numerator and denominator Sherwood numbers which comprise the ratio may vary nonmonotonically from row to row. In particular, in connection with the denominator values, there is an overshoot which was identified in connection with Fig. 6. The non-monotonic behavior of the numerator will be discussed shortly.

Attention will now be turned to the Sherwood number values listed in the right-hand half of Figs. 7 - 10. To identify the main trends, it is useful to

focus on a given enlargement ratio and enlargement positioning and to follow the Sherwood number from row to row. For the four-fold enlargement at the closest position, the Sherwood number increases from the first to the third rows, at which point it attains a maximum and then drops off very sharply, followed by a more gradual decline. Farther downstream, localized increases occur adjacent to the side walls as a result of the previously mentioned secondary fluid flow nonuniformity.

For the same enlargement ratio but with the enlargement at the intermediate position, the maximum is now shared by the second and third rows and is also less lofty. With the enlargement at the position farthest upstream of the bundle inlet, the Sherwood number varies monotonically from row to row for $Re = 850$ but displays a slight maximum for $Re = 8400$. The localized Sherwood number increases in the downstream part of the bundle, which were observed for the close-positioned enlargement, do not occur when the enlargement is positioned upstream of the bundle inlet.

For the two-fold enlargement and $Re = 850$ (Fig. 9), an unambiguous maximum occurs (in the third row) only at the closest positioning of the enlargement. When $Re = 8400$ (Fig. 10), maxima (also in the third row) are in evidence for the first two enlargement positions, but to a lesser extent as the position moves upstream of the inlet.

It is relevant to note that the flow visualization photographs, Figs. 4 and 5, foretold the presence of the third-row maxima.

By examining the trio of Sherwood numbers adjacent to each tube location, the effect of the delivery duct length can be identified. The variations among the numerical values which constitute a given trio are, of course, greatest in the initial rows. These variations are impressively large in the presence of the four-fold enlargement but are more moderate for the two-fold enlargement.

PRESSURE DROP RESULTS

As was noted earlier, taps had been installed along the upper wall of the delivery duct and the test section to enable the measurement of the axial pressure distributions. For each case (i.e., given delivery duct length, enlargement ratio, and Reynolds number), the measurements yielded the distribution of $(p_{\text{atm}} - p)$, where p is the local pressure at any tap location and p_{atm} is the ambient pressure in the laboratory from which the air was drawn. To obtain a dimensionless representation, it is appropriate to normalize the aforementioned pressure difference by a representative velocity head $\frac{1}{2}\rho V^2$ which is a constant for each case. For this purpose, ρV^2 was evaluated as

$$\rho V^2 = \dot{w}^2 / \rho A_{\text{min}}^2 \quad (6)$$

where \dot{w} and A_{min} are defined in the text just prior to equation (3), and ρ is the average density in the test section (evaluated at the seventh row).

Figures showing the axial distributions of $(p_{\text{atm}} - p) / \frac{1}{2}\rho V^2$ are available for each delivery duct length. However, to conserve space, only the figure for the longest delivery duct need be presented here. As will be shown shortly, this figure can be used to describe the characteristics of the pressure distributions for the other delivery ducts.

The pressure distributions are presented in Fig. 11. The data shown there, all for the longest delivery duct, are parameterized by the enlargement ratio (1, 2, 4) and by the Reynolds number (850, 8400). On the abscissa, $X = 0$ corresponds to the inlet face of the tube bundle. Axial stations to the left of $X = 0$ are situated in the delivery duct. For those stations, the abscissa variable is X/S (S = side of square delivery duct). The tube bundle is situated to the right of $X = 0$, and here the row number is used as the abscissa variable (the markers for the row numbers are positioned at the centers of the tubes). Owing to the fact that $(p_{\text{atm}} - p)$ appears on the ordinate, an increasing trend in the data indicates

a dropping pressure, while a decreasing trend in the data indicates a pressure rise.

Attention is first turned to the pressure distributions in the tube bundle. As noted earlier, the first tap is situated midway between the second and third rows, and subsequent taps are spaced two rows apart. It is seen that for each case, the data fall on a straight line, which suggests that fully developed conditions prevail at the third and all subsequent rows. This development is slightly more rapid than that for the development of the tube-bundle Sherwood number distributions in the presence of the longest delivery duct. This finding is consistent with the fact that the pressure distribution develops more rapidly than the velocity field. The slopes of the three lines for $Re = 850$ are nearly the same, and similarly for the three lines for $Re = 8400$. This characteristic will be employed shortly in the determination of quantitative pressure-related parameters.

Next, turning to the delivery duct, it may be noted that the flow separation which takes place at the upstream end of the duct has a marked effect on the pressure distribution, especially at larger enlargement ratios. For the four-fold enlargement, the pressure drop (shown as a rise in the figure) between the first and second stations is due to the acceleration of the fluid as it pinches together downstream of the enlargement plate (i.e., vena contracta effect). Subsequently, there is a pressure rise (a decrease in the figure) associated with the velocity decrease which accompanies the expansion of the fluid into the enlarged cross section. The pressure rise continues to occur up to the last pressure tap in the delivery duct, indicating that the expansion has not been completed at that station.

For the two-fold enlargement, the aforementioned vena contracta effect is no longer in evidence, and the first several taps display a rising pressure. Near the downstream end of the delivery duct, the pressure appears to be independent of X . Since the friction-related pressure drop is too small to be seen in the scale of the figure, the apparent pressure uniformity indicates that the inertia-related effects spawned by the enlargement have died away, although it is improbable

that the flow is fully developed.

Even in the absence of an enlargement plate at the upstream end of the delivery duct, there is a small zone of separation due to the sharp-edged nature of the inlet. The pressure recovery downstream of the separated region is reflected by the first and second data points for the zero-enlargement case. The subsequent data points are essentially at uniform pressure, reflecting the virtually imperceptible friction-induced pressure drop. Although not completely fully developed, the flow arriving at the inlet face of the tube bundle should have experienced substantial development.

In the intermediate-length delivery duct, the measured pressure distribution for each case is essentially identical to the first four data points in the corresponding delivery-duct pressure distribution of Fig. 11. Furthermore, the tube-bundle pressure distributions are very similar to those of Fig. 11. For the case of no delivery duct, the measured tube-bundle pressure distributions are also similar to the distributions of Fig. 11, except that the data from the first tap do not lie on the straight lines which pass through the data from the other taps.

The presence of the enlargement gives rise to an additional pressure drop relative to the no-enlargement case. For the longest delivery duct, the enlargement-induced incremental pressure drops Δp_{incr} can be read from Fig. 11 as the vertical distances between the straight lines appearing in the right-hand portion of the figure. For example, for $Re = 850$ and a four-fold enlargement, $\Delta p_{\text{incr}} / \frac{1}{2} \rho V^2$ is read between the uppermost and lowermost straight lines that pass through the circle data symbols. Values read in this way from Fig. 11 and from similar figures for the intermediate- and no-delivery-duct cases are listed in Table 1.

The table shows that the incremental pressure drop ranges from 7.5 - 12 velocity heads for the four-fold enlargement and from 1.3 - 2.5 heads for the two-fold enlargement. There is no appreciable difference between the results for the longest

and intermediate delivery ducts, but there is a significant increase in the pressure loss when the enlargement occurs at the inlet face of the tube bundle (i.e., no delivery duct). The table also shows that the smaller the Reynolds number, the larger is the value of $\Delta p_{\text{incr}} / \frac{1}{2} \rho V^2$.

Fully developed friction factors in the tube bundle can be determined from least-squares straight lines fitted through the pressure distributions. If $(-dp/dN)$ represents the pressure drop per row, then the friction factor was evaluated from

$$f = (-dp/dN) / \frac{1}{2} \rho V^2 \quad (7)$$

For a given Reynolds number, the fully developed friction factor was found to be only slightly affected by the delivery duct or by the enlargement. These variations were averaged out, yielding $f = 0.56$ and 0.36 , respectively for $Re = 850$ and 8400 .

CONCLUDING REMARKS

The results presented here have shown that the presence of an abrupt cross-sectional enlargement upstream of a tube bank can give rise to appreciable increases in the heat transfer coefficient compared with the no-enlargement case. Thus, the use of heat transfer information from the literature (presumably for no enlargement) to design a tube bank with upstream enlargement is conservative. On the other hand, the enlargement causes an additional pressure loss as listed in Table 1, and these losses should be included in the fluid flow design calculations.

ACKNOWLEDGMENT

The research reported here was performed under the auspices of the Office of Naval Research.

REFERENCES

1. S. Kakac, R. K. Shah, and A. E. Bergles, Low Reynolds Number Flow Heat Exchangers, Hemisphere, Washington, D.C. (1982).
2. H. H. Sogin, Sublimation from discs to air streams flowing normal to their surfaces, Trans. ASME 80, 61-71 (1958).
3. A. A. Zukauskas, Heat transfer from tubes in crossflow. In Advances in Heat Transfer, Vol. 8, Academic Press, New York (1972).

Table 1

Incremental Pressure Drop $\Delta p_{\text{incr}} / \frac{1}{2} \rho V^2$ Due to Enlargement

Re	Area Ratio	Delivery Duct		
		Longest	Middle	None
850	2	1.4	1.5	2.5
850	4	8.4	8.9	11.9
8400	2	1.3	1.3	1.8
8400	4	7.6	7.5	9.2

FIGURE CAPTIONS

- Fig. 1 Diagrams of the experimental apparatus
- Fig. 2 Enlargement configurations
- Fig. 3 Flow visualization pattern when there is no enlargement and no
 delivery duct
- Fig. 4 Flow visualization pattern in the presence of two-fold enlargement
 at the tube-bank inlet
- Fig. 5 Flow visualization pattern in the presence of four-fold enlargement
 at the tube-bank inlet
- Fig. 6 Sherwood number distributions for the no-enlargement case
- Fig. 7 Sherwood numbers and Sherwood number ratios for a four-fold
 enlargement and $Re = 850$
- Fig. 8 Sherwood numbers and Sherwood number ratios for a four-fold
 enlargement and $Re = 8400$
- Fig. 9 Sherwood numbers and Sherwood number ratios for a two-fold
 enlargement and $Re = 850$
- Fig. 10 Sherwood numbers and Sherwood number ratios for a two-fold
 enlargement and $Re = 8400$
- Fig. 11 Pressure distributions in the longest delivery duct and in the
 tube bank

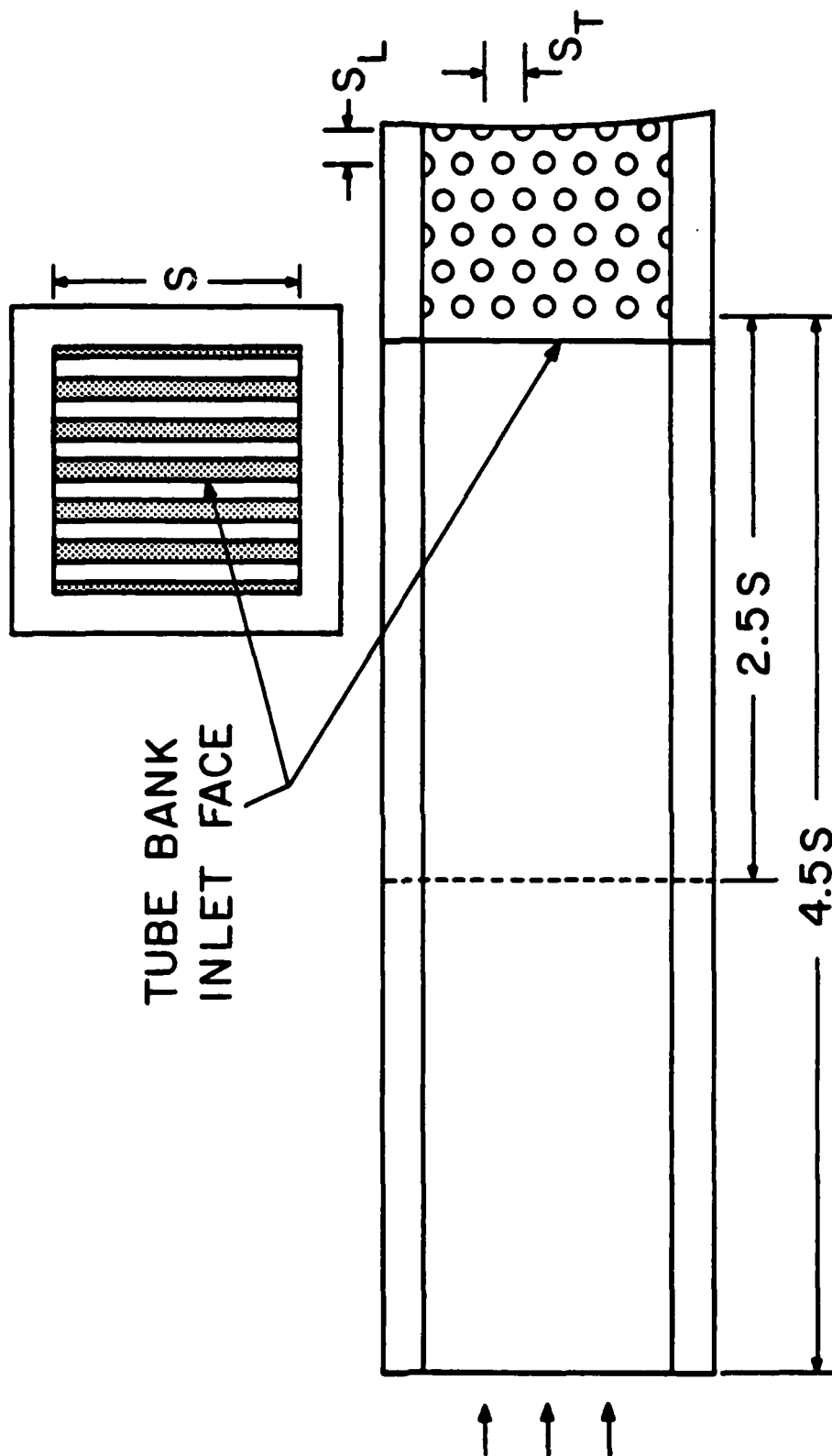


Fig. 1

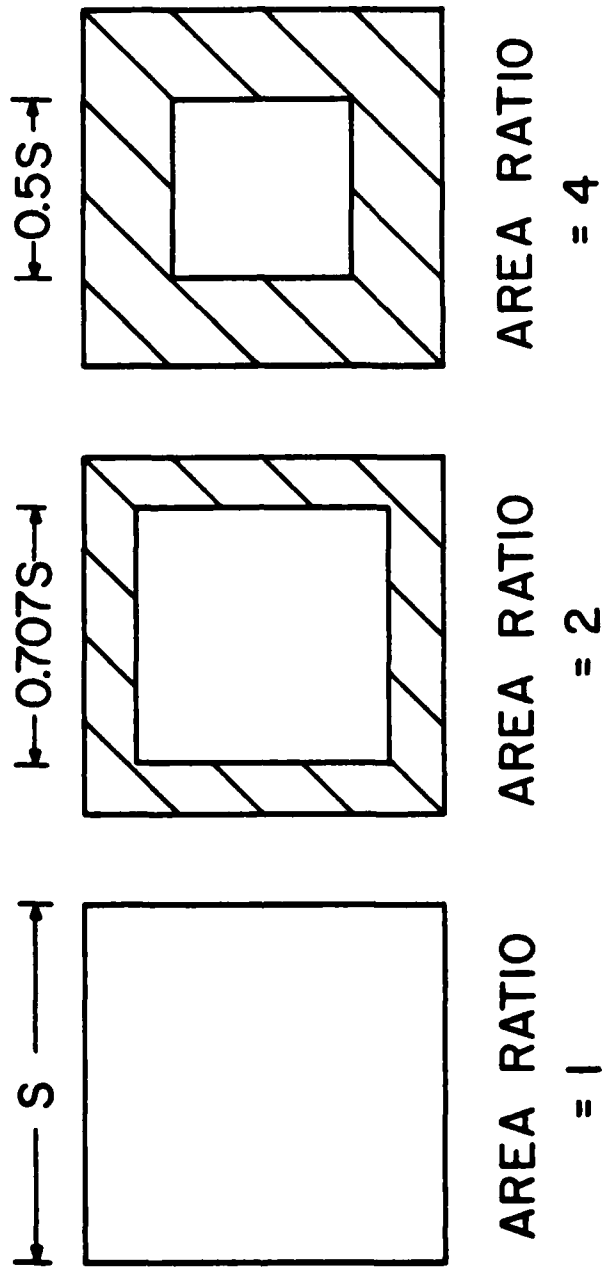


Fig. 2

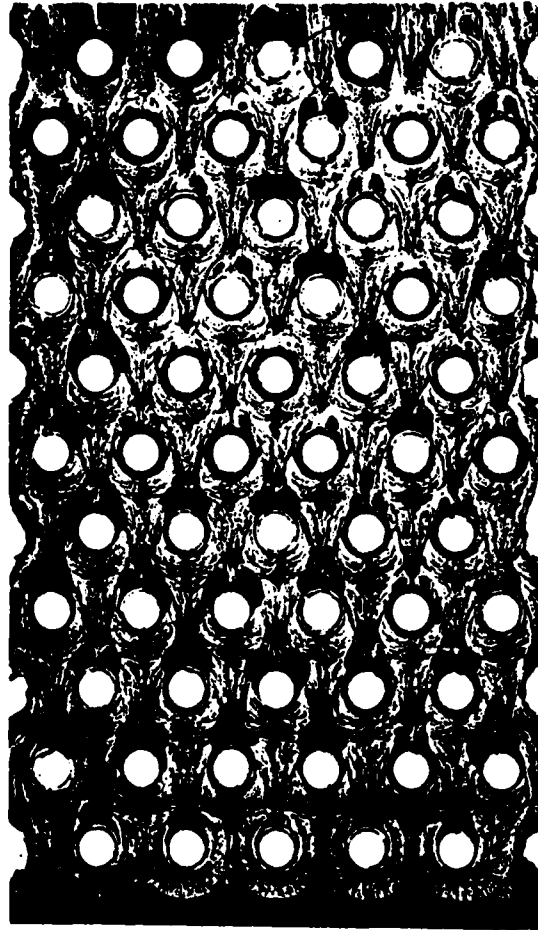


Fig. 3

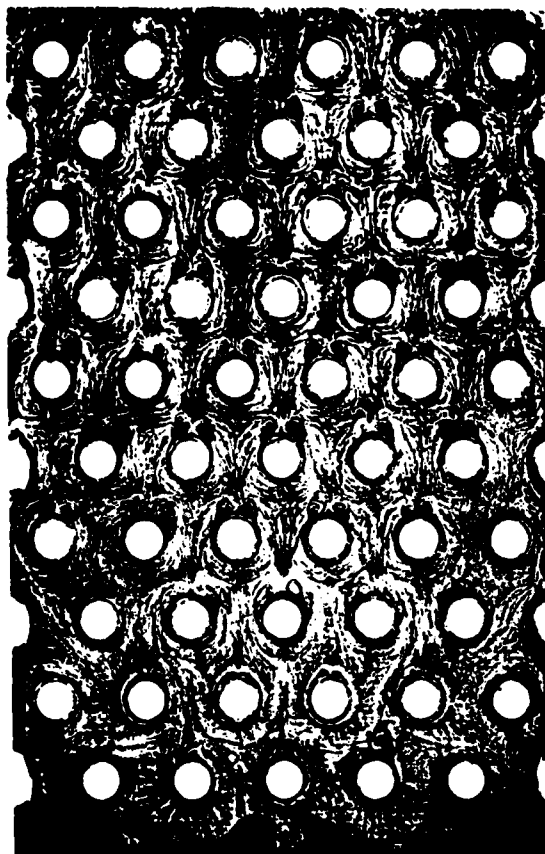


Fig. 4

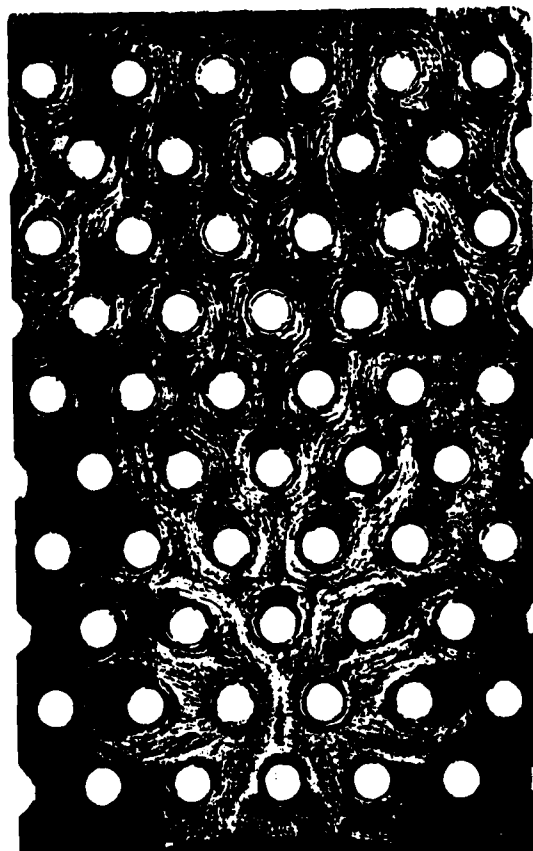


Fig. 5

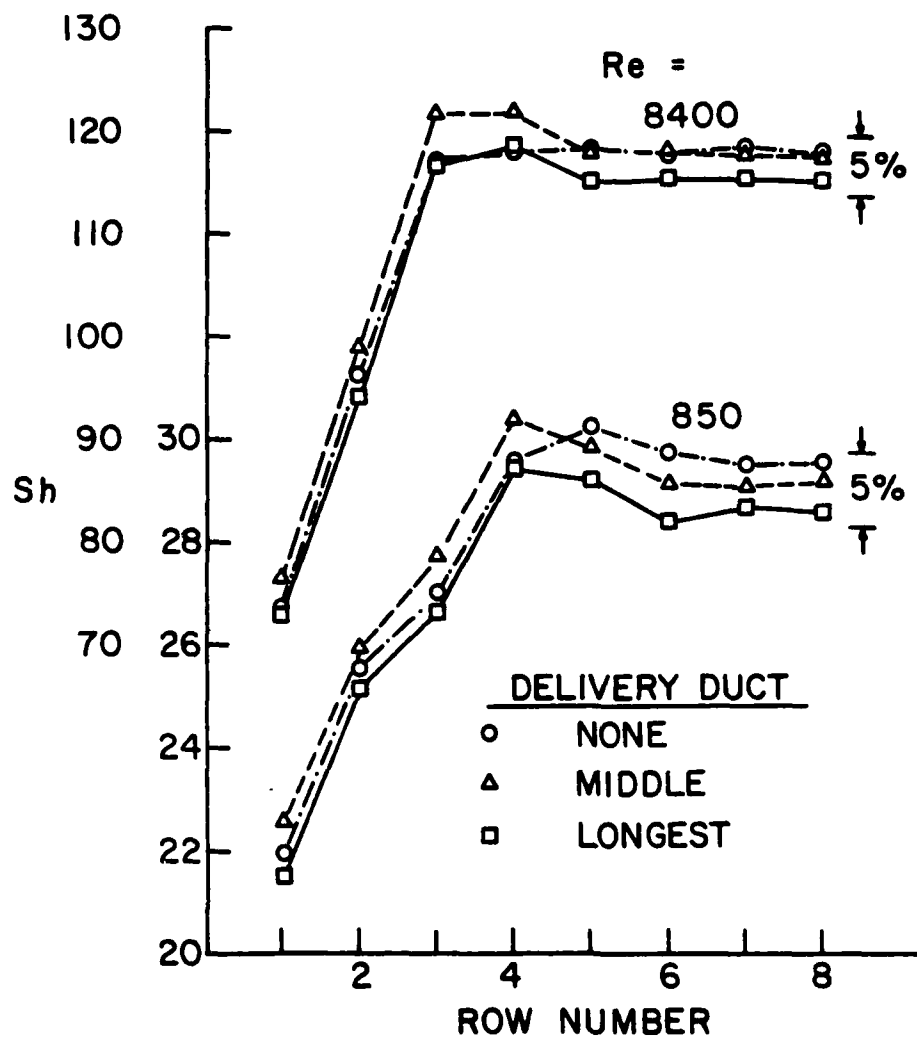


Fig. 6

12

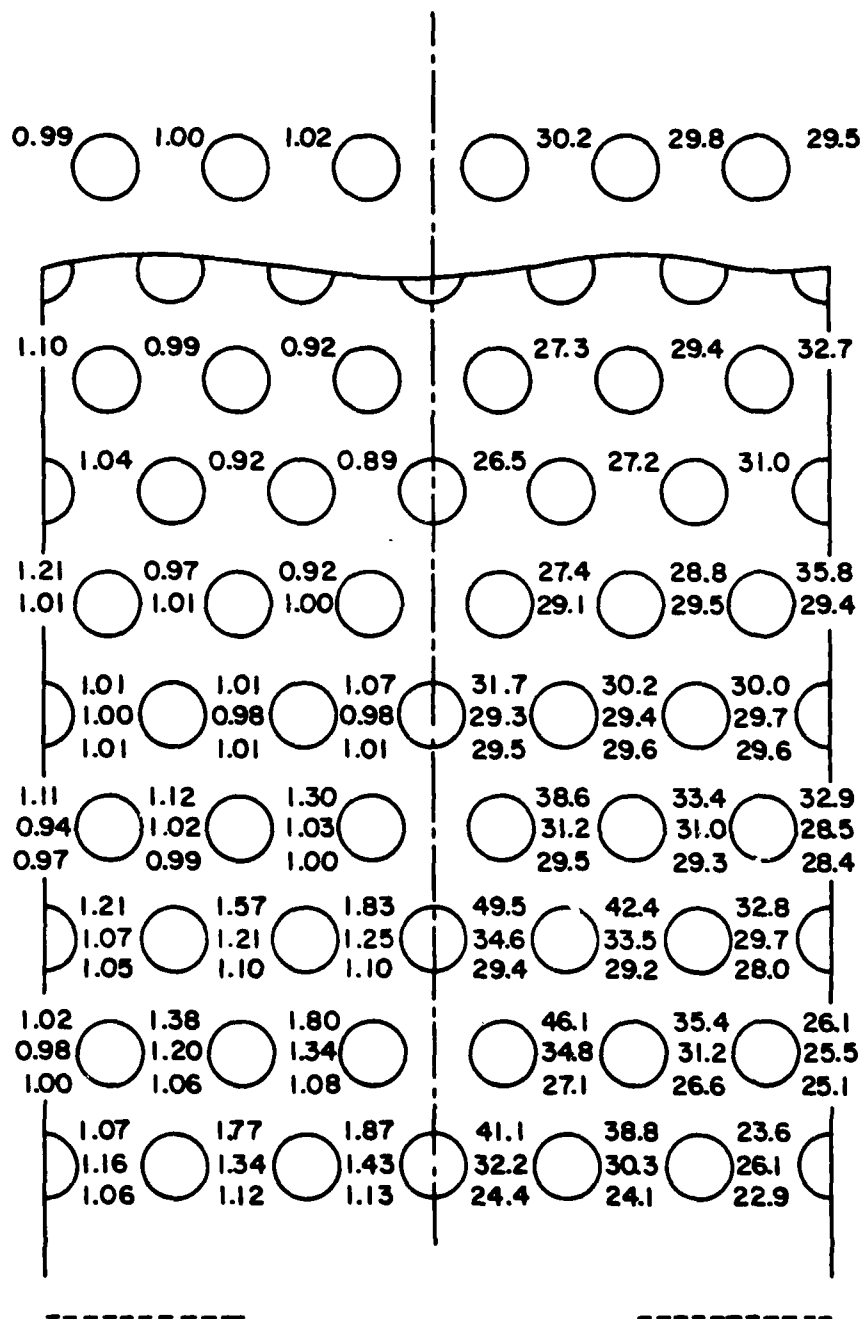


Fig. 7

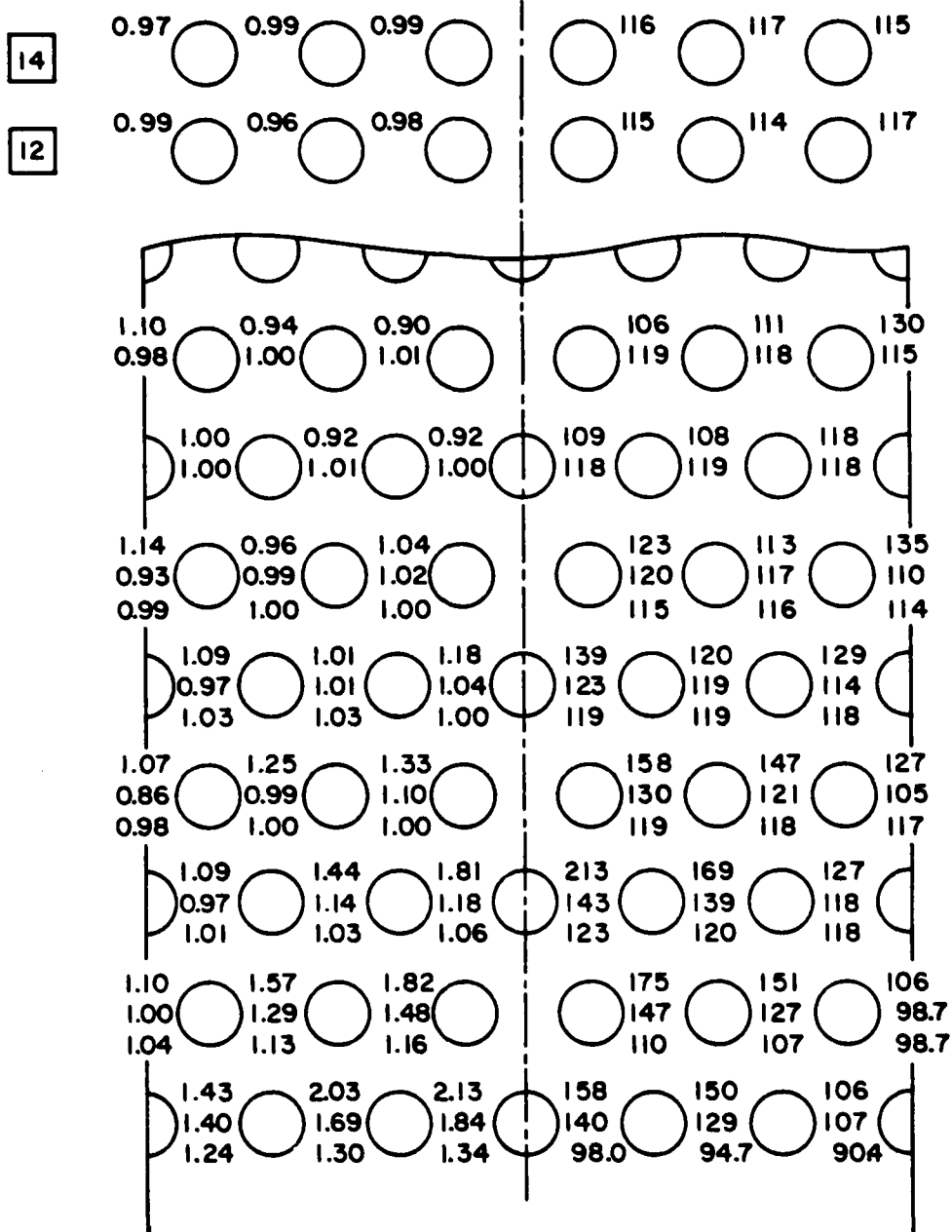


Fig. 8

12

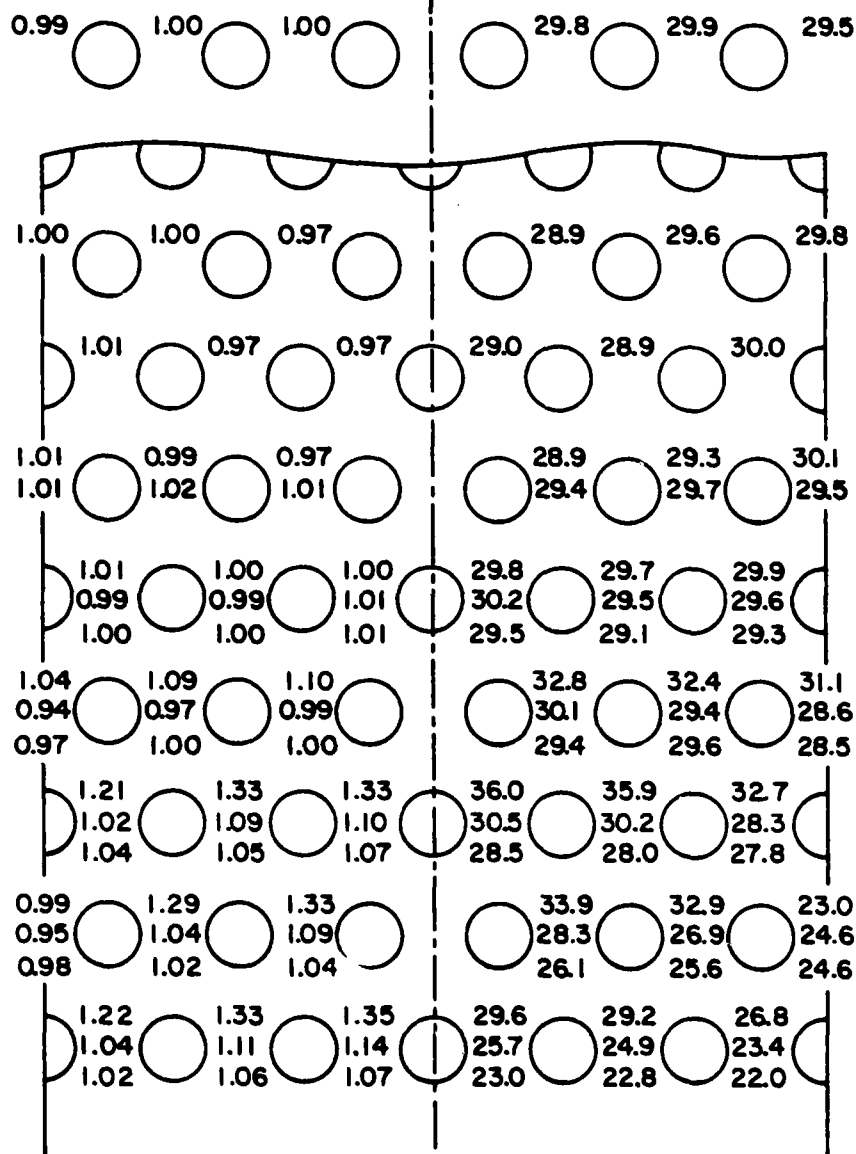


Fig. 9

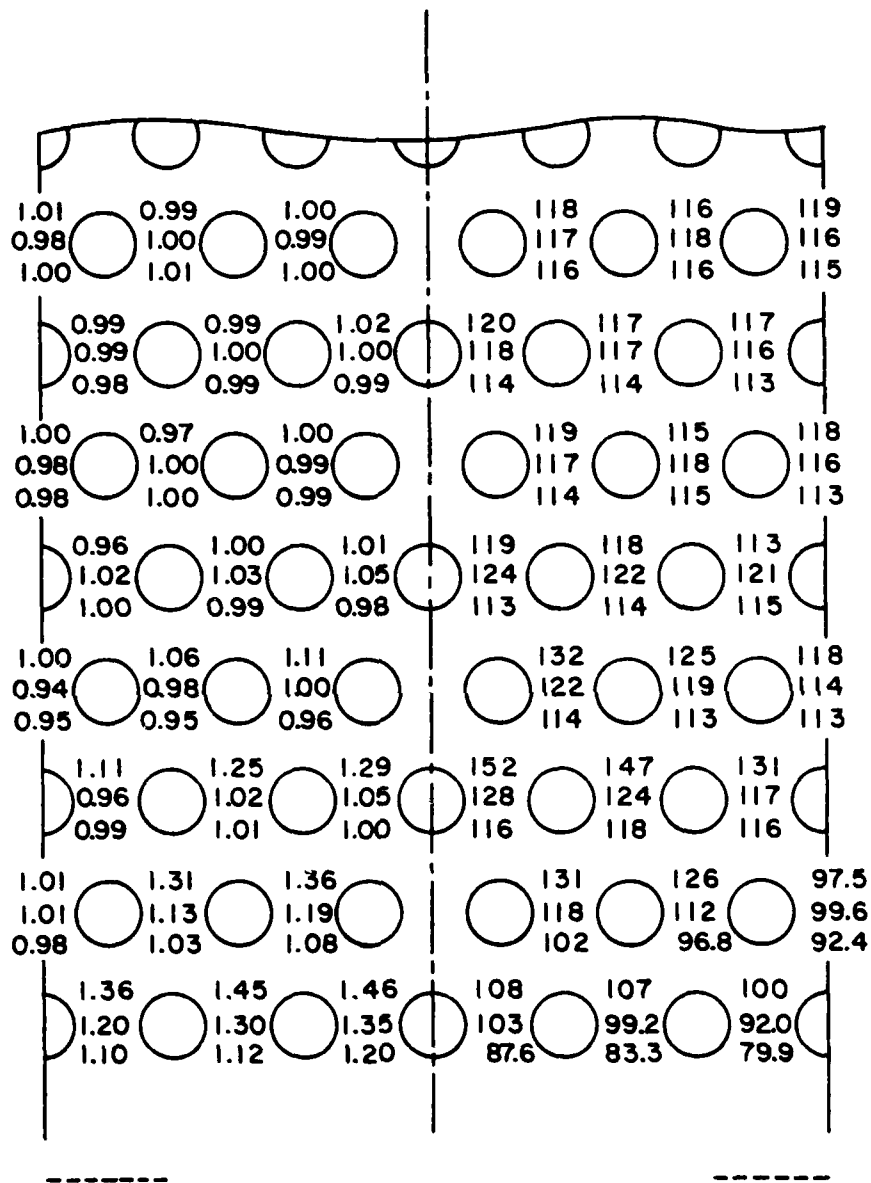


Fig. 10

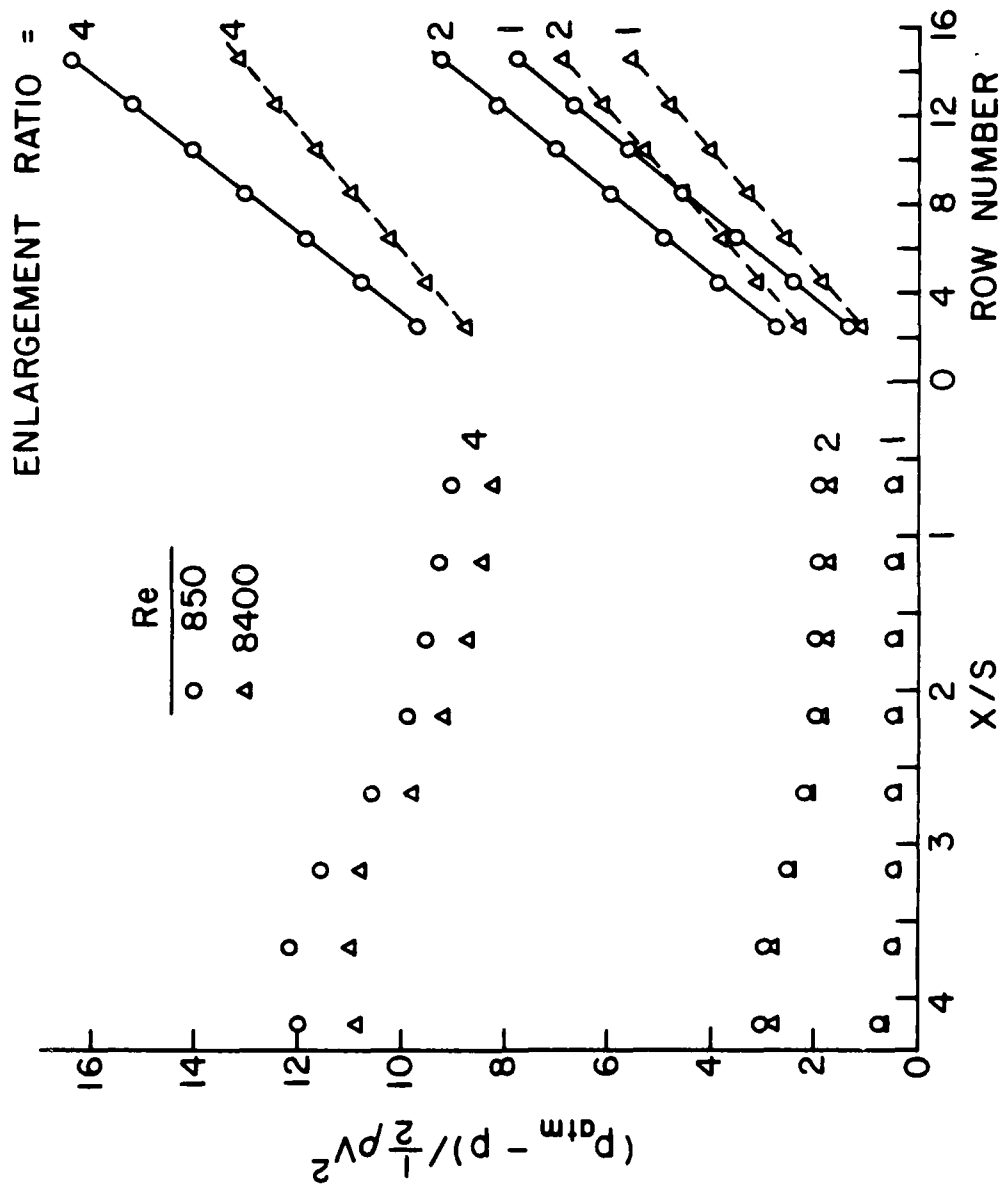


Fig. 11

IN-TUBE HEAT TRANSFER FOR SKEWED INLET FLOW CAUSED BY
COMPETITION AMONG TUBES FED BY THE SAME PLENUM

ABSTRACT

Measurements were made of the axial and circumferential distributions of the heat transfer coefficient in a tube in which the entering airflow is highly skewed. The skewness was caused by competition between the test section tube and a parallel tube which draws air from the same plenum chamber. For each of several fixed Reynolds numbers in the test section tube, the flow imbalance between the competing tubes was varied parametrically (up to a factor of eighteen), as was the center-to-center separation distance between the tubes (separation = 1.5, 3, and 4.5 times the tube diameter). Measurements were also made of the pressure drop, and a visualization technique was employed to examine the pattern of fluid flow. Practically significant effects of the flow imbalance on the axial distribution of the heat transfer coefficient were encountered only at the smallest of the investigated inter-tube spacings. Even for that case, the effects were moderate; for example, the imbalance-related changes for an imbalance ratio of two did not exceed seven percent. The experiments involved naphthalene sublimation, and a new technique was developed for coating the inside surface of a tube with naphthalene.

NOMENCLATURE

A	mass transfer surface area
D	tube inner diameter
D	diffusion coefficient
f	friction factor

K	mass transfer coefficient, equation (1)
K_p	incremental pressure loss coefficient
L_{mod}	axial length of naphthalene surface per module
ΔM	mass sublimed during data run
\dot{Q}	volumetric flow rate
p	pressure at X
p_∞	pressure in plenum
Re	Reynolds number, $4\dot{w}/\mu\pi D$
Re_1	Reynolds number of test section tube
Re_2	Reynolds number of competing tube
S	center-to-center separation
Sc	Schmidt number
Sh	Sherwood number, KD/\mathcal{D}
$Sh_{fd,0}$	fully developed Sherwood number for single tube
V	mean velocity
\dot{w}	airflow rate
X	axial coordinate
θ	angular coordinate
μ	viscosity
ν	kinematic viscosity
ρ	density
ρ_{nb}	naphthalene vapor density in bulk
ρ_{nw}	naphthalene vapor density at wall
τ	duration of run

Subscripts

1	test section tube
2	competing tube

INTRODUCTION

It is a common occurrence in heat exchange devices that a number of tubes draw fluid from the same header or plenum so that, in effect, the tubes are competing among themselves for the available fluid. This occurs, for example, in a shell and tube heat exchanger where the tube inlets, built into a tube sheet, face upstream into a plenum chamber from which all tubes draw their fluid. The presence of the assemblage of tubes and the inherent competition among them plays a decisive role in shaping the velocity distribution in the fluid entering any given tube. Indeed, even in the simplest configurations, the tube inlet velocity will differ significantly from the classical cases (e.g., either uniform or fully developed profiles) which are used in both experimental and analytical studies of in-tube heat transfer.

As a case in point, consider a very large plenum supplied with fluid at its upstream end and bounded at its downstream end by a tube sheet in which the tubes are arranged on equilateral triangular centers. If the rate of fluid flow drawn into each tube is the same, then, owing to symmetry, each inlet is fed by a stream tube of hexagonal cross section which extends from the face of the tube sheet back into the plenum. Thus, the velocity profile at inlet corresponds to that for an abrupt contraction from the hexagonal stream tube to the circular inlet aperture in the tube sheet and is, clearly, more complex than those of the standard pipe-flow literature.

The next stage of inlet profile complexity--that which is the focus of the present investigation--is the presence of a high degree of skewness in the profile. The skewness may result from a number of factors. One of these factors, the one involved in the present experiments, is differences in the rate of fluid flow passing through the various tubes of the assemblage which draw from the plenum. Thus, for example, a tube inlet situated next to one which draws a relatively high rate of flow from the plenum will experience an entering velocity distribution that is skewed in the direction of the high-inflow tube. Furthermore, the extent of the skewness of the inlet velocity distribution will be accentuated as the degree of the

tube-to-tube flow imbalance increases.

Skewed inlet profiles may also result from the geometry of the plenum or from the manner in which fluid is supplied to the plenum. In a narrow plenum, the fluid particles must move on highly curved trajectories in order to reach the various inlet apertures in the tube sheet. Similarly, fluid supplied to the plenum via a port in the side of the plenum will also move along trajectories that are highly curved.

In the presence of a skewed inlet velocity distribution, the separation of the flow (which occurs at any sharp-edged inlet) will also be skewed, as will the subsequent reattachment. Moreover, the non-axisymmetric turning of the flow as it enters the tube should also give rise to a secondary (i.e., circumferential) flow superposed on the mainflow. These features are not encountered in conventional, axisymmetric, single-tube flows from which heat transfer results are customarily obtained for subsequent use in heat exchanger design.

The focus of this investigation is the determination of turbulent pipe-flow heat transfer coefficients in the presence of skewed inlet velocity distributions. The approach taken here is to look at the generic problem rather than to be concerned with the large number of specific physical situations where skewness occurs. To this end, an experimental setup was employed which enabled the skewness to be varied in a systematic manner and which was capable of yielding skewnesses even more exaggerated than those encountered in normal practice. As indicated earlier, the inlet-profile skewness studied here is associated with tube-to-tube flow imbalance, but the results should have qualitative significance for skewness in general.

A schematic view of the experimental arrangement is shown in the upper diagram of Fig. 1. As seen there, two parallel tubes are set into a large circular plate (hereafter called the baffle plate) and draw from the open space upstream of the plate. Each tube was equipped with a downstream-positioned blower, control valve, and flowmeter (not shown), so that the rate of airflow passing through each could

be controlled independently.

The experiments were conducted at several fixed Reynolds numbers (i.e., flow rates) in the test section tube 1 covering the range from 5000 to 44,000. At each fixed Re_1 , the Reynolds number Re_2 of the second tube was varied from zero to as large a value of Re_2/Re_1 as was permitted by the capabilities of the apparatus (up to $Re_2/Re_1 = 18$). The variation of Re_2/Re_1 at a fixed value of Re_1 served to vary the degree of skewness of the velocity distribution at the inlet of tube 1. Correspondingly, the measured Nusselt numbers for tube 1 revealed the response of a fixed-Reynolds-number pipe flow to the degree of flow imbalance and inlet-profile skewness.

Another parameter varied during the course of the investigation was the proximity of the tubes. If S denotes the center-to-center separation distance and D is the internal diameter of the tubes, then the proximity may be defined by the S/D ratio. The investigated values of S/D included 1.5, 3, and 4.5.

Two types of heat transfer coefficients were measured. For each data run, circumferential-average coefficients were obtained at 21 to 24 axial stations along the length of the test section tube. For selected runs and at a specific axial station, circumferential variations of the coefficient were also measured.

In actuality, the heat transfer coefficients were determined indirectly via the analogy between heat and mass transfer, with the experiments themselves being performed with the naphthalene sublimation technique. In this regard, a new procedure was developed for applying on the inside of a tube a naphthalene coating of precise dimensions and having a hydrodynamically smooth surface finish.

Two types of fluid flow measurements were made to supplement the heat transfer experiments. The oil-lampblack flow visualization method was employed to examine the pattern of fluid flow adjacent to the tube wall, especially in the region where the separated flow reattaches to the wall. Axial pressure distributions were also measured to identify the effect of the skewed inlet velocity on the pressure drop.

To the knowledge of the authors, the work described here is the first research

involving multiple-tube competing flows. A variety of inlet conditions for single tubes has been investigated, as reported in {1 - 3}.

EXPERIMENTAL APPARATUS

As noted earlier, the experiments were conducted utilizing a pair of parallel tubes whose upstream ends mated with a large baffle plate and which drew air competitively from the space upstream of the baffle. Whereas the two tubes experienced strong hydrodynamic interactions, no mass transfer interactions can occur (note that extraneous, difficult-to-control, thermal interactions would have occurred had heat transfer experiments been performed). Therefore, only one of the two tubes (i.e., tube 1) need participate in the mass transfer process, while the other tube (tube 2) functions only as a fluid flow device. Correspondingly, tube 1 was internally coated with naphthalene and tube 2 was metallic (aluminum), without naphthalene. Both tubes had approximately the same internal diameter.

Each of the tubes was part of an independent flow circuit which, along the path of the airflow, included the tube itself, a flowmeter (one of three calibrated rotameters), a control valve, and a blower. The blowers were situated in a service corridor outside the laboratory room, which enabled their discharge, heated by blower compression and laden with naphthalene vapor, to be vented away from the laboratory. As a result of this arrangement, the air in the laboratory was free of naphthalene vapor and at a nearly uniform temperature (about 20°C), maintained by a control system.

In what follows, the mass transfer test sections will be described first, followed by the other apparatus components and the instrumentation.

Mass transfer test sections. Two distinct mass transfer test sections were employed during the experiments--one to determine the axial distribution of the mass transfer coefficient and the other for the circumferential distribution. The axial distribution was, by far, the major focus of the work, and the test section used in its determination will be described first and in greater detail, with that

for the circumferential distribution to follow.

The test section used for the axial distribution was of modular design, and a typical module, flanked by portions of the adjacent upstream and downstream modules, is pictured schematically in the lower diagram of Fig. 1. As seen there, the module consists of an outer metallic shell and an inner annular layer of solid naphthalene that was implanted by a casting process to be described shortly. The metallic shell is a segment of aluminum tube (i.d. = 4.064 cm, o.d. = 4.826 cm). At one end of the segment, an internal recess, 0.508 cm long, was formed by cutting away half the wall thickness. A similar recess was cut into the external surface at the other end of the module. As can be seen in the diagram, the test section was assembled by mating the internal recess of one module with the external recess of the adjacent module, with pressure-sensitive tape used to seal the joint against leaks.

The internal diameter D of the cast naphthalene layer was 3.272 cm, while the axial length L_{mod} of the naphthalene that was exposed to the airflow varied with the selected module. For the modules of the type pictured in Fig. 1, three different lengths L_{mod} were employed, respectively, $L_{\text{mod}}/D = 0.388$, 0.766, and 1.553. In the assembly of the test section, the shortest modules were positioned nearest the inlet, followed by the intermediate modules and then the longest modules. The specific positions of the respective modules will be apparent from the forthcoming presentation of results.

The most-upstream module was, necessarily, somewhat different from the others. The external surface of the metallic wall of the module was machined so that it fit snugly in an aperture in the baffle plate, and the upstream faces of the module and the baffle plate were aligned flush. Moreover, the module design was such that its upstream face was metallic, so that naphthalene sublimation occurred only along the bore of the module. The L_{mod}/D ratio for this module was 0.466.

All told, as many as twenty-four modules were assembled to form the test section. Fixtures and supports were provided to ensure the straightness of the

assembled test section tube.

The technique which was developed for forming a naphthalene coating on the inside surface of a circular tube will now be described. As a first step, the naphthalene coating from the preceding data run was removed from each module by melting and evaporation. Then, a mold was assembled as shown in Fig. 2. The components of the mold included the metallic wall of the module, end caps which mated with the recesses at the respective ends of the metallic wall, and a shaft (diameter = 3.272 cm) which passed through apertures in the end caps and served as the centerbody of the mold. The surface of the shaft had been polished to a mirror-like finish with a succession of lapping compounds.

Molten naphthalene was poured into the annular cavity between the metallic wall and the centerbody through an aperture in the wall. Once the naphthalene had solidified, the shaft and end caps were removed. The resulting surface quality of the cast naphthalene was comparable to that of the polished shaft. As a final step, the pouring aperture was sealed with tape to prevent extraneous sublimation. In certain modules (a total of four), thermocouples were cast into the naphthalene layer, flush with its interior surface.

Attention is now turned to the test section used for the measurement of the circumferential distribution of the heat transfer coefficient. In this regard, it may be noted that the scope of this phase of the investigation was more limited than that aimed at determining the axial distribution. In particular, the circumferential measurements were confined to the axial zone $0.472 \leq X/D \leq 0.848$, which corresponds to the axial range of the second module of the primary test section that was described earlier. This is the range in which the maximum heat transfer coefficients were encountered, and it was for this reason that it was chosen as the site for the circumferential studies.

In essence, the test section was an aluminum tube with a circular patch of naphthalene built into its wall. The tube was fabricated from solid aluminum rod

stock whose external surface was first turned down to the desired outside diameter (to fit snugly into the aperture in the baffle plate). Then, a hole, 1.232 cm in diameter, was drilled radially into the rod at a distance of 2.159 cm from one end. Finally, the rod was bored axially, resulting in a circular tube with an inner diameter of 3.272 cm (exactly equal to the i.d. of the test section described earlier).

The naphthalene patch was cast in place by employing the polished shaft that was used in the casting process for the modules. The shaft was inserted into the bore of the just-described fabricated tube, thereby blocking off the base of the radial hole. Molten naphthalene was poured into the open end of the radial hole, into which a thermocouple was also implanted. After solidification was completed, the polished shaft was removed, leaving a patch of naphthalene which now formed part of the surface which bounded the bore of the tube.

The circumferential position of the patch was varied by rotation of the tube, thereby enabling the detection of the circumferential variation of the transfer coefficient.

The patch was the only naphthalene surface in its test section that was exposed to the airflow. Therefore, the measured circumferential variations of the transfer coefficient reflect circumferential nonuniformities of the velocity field but are not influenced by upstream mass transfer events. Since the role of the velocity is expected to be dominant, the measured coefficients should give a true accounting of the circumferential variations.

Other apparatus components and instrumentation. As already noted, the second of the two parallel tubes served a hydrodynamic function in that it controlled the skewness of the velocity distribution at the inlet of the test section tube. The second tube was of seamless aluminum, with internal and external diameters of 3.239 cm and 4.227 cm, respectively, and a length of 88.9 cm. The tube fit snugly into an aperture in the baffle plate, and the upstream face of the tube wall was flush with the upstream face of the baffle. Fourteen taps deployed along the length

of the tube were used to make the pressure drop measurements to be described later.

The baffle was also of aluminum, 91.44 cm in diameter and 1.23 cm thick. An aperture was bored through the plate at its center to accommodate the test section tube. In addition, four other apertures were machined into the baffle, to be used one at a time to accommodate the second tube. The three apertures not in use were closed by aluminum disks, with the joints filled with body putty. The entire upstream face of the plate was sanded with 600-grit wet or dry paper, with special attention given to ensure a hydrodynamically smooth surface adjacent to the sealed apertures. The apertures were deployed along a radial line, with the respective centers at 1.5D, 3D, 4.5D, and 6D from the center of the test section tube (D = internal diameter of test section tube).

With regard to instrumentation, the four thermocouples implanted in the test section have already been mentioned. A fifth thermocouple measured the inlet air temperature. All thermocouples were precalibrated and were read with a programmable, 1 μ V datalogger. Airflow rates were measured with calibrated rotameters.

Perhaps the most critical measurement was the determination of the masses of the individual modules. The amount of naphthalene sublimed during a data run was determined by differencing the masses of the respective modules measured before and after the run. For this purpose, a Sartorius ultra-precision, electronic analytical balance was employed. This balance has a resolving power of 10^{-5} g and a capacity of 166 g. Typical changes of mass during a run were in the 0.05 g range.

Pressure measurements were made with a Baratron capacitance-type, solid-state pressure meter able to detect 10^{-3} mm Hg.

FLOW VISUALIZATION

Flow visualization studies were undertaken to gain insights into the effects of the skewed inlet velocity on the pattern of fluid flow in the initial portion of the test section tube. These studies were performed utilizing the oil-lampblack technique. With this technique, a mixture of oil and lampblack powder is brushed on the surface which bounds the airflow. Ideally, under the action of the forces exerted by the flow, the mixture will move along the surface, following the paths of the fluid particles which pass adjacent to the surface. In regions of low velocity (e.g., stagnation zones, reattachment zones), the mixture will remain stationary, so that such regions show themselves as black, streak-free zones on the surface.

The technique works best at high Reynolds numbers owing to the relatively high stresses that exist. At low Reynolds numbers, experience with a variety of flows has demonstrated that very little can be seen, even if a mixture of high fluidity is used (low viscosity oil and low particle loading). Furthermore, for vertical or downfacing surfaces, relatively stiff mixtures have to be utilized to prevent sagging and runoff, and such stiff mixtures preclude successful visualizations at low Reynolds numbers. Since the test section tube was horizontal in the present experiments, the employed mixture had to be stiff enough to avoid sagging along a considerable portion of the tube circumference. These realities restricted the visualization work to the high Reynolds number range ($> 35,000$).

To obtain a record of the visualized flow pattern, the inside surface of the test section tube was covered at its upstream end with white, plasticized contact paper. Once the oil-lampblack visualization pattern had been formed, the contact paper was carefully separated from the tube wall and laid flat on a sheet of cardboard for photography.

A photograph of a typical visualization pattern, shown in the aforementioned laid-out format, is presented in the upper portion of Fig. 3. This photograph corresponds to a test-section Reynolds number $Re_1 = 70,000$, to the modest flow

imbalance $Re_2/Re_1 = 1.26$, and to the dimensionless center-to-center separation distance $S/D = 1.5$. The right- and left-hand edges of the photo are parallel to the tube axis, and these edges are in contact with each other during the visualization experiment. The lower edge corresponds to the inlet edge of the test section, while the upper edge corresponds to an axial station that is about $2\frac{1}{2}D$ from the inlet.

To aid in the interpretation of the pattern, a diagram has been included in the lower part of Fig. 3 to define angular positions in the test section tube. The diagram shows the inlets of the test section tube and the competing tube. The origin of the angle θ is at the point of closest proximity of the two tubes. In terms of θ , the right- and left-hand edges of the photograph correspond to $\theta = 180^\circ$.

Prior to the start of the visualization experiment, the entire surface of the contact paper was covered by a uniformly black film of the oil-lampblack mixture, so what is seen in the photograph represents a substantial rearrangement. Four distinct zones are in evidence. There is a relatively straight black band adjacent to the lower edge (i.e., the tube inlet) and a curved black band somewhat downstream. Zones containing streak lines are situated between the two bands and downstream of the second band.

The visualization pattern indicates that the flow separates at the sharp-edged inlet of the tube and reattaches to the tube wall along the wavy black band. The angular variation of the reattachment is a direct consequence of the skewed inlet velocity resulting from the flow imbalance. In view of the modest imbalance ($Re_2/Re_1 = 1.26$), the extent of the circumferential variation is remarkable. The most forward point of the reattachment is at $\theta = 0^\circ$, i.e., at the position of nearest proximity of the tubes, while the most downstream reattachment occurs at $\theta = 180^\circ$, (i.e., on the side of the test section away from the competing tube). These results are consistent with the skewing of the test-section inlet flow in the direction of the competing tube.

The streak lines upstream of reattachment indicate a wall-adjacent backflow--a

flow directed upstream. This backflow is one leg of the recirculating flow which occupies the separation bubble. The backflow carries the oil-lampblack mixture toward the tube inlet and deposits it there, giving rise to the inlet-adjacent black band. It is noteworthy that the backflow streaks are not parallel to the tube axis. Their curvature is indicative of the presence of a circumferential velocity, probably a secondary flow caused by the non-axisymmetric turning of the fluid as it enters the tube.

The streak lines downstream of reattachment suggest the absence of circumferential (secondary) flow except, perhaps, in the neighborhood of $\theta = 180^\circ$. However, at greater flow imbalances, it is quite likely that secondary motions would persist to greater downstream distances.

With regard to the forthcoming mass transfer results, perhaps the most significant finding of the flow visualization is that the flow imbalance (i.e., the initial skewing) shifts the reattachment upstream at $\theta = 0^\circ$ and downstream at $\theta = 180^\circ$. Observations of numerous visualization patterns indicate that this behavior is accentuated with increasing imbalance.

MASS (HEAT) TRANSFER RESULTS

The experiments performed here provide mass transfer coefficients and Sherwood numbers, and these can be converted to heat transfer coefficients and Nusselt numbers by employing the analogy between the two processes. Because of this, the phrases heat transfer and mass transfer will be used interchangeably in the forthcoming presentation. The thermal boundary condition for the heat transfer problem which is analogous to the present mass transfer problem is uniform wall temperature.

Data reduction. The per-module mass transfer coefficient and Sherwood number were evaluated at each module of the primary test section. These coefficients may be regarded as quasi-local. In the forthcoming presentation, they are plotted at the axial mid-points of the respective modules.

At a typical module j , let ΔM_j denote the amount of mass sublimed during the

run time τ and A_j denote the mass transfer surface area. Also, $\rho_{nw,j}$ and $\rho_{nb,j}$ respectively represent the naphthalene vapor densities at the wall and in the bulk. With these, the per-module mass transfer coefficient and Sherwood number are

$$K_j = (\Delta M_j / \tau A_j) / (\rho_{nw,j} - \rho_{nb,j}) \quad (1)$$

$$Sh_j = K_j D / \mathcal{D} \quad (2)$$

where \mathcal{D} is the diffusion coefficient.

Turning to the specifics of the evaluation of K , it may be noted that both ΔM_j and τ are measured quantities and A is known from the geometry of the system. The vapor density ρ_{nw} at the wall was found from successive application of the Sogin vapor pressure--temperature relation {4} and the perfect gas law. The measured wall temperatures were uniform along the test section, so that ρ_{nw} was the same at all modules for a given data run.

To find the bulk vapor density ρ_{nb} at module j , it may first be noted that the increase in ρ_{nb} between the inlet and outlet sections of any module m is

$$(\Delta \rho_{nb})_m = (\Delta M_m / \tau) / \dot{Q} \quad (3)$$

where \dot{Q} is the volumetric flow rate passing through the module. Then, it follows that

$$\rho_{nb,j} = \rho_{nb,o} + \sum_{m=1}^{j-1} (\Delta \rho_{nb})_m + \frac{1}{2} (\Delta \rho_{nb})_j \quad (4)$$

The quantity $\rho_{nb,o}$ is the naphthalene bulk density at the inlet of the test section tube, which is zero for the present experiments. Also, \dot{Q} is virtually constant along the test section (typical variation ~ 0.04 percent).

For the Sherwood number evaluation, it is convenient to eliminate the diffusion coefficient by using the definition of the Schmidt number Sc , which gives

$$Sh_j = (K_j D / \nu) Sc \quad (5)$$

For naphthalene diffusion in air, $Sc = 2.5$ {4}. The kinematic viscosity ν was evaluated as that for pure air--consistent with the minute concentrations of the naphthalene vapor.

The evaluation of K and Sh for the circumferentially orientable test section follows the same pattern as that for each module. The area A that appears in equation (1) now represents the surface area of the naphthalene patch, while $\rho_{nb} = 0$ since no mass transfer occurs upstream of the patch.

The Sherwood number results will be parameterized by the Reynolds numbers Re defined in the conventional manner as

$$Re = 4\dot{w}/\mu\pi D \quad (6)$$

in which \dot{w} is the mass flow rate of the air.

Axial distributions of the transfer coefficient. As a prelude to the presentation of the axial distributions, the measured fully developed Sherwood numbers for single-tube operation will be compared with the literature. For these experiments, the second-tube's aperture in the baffle plate was sealed. Comparisons were made over the range from $Re = 5000$ to $88,000$ with the Petukhov-Popov equation (equations (8 - 23) and (8 - 24) of {5}) and its low Reynolds number extension due to Gnielinski {6}. Agreement to five percent or better was encountered over the entire range, lending strong support to the present experimental technique.

Axial distributions of the Sherwood number along the test section tube are presented in Figs. 4 and 5. These results correspond to two-tube operation (with the single tube as a special case) and to the smallest of the investigated center-to-center separation distances, $S/D = 1.5$. Figure 4 conveys results for two fixed values of the test section Reynolds number, $Re_1 = 5000$ and 9000 , while Fig. 5 presents the corresponding information for $Re_1 = 22,000$ and $44,000$.

At each fixed value of Re_1 , data are plotted for various flow imbalance ratios $Re_2/Re_1 = 0$ (single-tube operation), $2, 4, \dots$. Since the maximum attainable value of Re_2 was approximately $88,000$, the largest imbalance ratio, ~ 18 , was achieved at the smallest $Re_1 (= 5000)$. As Re_1 increased, the range of the imbalance ratio decreased, so that at $Re_1 = 44,000$, the largest imbalance ratio was about two. Correspondingly, the successive graphs, starting with $Re_1 = 5000$ and proceeding toward

larger Re_1 , include fewer data points.

The local Sherwood numbers for all operating conditions at a fixed value of Re_1 have been normalized by the measured fully developed Sherwood number corresponding to single tube operation at that Re_1 . This quantity is designated as $Sh_{fd,0}$, and the ordinates of the graphs are $Sh/Sh_{fd,0}$.

An overall view of Figs. 4 and 5 indicates a common pattern for all the Sherwood number distributions. Starting with a moderate value adjacent to the tube inlet, the Sherwood number increases sharply to a maximum, whereupon it decreases, rapidly at first, and more gradually thereafter, finally approaching the fully developed value. For all cases, the maximum occurs at the second module, which is centered at $X/D = 0.660$.

The aforementioned distribution is characteristic of tube flow with a sharp-edged inlet, which gives rise to inlet-adjacent separation. The reattachment of the flow at the tube wall is responsible for the sharp peak in the transfer coefficient, and the subsequent dropoff of the coefficient is a consequence of the post-reattachment redevelopment of the flow. It is interesting to note that despite the common occurrence of the sharp-edged inlet, analytical predictions for this configuration have not appeared in the literature.

In assessing the effects of flow imbalance (i.e., the skewing of the inlet flow), it is useful to regard the single-tube data (i.e., $Re_2/Re_1 = 0$, open circles) as a reference. Relative to that reference, an overview of Figs. 4 and 5 shows that the imbalance can cause substantial changes in the Sherwood number. However, a closer inspection reveals that if very large imbalances such as $Re_2/Re_1 = 10$ and 18 are excluded, then the effects of the imbalance are moderate. For instance, for $Re_2/Re_1 = 2$ and $Re_1 = 9000$, there is no axial station at which the imbalance-related change in Sh exceeds five percent, while for $Re_1 = 22,000$ and 44,000, five percent (or slightly greater) changes occur at only a few discrete points. Even for $Re_1 = 5000$ and $Re_2/Re_1 = 2$, the largest imbalance-related change is seven percent.

In this regard, it may be noted that a factor-of-two flow imbalance is by no means small when viewed from the standpoint of practice.

Large flow imbalances ($Re_2/Re_1 = 10$ and 18) significantly affect the Sherwood number distribution, both in the immediate neighborhood of the inlet and downstream of the sharp dropoff which follows reattachment. For example, at $Re_1 = 5000$, deviations of ten percent between the large-imbalance distributions and that for the single tube persist to $X/D = 12$. However, with increasing Re_1 , the effect of the imbalance appears to lessen, as suggested by a comparison of the $Re_2/Re_1 = 10$ distributions for $Re_1 = 5000$ and 9000 .

Another interesting characteristic of the results is that the presence of the imbalance does not have a universally enhancing or degrading effect on the Sherwood number. At the first measurement station, the imbalanced flows yield larger Sherwood numbers than that for the single tube, while the opposite relationship is in evidence at the second and third stations. Thereafter, there is even less regularity in that the existence of enhancement or degradation at a specific X/D depends on the magnitude of Re_2/Re_1 . For the larger Re_2/Re_1 (10 and 18), enhancement occurs with regularity in the region downstream of the rapid decrease of the Sherwood number that follows reattachment.

Certain of the trends noted in the preceding paragraph can be rationalized by taking cognizance of the shifting of the reattachment line which accompanies an increase in the flow imbalance ratio, as indicated by the visualization study. Another factor which may explain the downstream enhancement in evidence at large values of the ratio is the presence of a secondary flow (i.e., a swirl) induced when the fluid turns to enter the tube (in a manner similar to a pipe bend).

The data of Figs. 4 and 5 have been brought together in an alternate presentation in Fig. 6 in order to address the question of whether the imbalance-related effects can be correlated solely as a function of the imbalance ratio Re_2/Re_1 . The figure contains three graphs, respectively for $Re_2/Re_1 = 2, 4, \text{ and } 10$ (lower to

upper), and in each graph $Sh/Sh_{fd,0}$ data are plotted for various Reynolds numbers. It is evident from the figure that $Sh/Sh_{fd,0}$ depends on Re_1 as well as on Re_2/Re_1 . Overall, at a fixed Re_2/Re_1 , there is a tendency for $Sh/Sh_{fd,0}$ to increase with Re_1 , which is consistent with the expectation that lower Reynolds number flows are more sensitive to disturbing influences.

Thus far, the presentation of results has been focused on the closest of the investigated center-to-center distances, i.e., $S/D = 1.5$. Attention is now turned to the effect of increases in S/D . Since the lowest Reynolds number case, $Re_1 = 5000$, is the most sensitive to the flow imbalance, it will be considered first.

In Fig. 7, $Sh/Sh_{fd,0}$ distributions for $Re_1 = 5000$ are plotted for $S/D = 3$ and 4.5, respectively in the lower and upper graphs. If Fig. 4 is kept in mind, then Fig. 7 indicates a great decrease in the effects of the flow imbalance with increasing S/D . At $S/D = 3$, there is no detectable effect of the $Re_2/Re_1 = 10$ flow imbalance, and even for $Re_2/Re_1 = 18$ the deviations of the Sherwood numbers from the single-tube values are, for the most part, negligible. If the spacing is increased to $S/D = 4.5$, then the results for $Re_2/Re_1 = 18$ are coincident with those for $Re_2/Re_1 = 0$.

The S/D effect is addressed for larger values of Re_1 in Fig. 8, where results for $Re_1 = 9000$ and 22,000 are plotted for $S/D = 3$. Here again, the data for the $Re_2/Re_1 > 0$ cases are indistinguishable from those for $Re_2/Re_1 = 0$.

Figures 7 and 8 indicate that even enormous flow imbalances are not felt when the tubes are moderately far apart. By the same token, if the tubes were to be positioned much closer together than the $S/D = 1.5$ separation investigated here, there could well be a large magnification of the effects of the flow imbalance.

Circumferential distributions of the transfer coefficient. The circumferential distributions of the Sherwood number, measured by a naphthalene surface patch centered at $X/D = 0.660$, are plotted in Fig. 9. The figure consists of four graphs, respectively for $Re_1 = 5000, 9000, 22,000$, and 44,000. In each graph, data for

$Sh/Sh_{fd,0}$ are plotted as a function of the circumferential position θ , where θ is defined in the diagram below the photograph of Fig. 3. The data are parameterized by the flow imbalance ratio Re_2/Re_1 , with the single tube ($Re_2/Re_1 = 0$) included for reference purposes. All the data are for $S/D = 1.5$.

In appraising the results, it is helpful to recall that $\theta = 0^\circ$ corresponds to the position of closest proximity of the two tubes, while $\theta = 180^\circ$ is the position farthest from the competing tube. It may be noted that uncertainty bars have been affixed to various of the data points. These bars reflect the range of the data from multiple repeated runs; in those cases where there are no bars, the repeated runs gave virtually identical results.

As seen in the figure, the Sherwood number, starting from its value at $\theta = 0^\circ$, increases to a maximum, whereafter it declines and attains a minimum at $\theta = 180^\circ$. Owing to symmetry, the pattern repeats for $180^\circ \leq \theta \leq 360^\circ$. Since the number of circumferential measurement sites was limited, the actual maxima of the respective distributions may not be quite coincident with the plotted maxima. It is believed, however, that the true minimum occurs at $\theta = 180^\circ$.

At high values of the flow imbalance ratio Re_2/Re_1 , the maximum and minimum of the circumferential distribution are widely separated. As Re_2/Re_1 decreases, the extrema tend to come together, and when $Re_2/Re_1 = 0$, the distribution is circumferentially uniform (within the scatter of the data).

The development of the circumferential variation with increasing Re_2/Re_1 can be traced to the related shifting of the flow reattachment--in the upstream direction at $\theta = 0^\circ$ and in the downstream direction at $\theta = 180^\circ$. Thus, for sufficiently large Re_2/Re_1 , the reattachment at $\theta = 0^\circ$ lies upstream of the patch location, while for $\theta = 180^\circ$ the reattachment occurs downstream of the patch. At these angles, the patch is respectively situated in the (post-reattachment) redevelopment region and in the (pre-reattachment) separated region. The curved reattachment line (Fig. 3) passes through the patch site at angular position somewhere between $\theta = 0^\circ$ and 180° ,

causing the maximum in the distribution curve.

PRESSURE DROP RESULTS

For the pressure drop measurements, the tap-equipped metallic tube was positioned in the baffle aperture otherwise occupied by the mass transfer test section. Another metallic tube was employed to establish the flow imbalance.

In all cases, the linearity of the pressure distribution was established for $X/D \geq 10$. In the linear region, the local pressure $p(X)$ can be related to the pressure p_∞ in the upstream plenum via the expression

$$(p_\infty - p(X)) / \frac{1}{2} \rho V^2 = (X/D) f + K_p \quad (7)$$

where f is the friction factor. The quantity K_p is the incremental pressure loss coefficient. It takes account of the losses associated both with the entry of the flow into the tube and with the hydrodynamic development which occurs within the tube.

Values of K_p were determined for both single-tube and imbalanced two-tube operation. For the single tube, the measured K_p values were 1.66, 1.58, 1.53, 1.52, and 1.52, respectively for $Re = 5, 9, 22, 44$, and 88 thousand. Flow imbalance was found to increase K_p but to a remarkably small extent. For example, for $Re_2/Re_1 = 4$, $Re_1 = 22,000$, and $S/D = 1.5$; the K_p value was only 3.7 percent larger than that for the single tube. The maximum imbalance effect on K_p among all of the investigated cases was about ten percent.

CONCLUDING REMARKS

The present work appears to be the first investigation of turbulent tube-flow heat transfer and pressure drop in the presence of inlet flow skewness caused by competition between tubes for fluid drawn from a common plenum. In the execution of the experiments, the test section Reynolds number was fixed at one of several preassigned values, while the flow imbalance was varied parametrically. The effect of the center-to-center distance S between the two competing tubes was also

investigated, with S/D being varied from 1.5 to 3 to 4.5.

The heat transfer results were determined indirectly by mass transfer measurements utilizing the naphthalene sublimation technique. In this regard, a new coating procedure was developed which enabled naphthalene to be cast on the inside of a circular tube. The pattern of fluid flow in the test section tube, just downstream of the inlet, was visualized with the oil-lampblack technique. Axial pressure distributions were measured to determine the additional losses due to the flow imbalance.

Practically significant effects of the flow imbalance on the axial distribution of the Sherwood number were encountered only at the smallest of the investigated intertube spacings, i.e., $S/D = 1.5$. Even for that case, the effects were moderate except at very large imbalances. For example, for a flow imbalance ratio of two, which is by no means small from the standpoint of practice, the largest imbalance-related changes did not exceed seven percent.

The pressure drop information was presented in terms of a coefficient which reflects the losses associated with the entry of the flow into the tube and with its hydrodynamic development. For all the investigated cases, the imbalance-related changes in the loss coefficient were less than ten percent.

ACKNOWLEDGMENT

The research reported here was performed under the auspices of the Office of Naval Research.

REFERENCES

1. Boelter, L.M.K., Young, G., and Iversen, H.W., "An Investigation of Aircraft Heaters, XXVII--Distribution of Heat Transfer Rate in the Entrance Section of a Circular Tube," NACA Technical Note, No. 1451, 1948.
2. Mills, A. F., "Experimental Investigation of Turbulent Heat Transfer in the Entrance Region of a Circular Conduit," Journal of Mechanical Engineering Science, Vol. 4, 1962, pp. 63-77.

3. Lau, S. C., Sparrow, E. M., and Ramsey, J. W., "Effect of Plenum Length and Diameter on Turbulent Heat Transfer in a Downstream Tube and on Plenum-Related Pressure Losses," ASME Journal of Heat Transfer, Vol. 103, 1981, pp. 415-422.
4. Sogin, H. H., "Sublimation from Disks to Air Streams Flowing Normal to Their Surfaces," Trans. ASME, Vol. 80, 1958, pp. 61-71.
5. Karlekar, B. V. and Desmond, R. M., Heat Transfer, second edition, West Publishing, St. Paul, Minnesota, 1982.
6. Gnielinski, V., "New Equations for Heat and Mass Transfer in Turbulent Pipe and Channel Flow," International Chemical Engineering, Vol. 16, 1976, pp. 359-368.

I

FIGURE CAPTIONS

- Fig. 1 Upper diagram: two tube and baffle plate arrangement; lower diagram: typical module
- Fig. 2 Setup for forming a naphthalene coating on the inside of a circular tube
- Fig. 3 Upper part: typical flow visualization pattern ($Re_1 = 70,000$, $Re_2/Re_1 = 1.26$, $S/D = 1.5$); lower part: diagram showing definition of angular positions in the test section tube
- Fig. 4 Axial distributions of the Sherwood number in the presence of various flow imbalances for $Re_1 = 5000$ and 9000 and for $S/D = 1.5$
- Fig. 5 Axial distributions of the Sherwood number in the presence of various flow imbalances for $Re_1 = 22,000$ and $44,000$ and for $S/D = 1.5$
- Fig. 6 Axial distributions of the Sherwood number for flow imbalances $Re_2/Re_1 = 2, 4$, and 10 for various test section Reynolds numbers Re_1 and for $S/D = 1.5$
- Fig. 7 Axial distributions of the Sherwood number in the presence of various flow imbalances for $Re_1 = 5000$ and for $S/D = 3$ and 4.5
- Fig. 8 Axial distributions of the Sherwood number in the presence of various flow imbalances for $Re_1 = 9000$ and $22,000$ and for $S/D = 3$
- Fig. 9 Circumferential distributions of the Sherwood number at $X/D = 0.660$ for various flow imbalances and test section Reynolds numbers and for $S/D = 1.5$

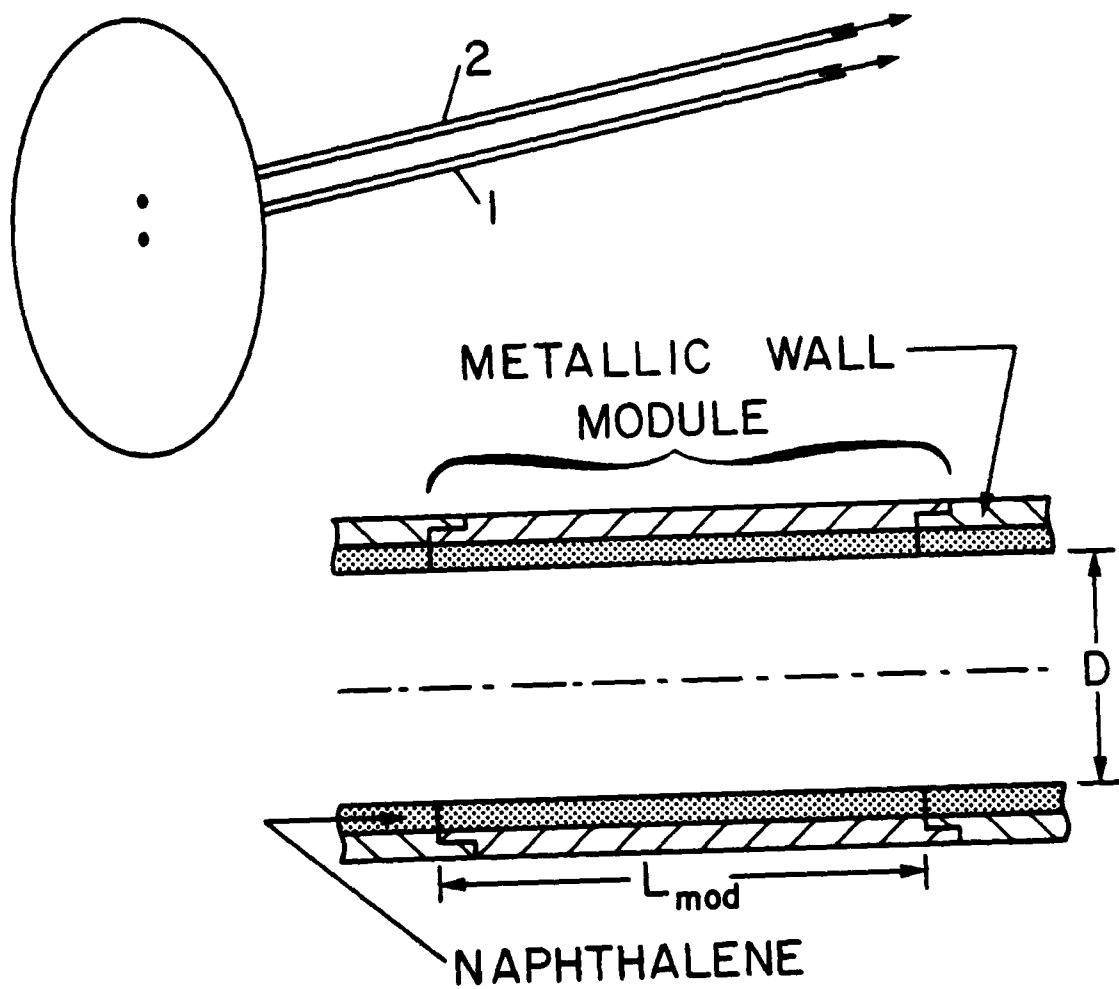


Fig. 1

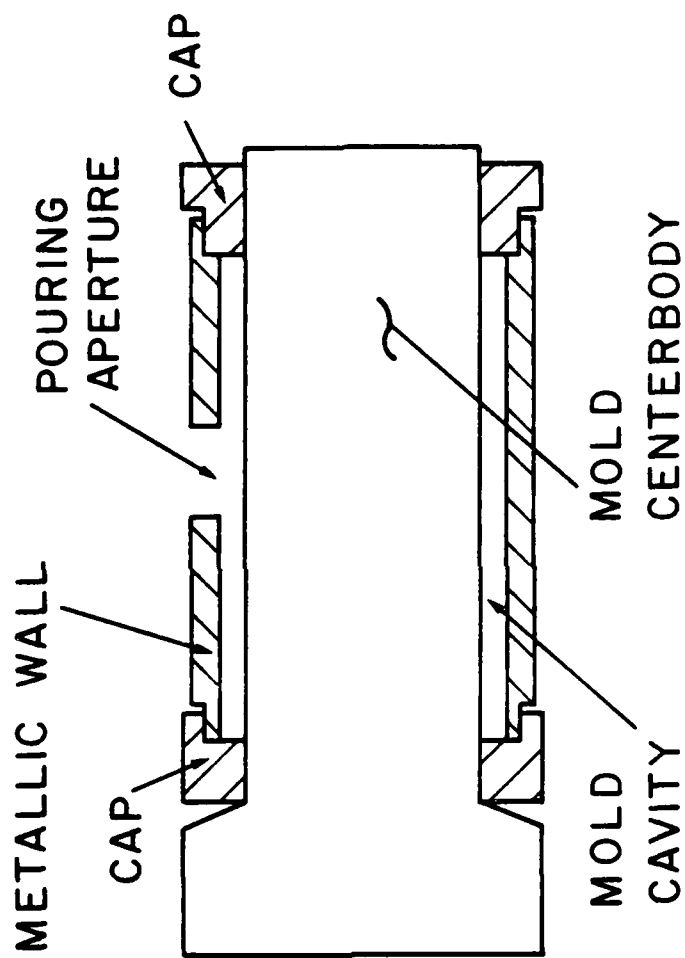


Fig. 2

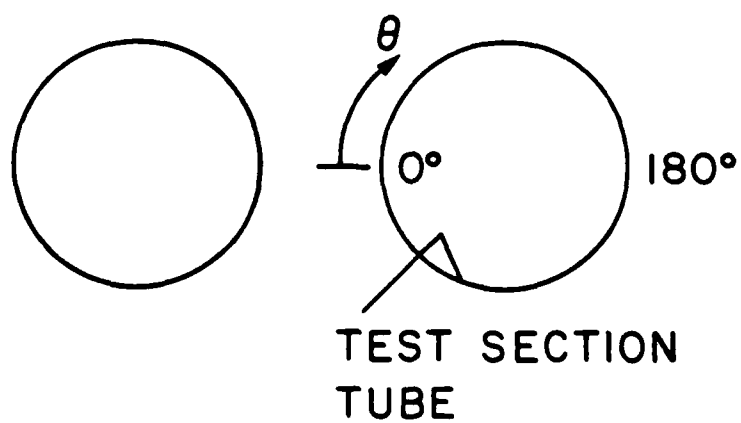
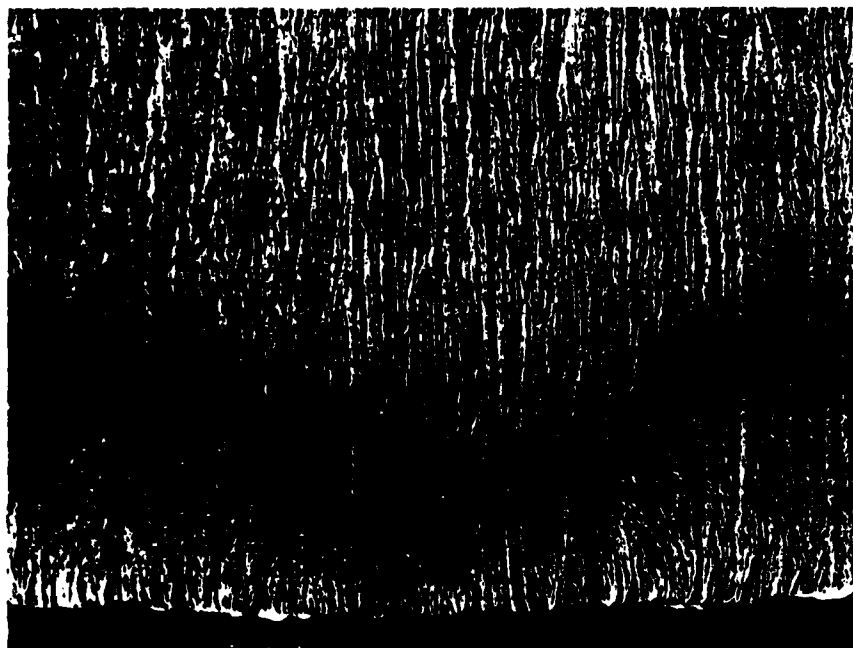


Fig. 3

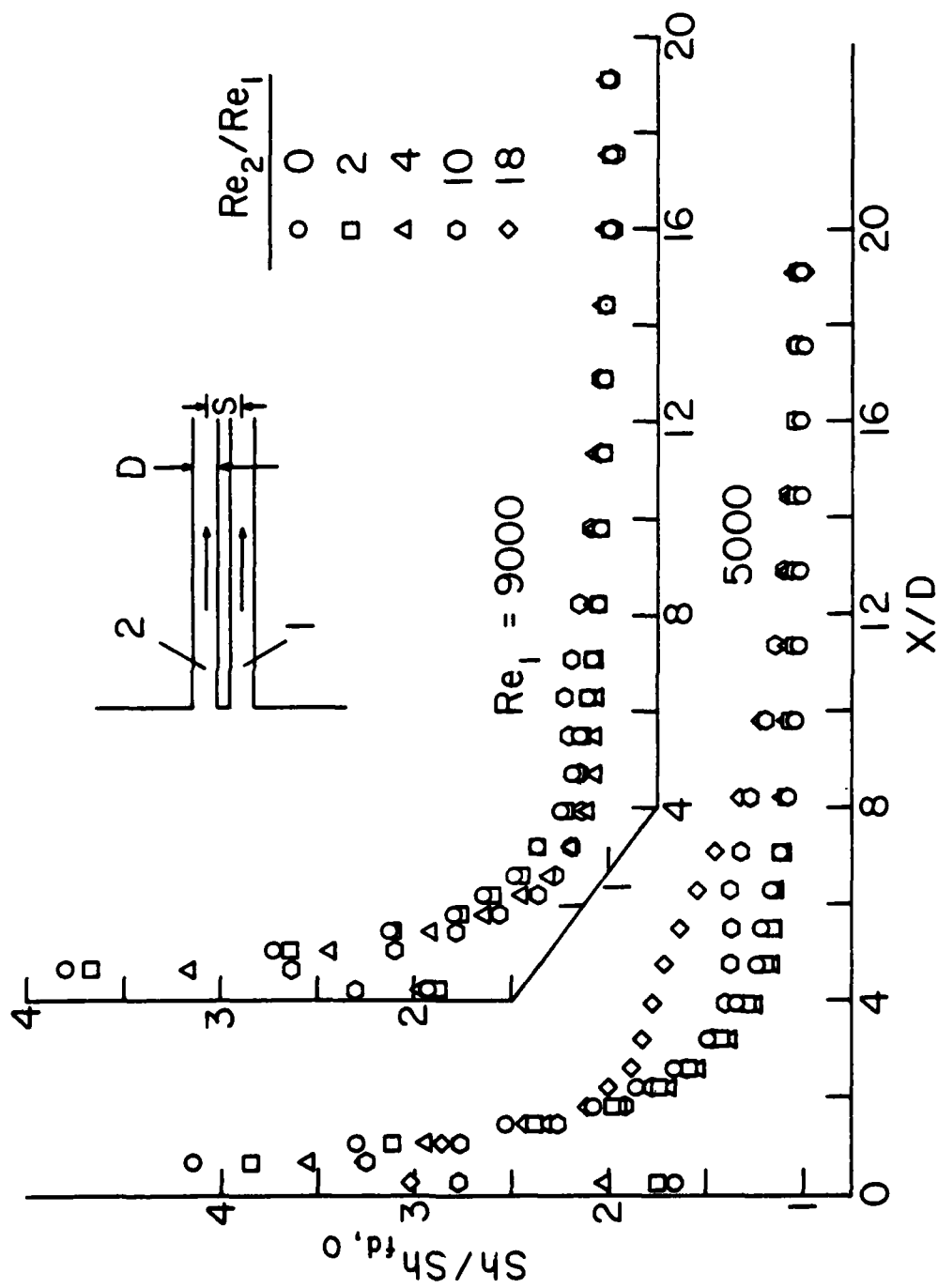


Fig. 4

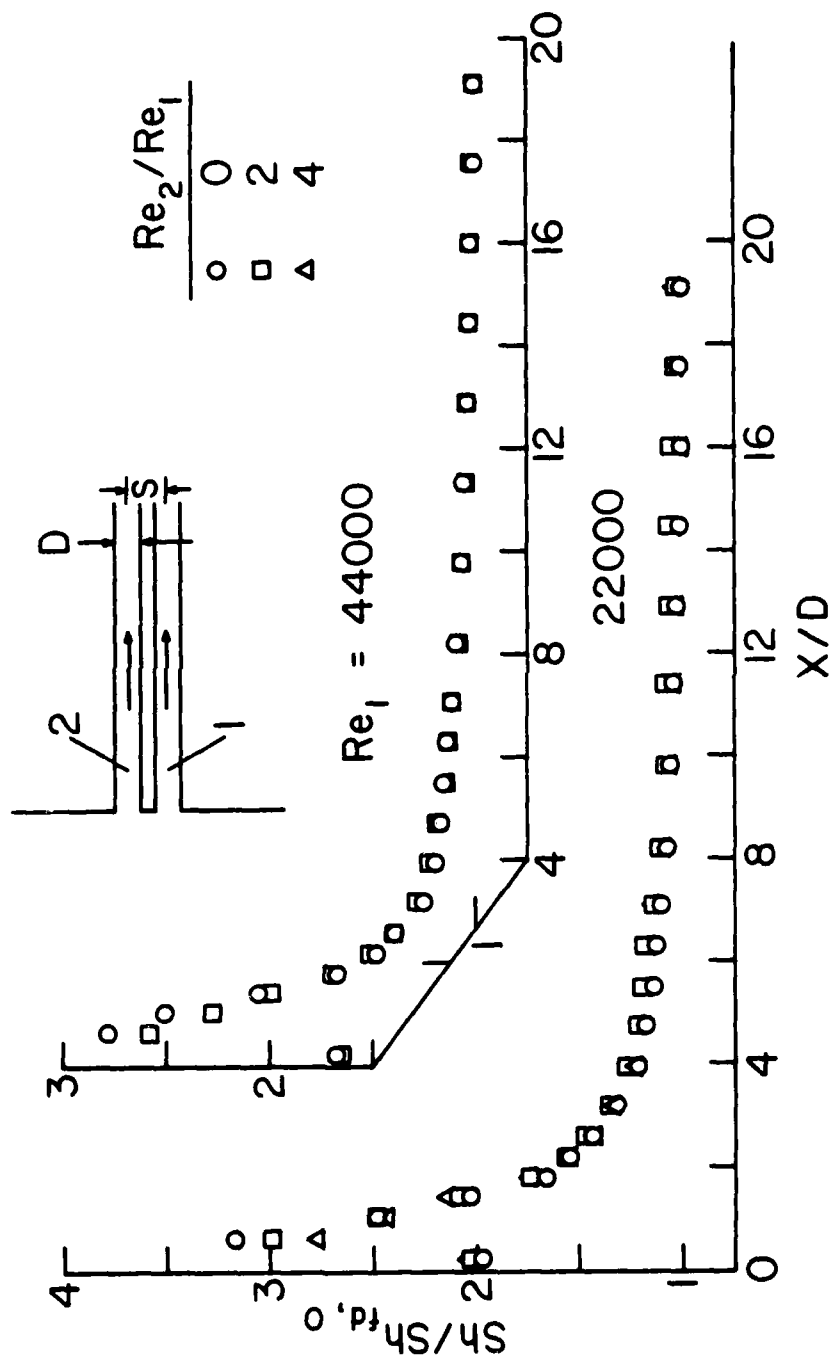


Fig. 5

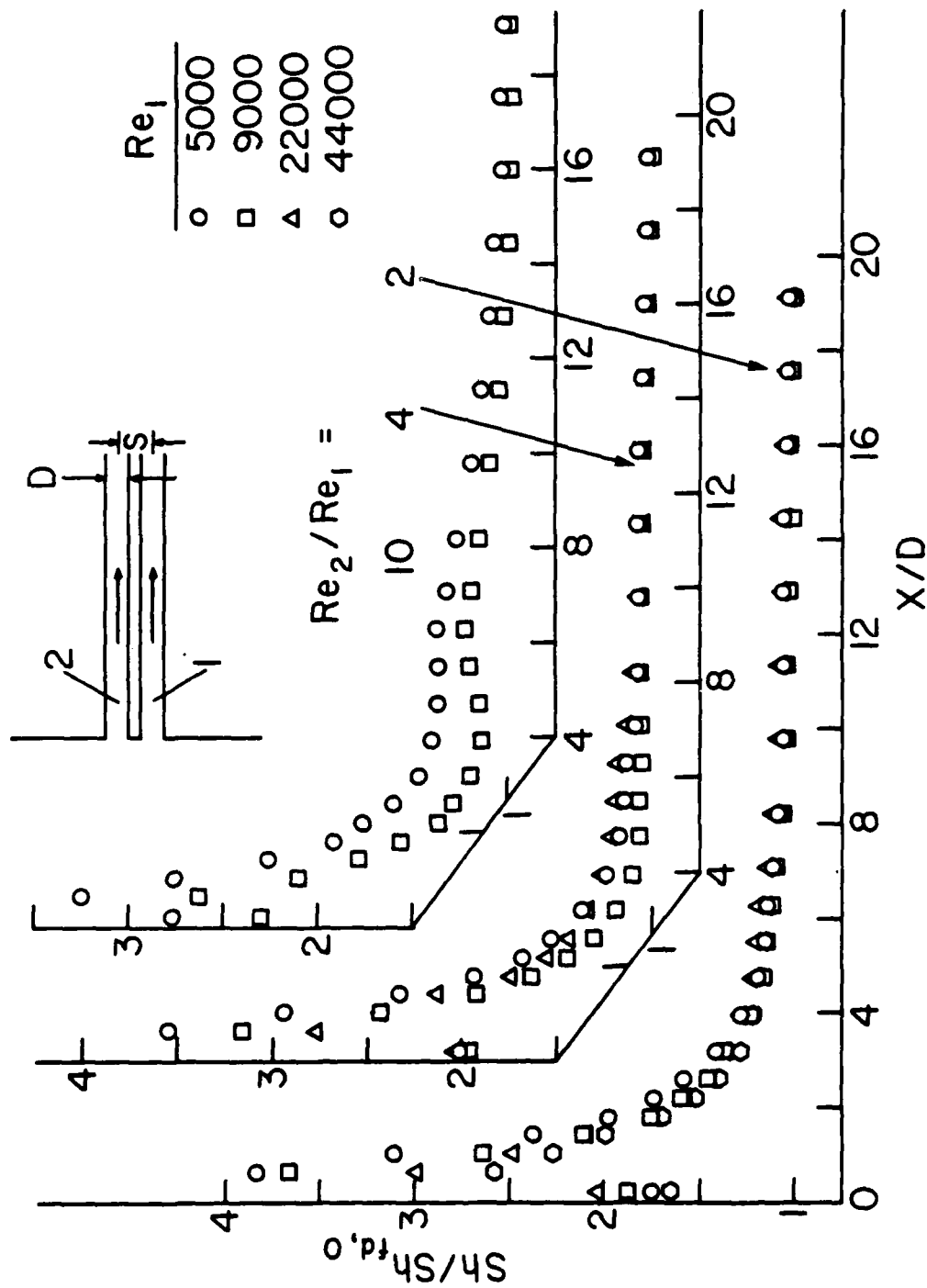


Fig. 6

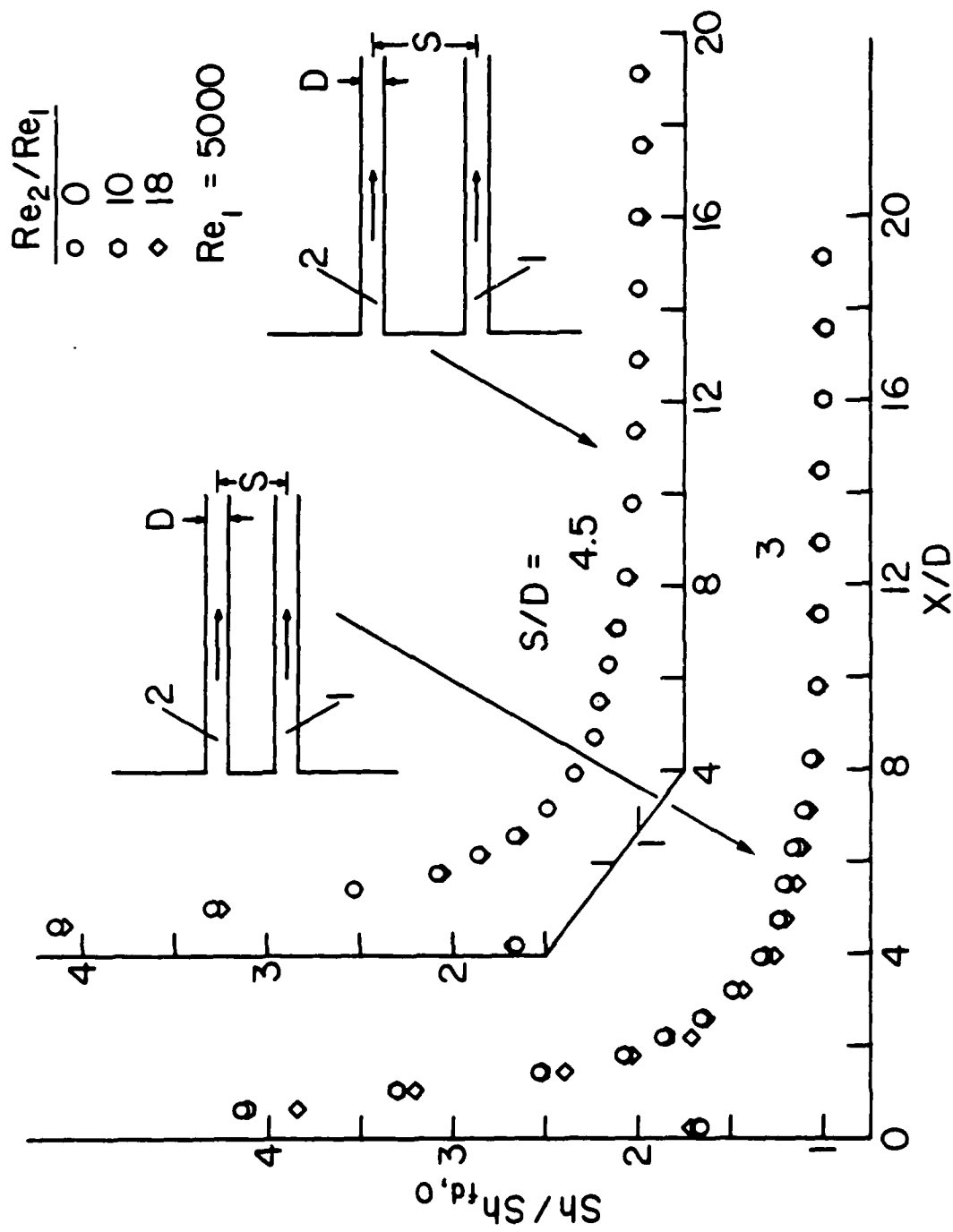


Fig. 7

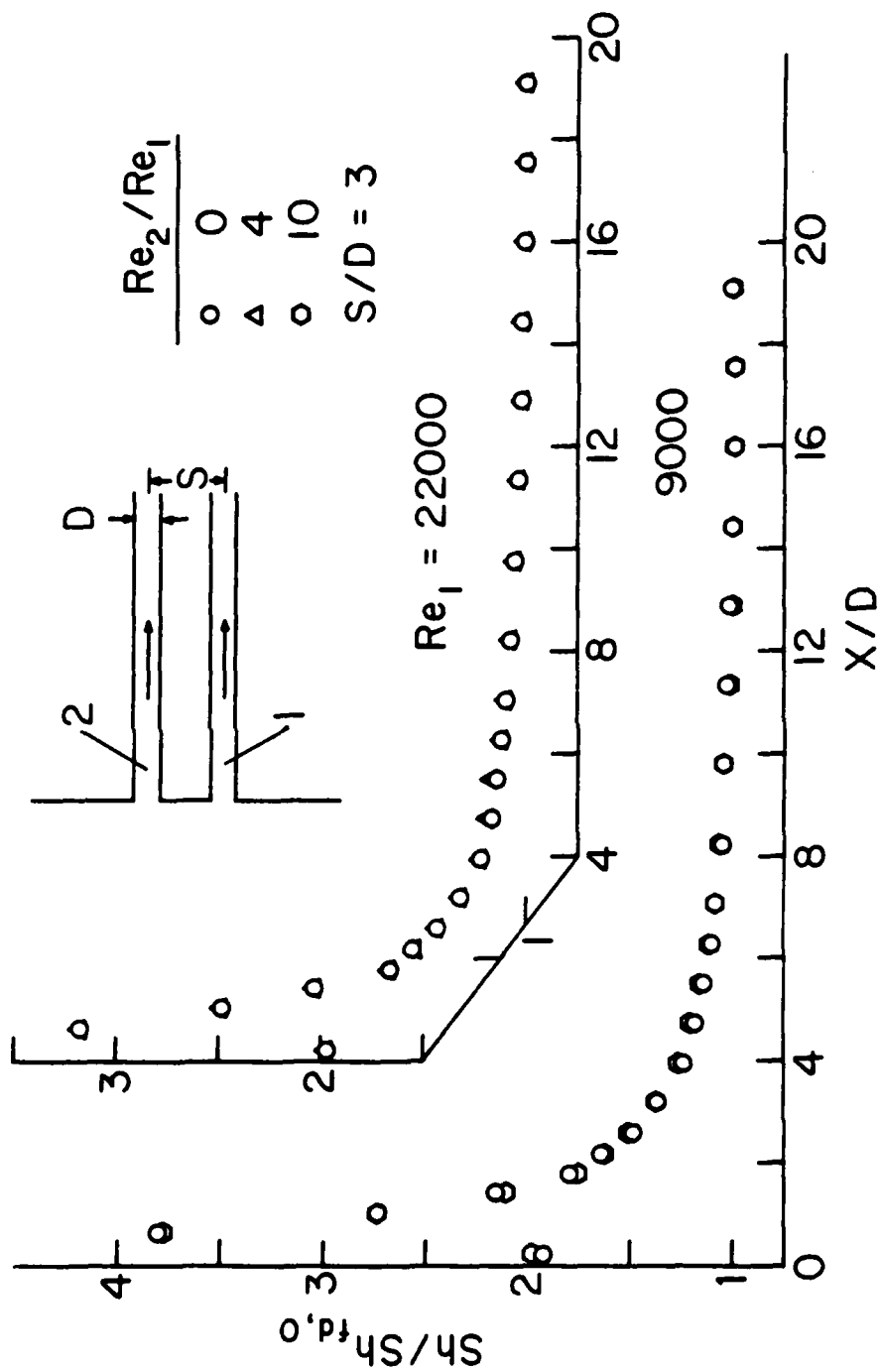


Fig. 8

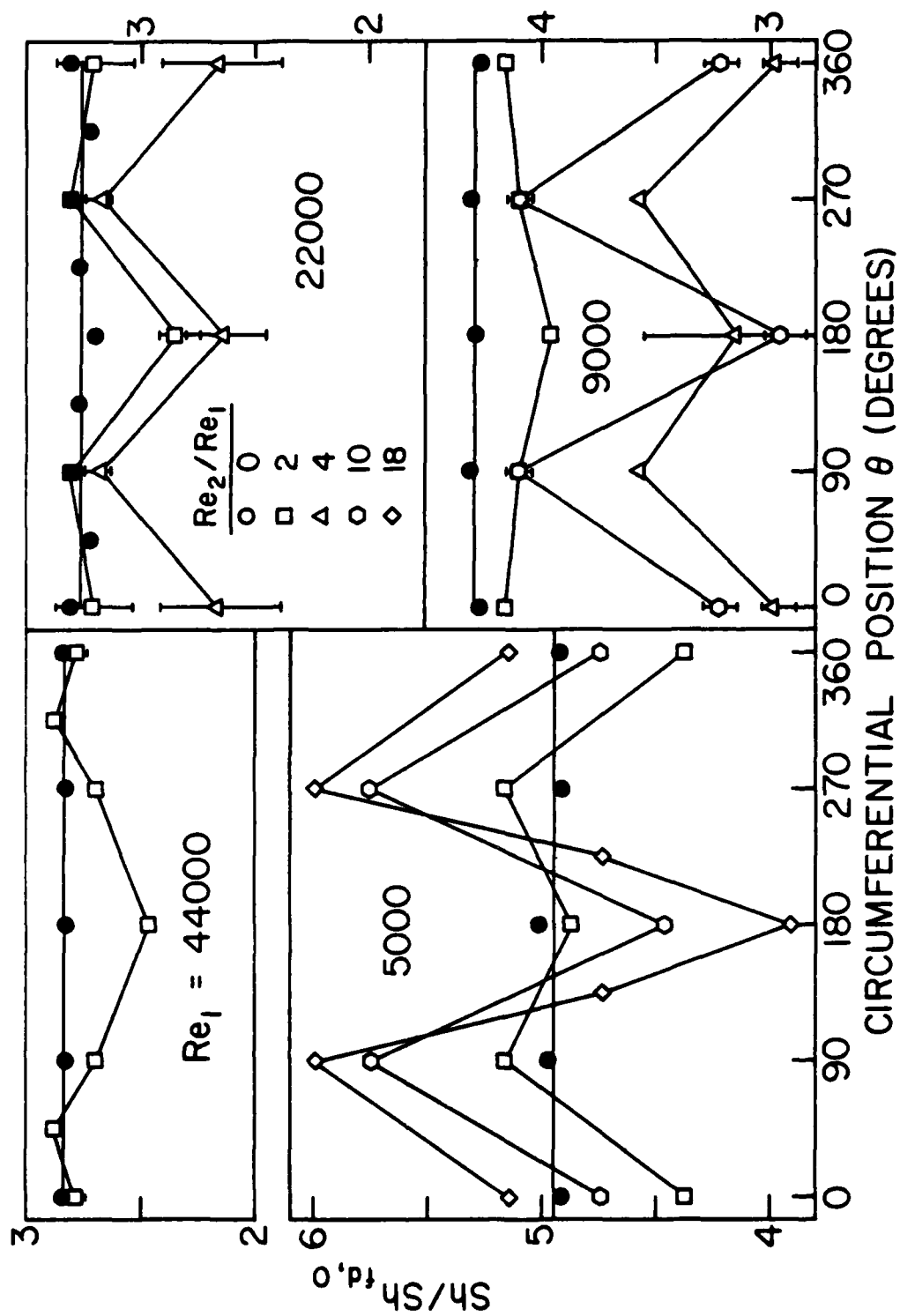


Fig. 9

MALDISTRIBUTED-INLET-FLOW EFFECTS ON TURBULENT HEAT TRANSFER
AND PRESSURE DROP IN A FLAT RECTANGULAR DUCT

ABSTRACT

The effects of flow maldistribution caused by partial blockage of the inlet of a flat rectangular duct were studied experimentally. Local heat transfer coefficients were measured on the principal walls of the duct for two blockages and for Reynolds numbers spanning the range between 6000 and 30,000. Measurements were also made of the pressure distribution along the duct, and the fluid flow pattern was visualized by the oil-lampblack technique. Large spanwise nonuniformities of the local heat transfer coefficient were induced by the maldistributed flow. These nonuniformities persisted to far downstream locations, especially in the presence of severe inlet-flow maldistributions. Spanwise-average heat transfer coefficients, evaluated from the local data, were found to be enhanced in the downstream portion of the duct due to the flow maldistribution. However, at more upstream locations, where the entering flow reattached to the duct wall following its separation at the sharp-edged inlet, the average coefficients were reduced by the presence of the maldistribution.

NOMENCLATURE

A	area of unblocked inlet
A_b	blocked area of inlet
A_i	open inlet area with blockage in place
\mathcal{D}	naphthalene-air diffusion coefficient
D_h	hydraulic diameter
H	duct height, Fig. 1
K_{xy}	local mass transfer coefficient, equation (8)

\bar{K}_x	spanwise-average mass transfer coefficient, equation (10)
\dot{M}	mass transfer rate per unit length
\dot{m}	mass transfer rate per unit area
P	duct perimeter
p	pressure
p_∞	pressure upstream of inlet
\dot{Q}	volume flow rate, \dot{w}/ρ
Re	Reynolds number, $4\dot{w}/\mu P$
Sc	Schmidt number
Sh_{xy}	local Sherwood number, $K_{xy} D_h / \mathcal{D}$
\bar{Sh}_x	spanwise-average Sherwood number, $\bar{K}_x D_h / \mathcal{D}$
V_1	velocity based on inlet cross section, equation (11)
W	duct width, Fig. 1
\dot{w}	net flow rate in forward direction
x	axial coordinate
y	transverse coordinate
δ	sublimation depth
μ	air viscosity
ν	air kinematic viscosity
ρ	mean air density
ρ_∞	air density upstream of inlet
ρ_{nb}	bulk density of naphthalene vapor
ρ_{nw}	density of naphthalene vapor at wall
ρ_s	density of solid naphthalene
τ	duration of data run

INTRODUCTION

Typically, in pipe- or duct-flow experiments, efforts are made to obtain inlet velocity distributions which either are uniform or are congruous with respect to the symmetry lines of the cross section. In practice, however, the flow supplied to the inlet cross section of a tube or duct may be highly maldistributed. This may occur when the flow is delivered to the duct via a piping system which contains bends, changes of cross section, valves, blockages, or combinations of these perturbing features.

Maldistributed flows may not only be nonuniformly and unsymmetrically distributed over the inlet cross section, but the maldistribution may set up pockets of recirculating flow (i.e., backflow) in the duct. In the presence of a maldistributed inlet flow, circumferential variations of the heat transfer coefficient are virtually a certainty, giving rise to possible hot or cold spots on the duct walls. In addition, the magnitude of the circumferential-average heat transfer coefficient may be significantly affected.

In the case of the circular tube, the heat transfer ramifications of a maldistributed inlet flow have been investigated experimentally for a variety of causal factors (e.g., bends, unsymmetrical blockages, and mixing), and {1 - 3} are representative of the available literature. On the other hand, the impact of an initial flow maldistribution on the heat transfer characteristics of rectangular ducts appears not to have been investigated heretofore. It is the purpose of this paper to report on an experimental investigation of turbulent heat transfer in a flat rectangular duct in the presence of an inlet-section flow maldistribution.

The experiments were performed with a high aspect-ratio duct (aspect ratio = 18.3) with a view toward approximating a parallel-plate channel. In planning the experimental program, it was decided to work with a severe maldistribution. To this end, the duct inlet configuration illustrated in Fig. 1 was adopted. The figure is a head-on view looking at the duct inlet from an upstream vantage point. As

seen there, the upstream portion of the duct is set into a large baffle plate such that the exposed end faces of the duct walls are flush with the upstream face of the baffle. Owing to the presence of the baffle plate and with the system operating in the suction mode, the entire space upstream of the baffle serves as a plenum from which flow is drawn into the duct inlet. The duct cross section dimensions are W and H , width and height, respectively, with $W/H = 18.3$.

The flow maldistribution was induced by positioning a thin-plate blockage element as shown schematically in Fig. 1. The presence of the blockage causes the flow entering the duct to pack to one side of the inlet cross section. Owing to the inability of the entering flow to turn sharply and fill the space downstream of the blockage, a low-velocity recirculation zone is set up. On the other hand, the flow passing through the unobstructed portion of the inlet section streams in a jet-like manner through the duct, spreading in response to wall friction and momentum exchange with the recirculation zone.

Experiments were performed for two blockage ratios, respectively $1/4$ and $1/2$ of the total cross section of the duct. The unblocked case, which can be regarded as a baseline case against which the maldistribution-affected results may be compared, was investigated earlier [4]. For each blockage ratio, experiments were carried out for four Reynolds numbers spanning the range from 6000 to 30,000.

In addition to the degree of maldistribution (blockage ratio) and the Reynolds number, the thermal boundary conditions were also varied during the course of the experiments. In one set of experiments, the two principal walls of the duct were maintained at the same uniform temperature, while in a second set one of the principal walls was isothermal and the other principal wall was adiabatic. In all of the experiments, the side walls were adiabatic.

Local heat transfer coefficients were measured at thirteen points across the span (i.e., the width) of the duct at each of twenty-one axial measuring stations. These measurements permitted the evaluation of spanwise-average heat

transfer coefficients at the twenty-one axial stations, and it is these spanwise-average results that will be compared with those for the non-maldistributed flow.

In addition to the heat transfer measurements, two types of fluid-flow-related results were obtained and will be presented. One of these is the axial pressure distributions in the presence of inlet-section blockage. The other is the pattern of fluid flow that is created in the duct due to the blockage. The oil-lamp-black technique was used for the flow visualization.

THE EXPERIMENTS

Test section. As shown in Fig. 1, the test section was made up of two principal walls which formed the upper and lower bounding surfaces of the flow cross section and of two side walls which served as spacers to separate the principal walls. These walls defined a flow cross section of width $W = 8.13$ cm (3.20 in.) and height $H = 0.445$ cm (0.175 in.), with a resulting hydraulic diameter $D_h = 0.842$ cm (0.332 in.). The wall thicknesses shown in the figure are to scale with respect to H and W . In the streamwise direction, the active length of the test section was equal to about $22D_h$.

Instead of heat transfer experiments, the experiments that were actually performed involved mass transfer. According to the analogy between the two processes (to be discussed later), the measured mass transfer coefficients can be readily converted to heat transfer coefficients. For the mass transfer studies, either one or both of the principal walls (depending on the desired boundary conditions) were recessed so as to accommodate a layer of naphthalene which was implanted by a casting process. On each plate that participated in the mass transfer process, the spanwise width of the exposed naphthalene surface was precisely equal to the duct cross-section width W . The streamwise length of the naphthalene surface was already noted in the preceding paragraph.

Two test setups were employed. In one, one of the principal walls housed a naphthalene layer which bounded the flow while the other wall was an aluminum plate

whose flow-facing surface had been carefully polished. In the other setup, the flow was bounded by naphthalene surfaces in both walls. According to the heat--mass transfer analogy, a naphthalene surface corresponds to an isothermal surface in the counterpart heat transfer experiment, while a metallic surface corresponds to an adiabatic surface. Thus, the setup where the surfaces of both principal walls were of naphthalene corresponded to a symmetrically heated channel, while the setup with only one naphthalene surface corresponded to unsymmetric heating.

The two principal walls which housed the naphthalene were each made from a solid block of aluminum. Each block was milled all the way through, removing most of the metal and leaving only an open frame-like structure and internal ribs which bridged between the frame to give it strength. Naphthalene was cast into the hollowed-out space such that the naphthalene surface exposed to the airflow was coplanar with its surrounding metal frame.

The aforementioned machining was performed so that the naphthalene surface could extend as close as possible to the duct inlet. Correspondingly, the frame at the upstream end of the test section was narrowed to 0.050 cm (0.020 in.), which corresponds to a streamwise length $\approx 0.06D_h$. This length of surface did not participate in the mass transfer process.

For each data run, a fresh naphthalene layer was cast into each of the mass-transfer-participating walls, and all portions of the casting except the surface which interfaces with the airflow were carefully taped to prevent extraneous sublimation. Upon completion of the casting procedure, the participating walls were placed in an airtight container and left overnight in the laboratory in order to attain thermal equilibrium with the room air.

For the determination of the axial pressure distribution in the duct, eight pressure taps were installed along the spanwise centerline of the aluminum plate which served as the non-participating principal wall for the unsymmetric mass transfer experiments. The locations of the taps will be evident from the pressure

distribution results to be presented later.

Other apparatus components and instrumentation. For the identification of other components, it is convenient to follow the path of the airflow through the apparatus. Air drawn from the temperature-controlled laboratory room entered the test-section duct via the partially blocked inlet. After traversing the axial length of the duct, the air encountered an abrupt enlargement (area ratio ~ 9.5) as it discharged into a long transition section whose function was to bridge between the flat rectangular cross section of the test section and the circular piping of the downstream air-handling system. The external cross-sectional dimensions of the transition section and the test section were made identical to facilitate sealing their interface against leaks.

The piping system leading from the transition section conveyed the air to a flowmeter (a calibrated rotameter), a control valve, and then to a blower situated in a service corridor adjacent to the laboratory. The naphthalene-laden blower exhaust was vented outside the building.

The baffle which framed the inlet of the duct was a 66 cm (26 in.) square aluminum plate. The 66 x 66 cm face dimensions of the baffle were chosen to be very large compared with the 8.13 x 0.445 cm dimensions of the duct cross section. Thus, the fluid flow perceives the duct inlet as an aperture in an infinite wall.

The partial blockage of the inlet was accomplished by affixing a 0.0254-cm (0.010-in.) thick stainless-steel plate to the face of the baffle by means of pressure-sensitive tape. The choice of a thin plate was made to ensure a sharply defined flow separation; the plate was sufficiently thick so as not to deform under the forces exerted by the airflow. A dial-gage-equipped caliper was used to ensure the precise positioning of the plate for the desired blockages.

The instrumentation used in the experiments will now be described. The local mass (heat) transfer coefficients were determined from measurements of the contour of the naphthalene surface made both before and after each data run. For the

contour measurements, the naphthalene test surface, housed in its metal frame, was positioned, via pins and clamps, on the bed of a coordinate table. The table permitted controlled, precisely measurable travel in two perpendicular horizontal directions, and this enabled a sensor tip, similar to that of a dial gage, to be traversed over the naphthalene surface. The vertical movements of the tip were converted to electrical signals which were read and printed out by a digital voltmeter. The final digit of the printout corresponded to 10^{-5} inches.

The outputs of the test-section pressure taps were conveyed by plastic tubing to a selector switch, the output of which was fed to the terminals of a Baratron solid-state, capacitance-type pressure meter capable of discriminating 10^{-4} mm Hg. The Baratron output was read with a digital voltmeter.

The temperature of the air entering the test section was measured by an ASTM-certified 0.1°F thermometer. In a selected number of data runs (~ 10), a calibrated copper-constantan thermocouple was cast into the naphthalene so that the thermocouple junction lay in the surface exposed to the airflow. In no case did the run-average value of the thermometer readings differ by more than 0.1°C (0.2°F) from the run-average value of the embedded thermocouple readings. This difference introduces an uncertainty of no more than one percent in the mass transfer results.

Flow visualization. As was noted in the Introduction, the flow visualization was performed using the oil-lampblack technique. According to this technique, a suitable mixture of oil and lampblack is applied to a surface, which is then exposed to the airflow whose characteristics are to be studied. Ideally, under the action of the forces exerted by the fluid, the mixture will move along the surface, following the paths of the fluid particles that pass adjacent to the surface.

Lampblack is a fine black powder which mixes readily with oil. The fluidity of the mixture can be regulated by the selection of the viscosity of the oil and by the proportions of the oil and the lampblack powder. The fluidity has a profound

effect on the extent of the resolution that can be achieved with the oil-lampblack technique. A stiff mixture will not respond to low velocities while a very fluid mixture will be blown away by a high velocity stream so that, in either of these cases, little information is obtained.

In the present instance, owing to the complexity of the flow, mixtures of different fluidities had to be used for different parts of the duct surface in order to cope with the extremes of high and low velocity. To enhance the visualization, the mixture was applied to the surface in a variety of patterns. These patterns included a sequence of dots, one or more parallel lines, or a complete coating of a specific portion of the surface.

The mixture was applied only to the lower principal wall of the duct, since sagging and dripping would have occurred had the mixture been applied to the upper principal wall. For all the visualization runs, the lower wall was covered with white, plasticized contact paper in order to provide the highest possible contrast for the black streak lines induced on the surface by the flow. Furthermore, to permit direct observation of the movement of the oil-lampblack mixture during the visualization runs, a specially fabricated plexiglass plate was used as the upper wall of the duct.

Visualization runs were performed for the same range of Reynolds numbers as that for the mass transfer runs. With the blockage in place, there were pockets of very low velocity flow. In those regions, the most fluid mixture responded very sluggishly even at the highest Reynolds number. Therefore, in order to obtain the clearest possible flow patterns for the blockage cases, all of the detailed visualization runs were made at the highest Reynolds number, namely, about 30,000.

For the presentation of the observed flow patterns, ink tracings of the streak lines were made by overlaying tracing paper atop the white contact paper used to coat the duct wall.

DATA REDUCTION

Two types of mass transfer coefficients were evaluated from the experimental measurements and will be presented in the next section of the paper. One of these is the local coefficient K_{xy} at a position x, y on the principal walls of the duct, where x is the axial coordinate (in the flow direction) and y is the spanwise coordinate (across the width W). The other is the spanwise-average coefficient \bar{K}_x at an axial station x . The dimensionless counterparts of these coefficients are the Sherwood numbers Sh_{xy} and \bar{Sh}_x , defined as

$$Sh_{xy} = K_{xy} D_h / \mathcal{D}, \quad \bar{Sh}_x = \bar{K}_x D_h / \mathcal{D} \quad (1)$$

and it is these Sherwood numbers that will be employed in the presentation of the results. In turn, these Sherwood numbers are the analogues of the Nusselt numbers Nu_{xy} and \bar{Nu}_x ,

$$Nu_{xy} = h_{xy} D_h / k, \quad \bar{Nu}_x = \bar{h}_x D_h / k \quad (2)$$

For duct flows, it is standard to employ the difference between the wall and bulk temperatures (concentrations) as the basis of the heat (mass) transfer coefficient. In conventional situations where the flow is in the forward direction at all points of the cross section (i.e., no recirculation or backflow), the evaluation of the bulk temperature (concentration) in terms of the flow rate \dot{w} and the heat (mass) added to the flowing fluid is straightforward. For instance, for mass transfer, if $\dot{M}(x)$ denotes the mass of naphthalene vapor added to the airflow per unit time and per unit axial length at x and if $\dot{Q} = \dot{w}/\rho$ is the volume flow rate of the air (ρ = air density), then

$$d\rho_{nb} = \dot{M}(x) dx / \dot{Q} \quad (3)$$

represents the increase in the bulk density (i.e., concentration) of the naphthalene vapor in an axial length dx .

When there is a backflow in a portion of the cross section, as in the present instance, equation (3), or its heat transfer counterpart, can continue to serve

as the definition of the bulk concentration (or temperature) provided that \dot{Q} is associated with the net flow rate \dot{w} in the forward direction. In the steady state, the net forward flow \dot{w} is a constant from cross section to cross section despite possible differences in the extent of the backflow. Furthermore, with ρ evaluated at the axial-mean pressure in the test section, the extreme variation of \dot{Q} along the test section was about one percent in the present experiments. Thus, \dot{Q} will be regarded as independent of x . With this, equation (3) may be integrated from $x = 0$ to $x = x$ to yield the bulk concentration of the naphthalene vapor

$$\rho_{nb}(x) = \int_0^x \dot{M}(x) dx / \dot{Q} \quad (4)$$

where the condition $\rho_{nb} = 0$ at $x = 0$ has been employed.

The determination of $\rho_{nb}(x)$ from equation (4) requires $\dot{M}(x)$ as input. The surface contour measurements made before and after a data run, when differenced, yielded the distribution of local sublimation depths $\delta(x,y)$ on each participating wall. With these, the local rates of mass transfer $\dot{m}(x,y)$ per unit time and unit surface area follow as

$$\dot{m}(x,y) = \rho_s \delta(x,y) / \tau \quad (5)$$

in which ρ_s is the density of solid naphthalene and τ is the duration of the data run. If 1 denotes the upper principal wall and 2 denotes the lower principal wall, then

$$\dot{M}_1(x) = \int_0^W \dot{m}_1(x,y) dy, \quad \dot{M}_2(x) = \int_0^W \dot{m}_2(x,y) dy \quad (6)$$

and

$$\dot{M}(x) = \dot{M}_1(x) + \dot{M}_2(x) \quad (7)$$

When both walls participated in the mass transfer process, the contributions of \dot{M}_1 and \dot{M}_2 to \dot{M} were within a few percent of each other, while when only one wall participated, either \dot{M}_1 or $\dot{M}_2 = 0$ depending on the test configuration employed.

With the foregoing as background, the evaluation of the mass transfer coefficients will now be described. For the local coefficient K_{xy}

$$K_{xy} = \dot{m}(x,y) / (\rho_{nw} - \rho_{nb}(x)) \quad (8)$$

For one participating wall, $\dot{m}(x,y)$ was taken directly from equation (5), while in the case of two participating walls

$$\dot{m}(x,y) = \frac{1}{2}(\dot{m}_1(x,y) + \dot{m}_2(x,y)) \quad (9)$$

There were occasional differences between \dot{m}_1 and \dot{m}_2 in the five percent range, but for the most part agreement was in the 2 - 3 percent range. For the spanwise-average coefficient

$$\bar{K}_x = \{\dot{M}(x)/nW\} / (\rho_{nw} - \rho_{nb}(x)) \quad (10)$$

where $\dot{M}(x)$ is from equation (7), and $n = 1$ when one wall participates in the mass transfer process and $n = 2$ when both walls participate.

The bulk vapor density ρ_{nb} that appears in equations (8) and (10) has been thoroughly discussed, but ρ_{nw} , the naphthalene density at the wall, remains to be evaluated. For this purpose, the naphthalene vapor pressure at the wall was first computed from the Sogin vapor pressure--temperature relationship {5} and, with this, ρ_{nb} was obtained from the perfect gas law.

The mass transfer coefficients from (8) and (10) were introduced into the Sherwood number definitions of equation (1). The diffusion coefficient \mathcal{D} appearing there was evaluated from the identity $\mathcal{D} = \nu/Sc$, where Sc is the Schmidt number for naphthalene diffusion in air ($= 2.5$ {5}), and ν is the kinematic viscosity of air.

Attention will now be turned to the pressure distribution measurements. For the unblocked inlet, the axial pressure distributions were linear, and the corresponding friction factors were in excellent agreement with conventional relationships. These results fulfilled expectations and need not be reported further.

The pressure distributions corresponding to the maldistributed inlet flow were dominated by inertial effects. Therefore, a pressure loss coefficient, rather than a friction factor, is more suitable for their presentation. Also, it

was found that a relatively compact presentation could be achieved using a velocity V_1 based on the actual open area A_1 of the inlet with the blockage in place, i.e.,

$$V_1 = \dot{w} / \rho_\infty A_1 \quad (11)$$

where ρ_∞ is the density of the air upstream of the inlet. With this, the pressure distributions were expressed in the form

$$(p_\infty - p(x)) / \frac{1}{2} \rho_\infty V_1^2 \quad (12)$$

with p_∞ denoting the pressure upstream of the inlet.

The results were parameterized by the Reynolds number defined in the standard manner for a rectangular duct

$$Re = 4\dot{w} / \mu P \quad (13)$$

where P , the perimeter, is equal to $(2W + 2H)$.

RESULTS AND DISCUSSION

The presentation of results will begin with the flow visualization patterns, then goes on to the local and spanwise-average heat transfer coefficients, and then concludes with the pressure distributions.

Fluid flow patterns. The first case for which results are to be presented is that in which there is no blockage. In this case, the flow passes through a sharp-edged inlet as it enters the duct. Owing to its inability to turn the sharp corner at the inlet, the flow separates from the duct wall. Within the separation bubbles that are formed adjacent to each principal wall, the flow recirculates such that the fluid adjacent to the wall moves upstream, opposite to the mainflow direction. Downstream of the separation bubble, the flow reattaches to the wall.

These events are chronicled in the representative oil-lampblack pattern that is shown in Fig. 2, which is a plan view looking down at the lower wall of the duct. Two horizontal black bands can be seen in the figure. The sharply defined narrow band marks the reattachment of the separated flow, and the separated region and its recirculating flow are located fore of the reattachment. The array of

short vertical lines that populate the separated region are lines of backflow (i.e., opposite to the mainflow direction). The backflow lines terminate in a broad black band situated immediately adjacent to the duct inlet. This black band is the result of an accumulation of the oil-lampblack mixture that was pushed toward the inlet by the backflow.

It is noteworthy that the reattachment line is, for the most part, straight and parallel to the duct inlet--indicating that the separation is two-dimensional over most of the duct width. However, near the inlet and adjacent to the side walls, there is clear evidence of three-dimensional motions.

Attention may now be directed to Fig. 3, which shows, respectively at the left and at the right, the flow visualization patterns corresponding to the $\frac{1}{4}$ and $\frac{1}{2}$ blocked inlets. In both cases, the blockage is situated at the left side of the duct inlet. The flow which passes through the unblocked portion of the inlet creates an inlet-adjacent visualization pattern identical to that already discussed in connection with Fig. 2, and no further elaboration is needed. The novel features of Fig. 3 relate, therefore, to the presence of the blockage.

Behind the blockage and over a substantial distance downstream of it, the velocities are very low and a well-defined recirculation loop is not in evidence. Rather, the expected recirculating eddy with its clearly defined eye is situated farther downstream. In the case of the $\frac{1}{4}$ blockage, the eddy appears to have closed well ahead of the downstream end of the duct and a fully forward flow, albeit not necessarily fully developed, appears to have been established. For the $\frac{1}{2}$ blockage case, the eye of the eddy is positioned forward of the exit section, but the entire eddy has not closed. In neither case is there a tendency for the entering flow to spread rapidly into the space behind the blockage.

The ramifications of these fluid flow events will be evident during the presentation of the heat transfer and pressure drop results.

Heat (mass) transfer results. In view of the analogy between the two

processes, the phrases heat transfer and mass transfer will be used interchangeably during the forthcoming presentation. Attention will first be focused on the local mass (heat) transfer coefficients. Journal space limitations permit only a representative sample of the total collection of local-coefficient results to be presented here, but the full complement of results is available in {6}.

Figure 4 conveys distributions of the local Sherwood number for the case of the $\frac{1}{4}$ blockage with mass transfer at both principal walls. The figure consists of eight graphs, each of which corresponds to a specific axial station starting with the first measurement station $x/D_h = 0.22$ and ending with the last measurement station $x/D_h = 20.91$. These eight stations were selected from among the twenty-one measurement stations at which data were collected.

In each graph, the local Sherwood number Sh_{xy} is plotted as a function of the dimensionless spanwise coordinate y/W . The graphs are arranged in two columns. Atop each column, a line has been drawn to indicate the range of y/W that is spanned by the inlet-section blockage. Data are plotted for $Re = 6000$ and $30,000$, which are, respectively, the lowest and highest Reynolds numbers investigated. Lines have been faired through the data to provide continuity.

Inspection of Fig. 4 reveals that marked spanwise variations in the heat transfer coefficient are engendered by the maldistributed inlet flow and that residuals of the variations persist even to the downstream end of the duct. The flow which streams through the unblocked portion of the inlet creates, at axial stations corresponding to small and intermediate x/D_h , a heat-transfer-coefficient plateau whose level is very much higher than that of the coefficients in the low-velocity region behind the blockage. Indeed, the behind-the-blockage coefficients are a small fraction of the coefficients encountered in any other portion of the duct.

Detectable increases in the level of the low coefficients begin to appear at $x/D_h \sim 2$, and these increases continue at larger x/D_h as the mainflow tends to

occupy more and more of the duct width and as the more vigorous part of the recirculation eddy is encountered (see Fig. 3). Meanwhile, in this same range of x/D_h , the level of the high plateau decreases slowly in response to the spreading of the mainflow.

At the last measuring station ($x/D_h = 20.91$), although the flow is in the forward direction at all points in the cross section (Fig. 3), velocity and temperature profile nonuniformities persist and yield a nonuniform distribution of the heat transfer coefficient. This is especially true for the higher Reynolds number ($Re = 30,000$), where the ratio of the highest to the lowest of the plotted transfer coefficients is almost 1.4.

A detailed examination of the results for small x/D_h reveals two special characteristics, both of which are more marked for $Re = 6000$ than for $Re = 30,000$. First, the level of the plateau created by the stream which passes through the open part of the inlet tends, at first, to rise with increasing x/D_h and, after the attainment of a maximum, decreases. This behavior is due to the flow separation and reattachment induced by the sharp-edged inlet, whereby the maximum occurs when the flow reattaches.

The second special feature is the peak in the spanwise distributions that is in evidence at the initial measurement stations. This peak is believed to be a manifestation of the eddies that are shed from the sharp edge of the blockage plate [7].

A presentation similar to Fig. 4, but for the $\frac{1}{2}$ -blockage case, is made in Fig. 5. Inspection of Fig. 5 reveals an overall behavior that is similar to that which was identified and discussed in the preceding paragraphs. There are, however, certain differences in detail. In particular, significant differences in the levels of the high- and low-coefficient zones persist to greater downstream distances when the $\frac{1}{2}$ blockage is in place. Thus, at the last measurement station ($x/D_h = 20.91$), the ratio between the highest and lowest coefficients is about

a factor of two in Fig. 5 compared with about 1.4 in Fig. 4. This significant spanwise variation of the heat transfer coefficient reflects the nonuniformity in the fluid flow pattern that is in evidence in the right-hand diagram of Fig. 3. Also, at certain axial stations, in the low portion of the spanwise distribution, there is a tendency for the coefficients to tip up near the side wall. This behavior may be attributed to the existence of higher recirculation velocities adjacent to the side wall than in the eye of the recirculation eddy.

The highly nonuniform local heat transfer coefficients displayed in Figs. 4 and 5 suggest that hot or cold spots will exist for certain types of heating conditions (e.g., uniform heat flux) due to the maldistributed entering flow.

Attention will now be turned to the spanwise-average mass (heat) transfer coefficients. This information is conveyed in Figs. 6 - 9, respectively for $Re = 6000, 10,000, 21,000$ and $30,000$ and for mass transfer at both principal walls. In each figure, \overline{Sh}_x is plotted as a function of the dimensionless axial coordinate x/D_h . To provide better resolution in the region just downstream of the inlet, the abscissa scale has been enlarged in the region $0 \leq x/D_h < 1$. Three sets of data are plotted in each figure corresponding to the blockage ratios 0 (no blockage), $\frac{1}{4}$, and $\frac{1}{2}$. Curves have been faired through the data for continuity.

All of the axial distributions of the Sherwood number presented in Figs. 6 - 9 share a common shape. Starting at the first measurement station, the transfer coefficients rise sharply to a maximum and then drop off, rapidly at first and then more and more gradually. In the far downstream region, the coefficients for the no-blockage case tend to a fully developed value, while those for the blockage cases continue to vary slowly.

As was noted earlier, the rise of the transfer coefficient just downstream of the inlet and the attainment of a maximum is related to the reattachment of the separated entering flow. The subsequent dropoff is the result of the hydrodynamic and thermal development processes operating on the reattached flow. There is an

overall tendency for the reattachment point (i.e., the peak of the curve) to move upstream with increasing Reynolds number, with the range of x/D_h at reattachment extending from 0.9 to 0.35. Furthermore, the sensitivity of the reattachment-point location to blockage diminishes with the Reynolds number. At the lower Reynolds numbers, the more highly blocked flow tends to reattach sooner, while for $Re = 30,000$ the reattachment-point location ($x/D_h \sim 0.35$) is about the same for all of the inlet conditions investigated.

In contrast to the reattachment-point location, the magnitude of the transfer coefficient at the reattachment peak becomes increasingly sensitive to the blockage ratio as the Reynolds number increases, with lower peaks for greater blockages. At the lowest Reynolds number ($Re = 6000$), the peaks for the three inlet conditions are about at the same level. On the other hand, for $Re = 30,000$, the peak value for the unblocked case is about 1.8 times the peak for the $\frac{1}{2}$ blockage case.

The aforementioned ordering of the peaks with blockage also holds for the distribution curves proper in the x/D_h range just upstream of reattachment and extending downstream throughout the region of rapid dropoff of the curves. In this range of axial stations, the maldistribution of the inlet flow reduces the heat transfer.

In the downstream region, say, $x/D_h > 5$, a new ordering of the results emerges. Here, the transfer coefficients increase monotonically with increasing blockage ratio. This ordering is reflective of the degree to which the various cases approach the fully developed regime--with the no-blockage case having attained complete development while the $\frac{1}{2}$ blockage case is rather far from being developed. The enhancement in the downstream coefficients due to blockage is greatest at low Reynolds numbers--about 35 percent at $x/D_h = 20$ for $Re = 6000$ and 15 percent at the same x/D_h for $Re = 30,000$.

The presentation of the mass (heat) transfer results has, thus far, been focused on the case where mass transfer occurs at both principal walls (symmetric

heat transfer). The results for the case in which only one of the walls actively participates are essentially coincident (within data scatter) with those already presented for x/D_h values up to about five and, in some instances, beyond. This is as it should be, reflecting the independence of the transfer processes at the two principal walls until the respective boundary layers have met. Thereafter, the coefficients for the unsymmetric-transfer case tend to lie below those for symmetric transfer. In the absence of blockage, the deviations are about seven percent. For the blockage cases, the deviations are less regular, ranging from two to ten percent depending on the blockage ratio and Reynolds number. This irregularity is probably reflective of the non fully developed nature of the flow and temperature fields.

Pressure distributions. As noted earlier, the pressure drop results corresponding to the unblocked inlet are in accord with the literature and need not be presented here, so that attention will be focused solely on the blockage-related pressure distributions. These results, expressed in terms of the pressure loss coefficient of equation (12), are plotted as a function of x/D_h in Fig. 10. The figure consists of four tiers of graphs, one for each of the investigated Reynolds numbers. In interpreting the results, it should be noted that decreasing values of $p(x)$ give rise to increasing values of the loss coefficient, while increasing $p(x)$ (i.e., a pressure recovery) causes the loss coefficient to decrease.

From Fig. 10, it is seen that all the pressure distributions for the $\frac{1}{4}$ blockage share a common pattern, while those for the $\frac{1}{2}$ blockage share a seemingly different common pattern. For the $\frac{1}{4}$ blockage, a slight friction-related pressure drop in the x/D_h range from five to ten is followed by a pressure recovery which results from the spreading of the mainflow (see Fig. 3). Near the downstream end of the duct, the pressure recovery is completed and friction-related pressure drop is about to take over.

The pressure distribution for the $\frac{1}{2}$ blockage case is actually a shifted and

amplified version of that for the $\frac{1}{4}$ blockage case. The small initial pressure drop for the $\frac{1}{4}$ blockage is shifted downstream and enlarged (by inertial losses) for the $\frac{1}{2}$ blockage, and a similar shift occurs for the region of pressure recovery. The duct is not sufficiently long to enable the pressure recovery to be completed for the $\frac{1}{2}$ blockage case.

CONCLUDING REMARKS

The analogy between heat and mass transfer has been firmly established on theoretical grounds for laminar flow and for turbulent flows where the eddy diffusivities for heat and mass are equal {8}. Recent empirical confirmation of the analogy for flows with separated regions has been provided by naphthalene sublimation experiments at Minnesota with cylinders and spheres in crossflow. An even more convincing demonstration that the analogy is viable in separated flows was made in naphthalene simulation experiments of a tube bank in crossflow.

In accordance with the analogy, the Sherwood number results presented in Figs. 4 - 9 and in {6} can be regarded as Nusselt numbers corresponding to a Prandtl number of 2.5 (equal to the Schmidt number for naphthalene sublimation in air). These Nusselt number results can then be employed for other Prandtl numbers using the conventional Pr^m power-law scaling, where m may be selected between $1/3$ and 0.4 .

The results presented here have demonstrated that spanwise nonuniformities in the local heat transfer coefficient induced by flow maldistribution at the inlet can persist to far downstream locations. The downstream persistence of the spanwise nonuniformities was found to be greater with a more extreme inlet-flow maldistribution. Higher spanwise-average heat transfer coefficients were encountered in the downstream region of the duct due to the flow maldistribution. However, at more upstream locations, where the entering flow reattaches to the duct wall following its separation at the sharp-edged inlet, the spanwise-average coefficients for the maldistributed flows are lower.

ACKNOWLEDGMENT

This research was performed under the auspices of the Power Program of the Office of Naval Research.

REFERENCES

1. Mills, A. F., "Experimental Investigation of Turbulent Heat Transfer in the Entrance Region of a Circular Conduit," *Journal of Mechanical Engineering Science*, Vol. 4, 1962, pp. 62-70.
2. Koram, K. K. and Sparrow, E. M., "Turbulent Heat Transfer Downstream of an Unsymmetric Blockage in a Tube," *Journal of Heat Transfer*, Vol. 100, 1978, pp. 588-594.
3. Sparrow, E. M. and Kemink, R. G., "The Effect of a Mixing Tee on Turbulent Heat Transfer in a Tube," *International Journal of Heat and Mass Transfer*, Vol. 22, 1979, pp. 909-917.
4. Sparrow, E. M. and Cur, N., "Turbulent Heat Transfer in a Symmetrically or Asymmetrically Heated Flat Rectangular Duct with Flow Separation at Inlet," *Journal of Heat Transfer*, Vol. 104, 1982, pp. 82-89.
5. Sogin, H. H., "Sublimation from Disks to Air Streams Flowing Normal to their Surfaces," *Trans. ASME*, Vol. 80, 1958, pp. 61-71.
6. Cur, N., "Local Turbulent Heat Transfer Coefficients in a Symmetrically or Asymmetrically Heated Flat Rectangular Duct with Either Uniform or Nonuniform Inlet Velocity," Ph.D. Thesis, Department of Mechanical Engineering, University of Minnesota, Minneapolis, Minnesota, 1982.
7. Beavers, G. S. and Wilson, T. A., "Vortex Growth in Jets," *Journal of Fluid Mechanics*, Vol. 44, 1970, pp. 97-112.
8. Eckert, E.R.G., "Analogies to Heat Transfer," in *Measurement Techniques in Heat Transfer*, edited by E.R.G. Eckert and R. J. Goldstein, Hemisphere Publishing, Washington, D.C., 1976.

FIGURE CAPTIONS

- Fig. 1 Duct inlet configuration
- Fig. 2 Flow visualization pattern corresponding to a blockage-free inlet ($Re = 21,000$)
- Fig. 3 Flow visualization patterns corresponding to the $\frac{1}{4}$ and $\frac{1}{2}$ inlet blockages, left- and right-hand diagrams, respectively
- Fig. 4 Spanwise and axial distributions of the local Sherwood number for the $\frac{1}{4}$ blocked inlet
- Fig. 5 Spanwise and axial distributions of the local Sherwood number for the $\frac{1}{2}$ blocked inlet
- Fig. 6 Axial distributions of the spanwise-average Sherwood number, $Re = 6000$
- Fig. 7 Axial distributions of the spanwise-average Sherwood number, $Re = 10,000$
- Fig. 8 Axial distributions of the spanwise-average Sherwood number, $Re = 21,000$
- Fig. 9 Axial distributions of the spanwise-average Sherwood number, $Re = 30,000$
- Fig. 10 Pressure distributions corresponding to the $\frac{1}{4}$ and $\frac{1}{2}$ inlet blockages

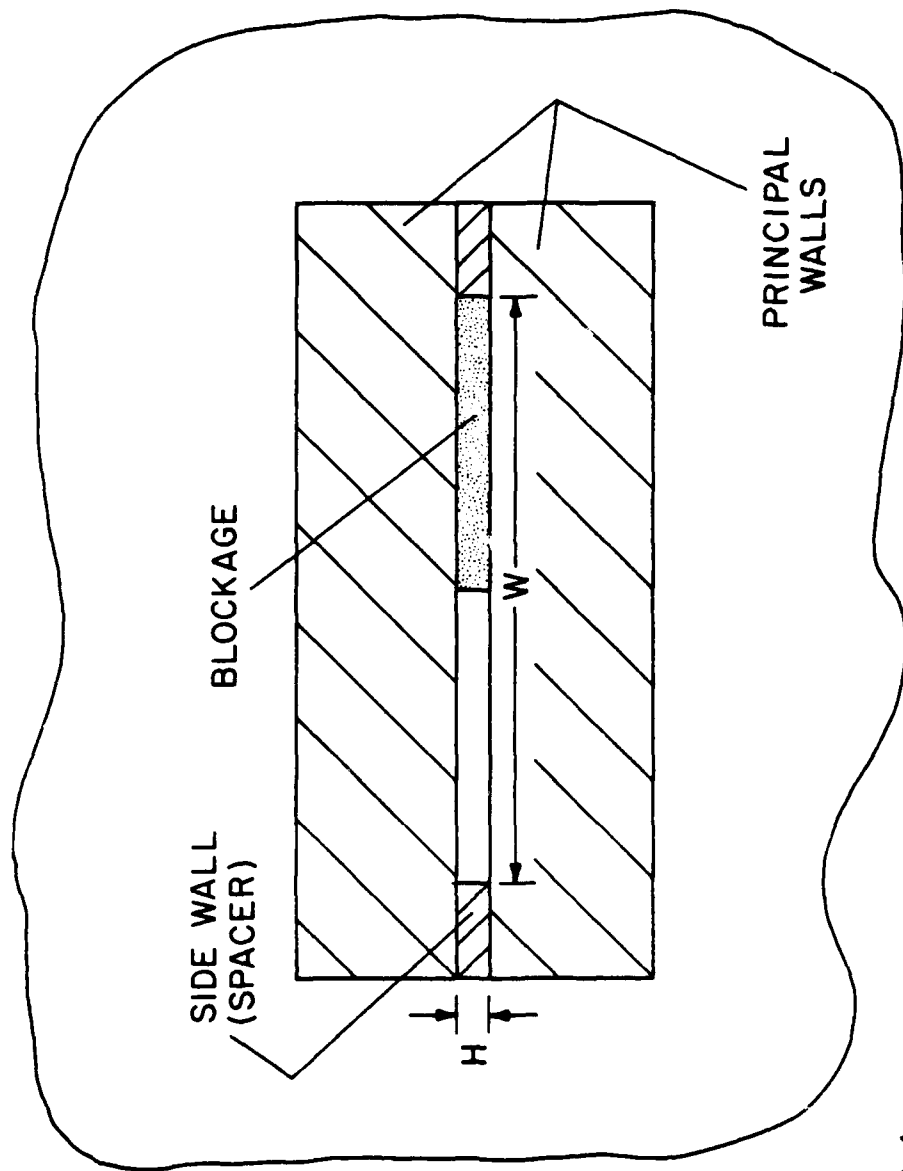


FIG. 1

AD-A124 017

STUDIES OF HEAT TRANSFER IN COMPLEX INTERNAL FLOWS(U)
MINNESOTA UNIV MINNEAPOLIS DEPT OF MECHANICAL
ENGINEERING E M SPARROW JAN 83 N00014-79-C-0621

2/2

UNCLASSIFIED

F/G 13/1

NL



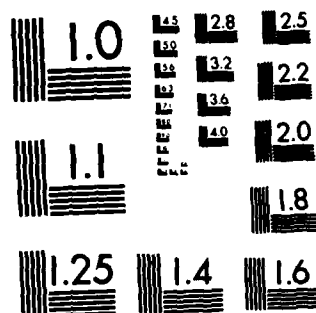
END

DATE

EXTENDED

2 83

DTIC



MICROCOPY RESOLUTION TEST CHART
NATIONAL BUREAU OF STANDARDS-1963-A

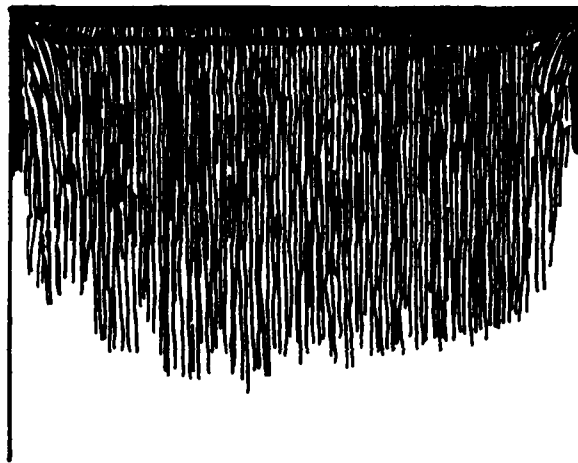


Fig. 2

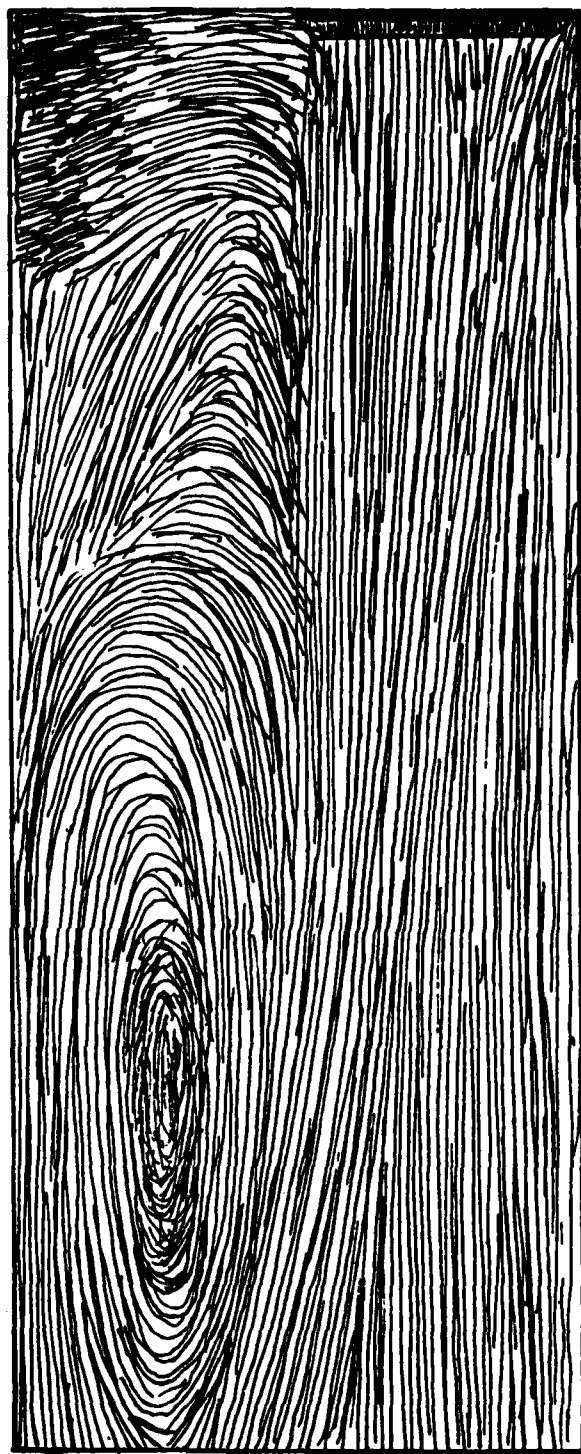
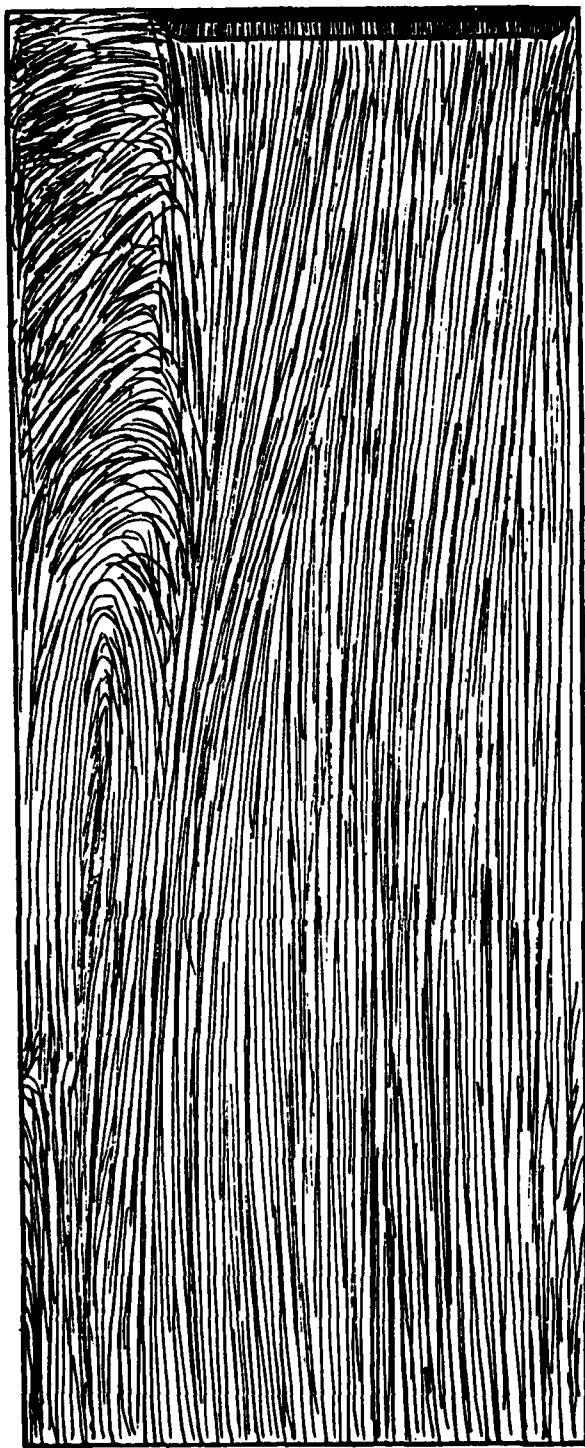


Fig. 3

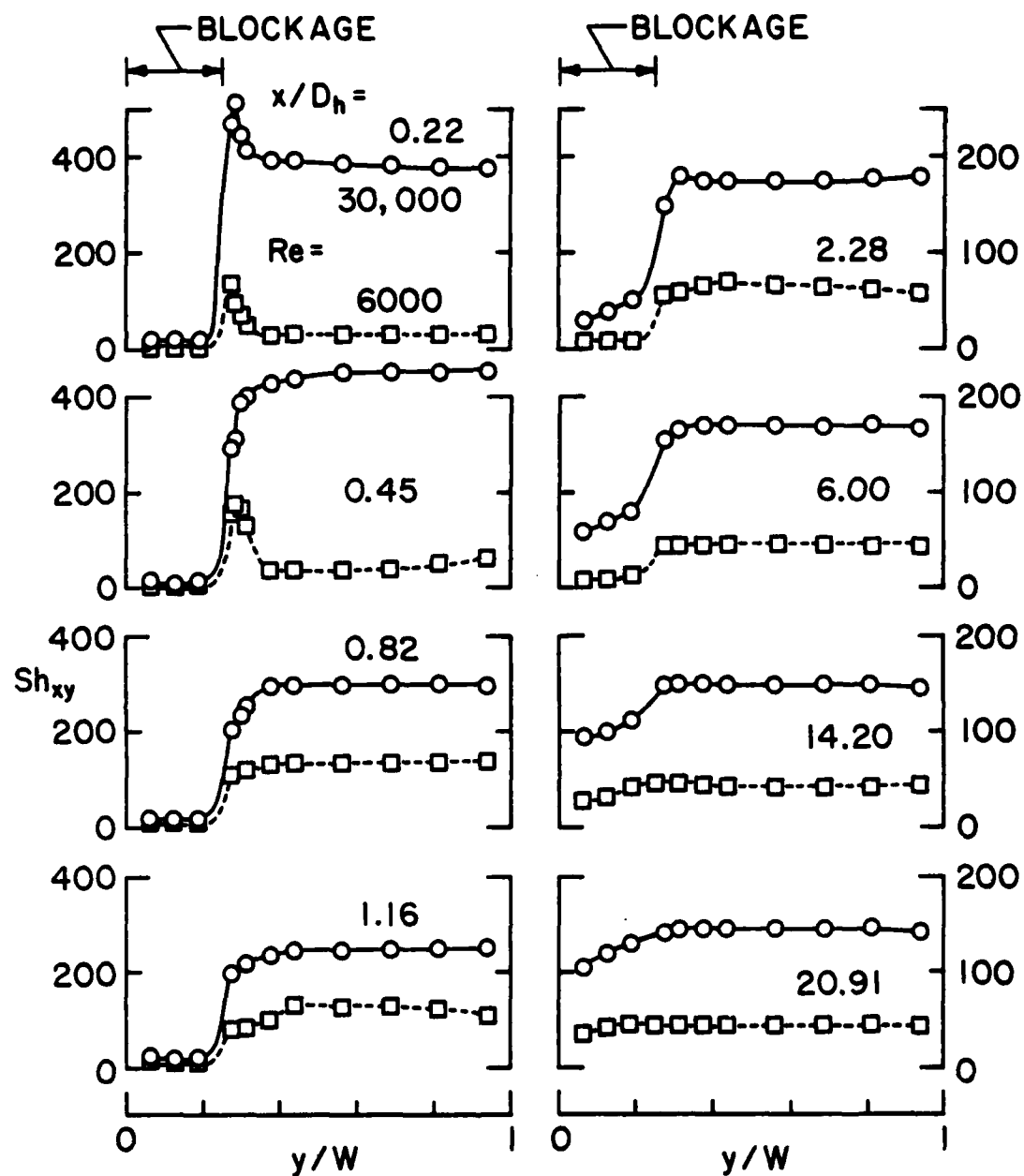


FIG. 4

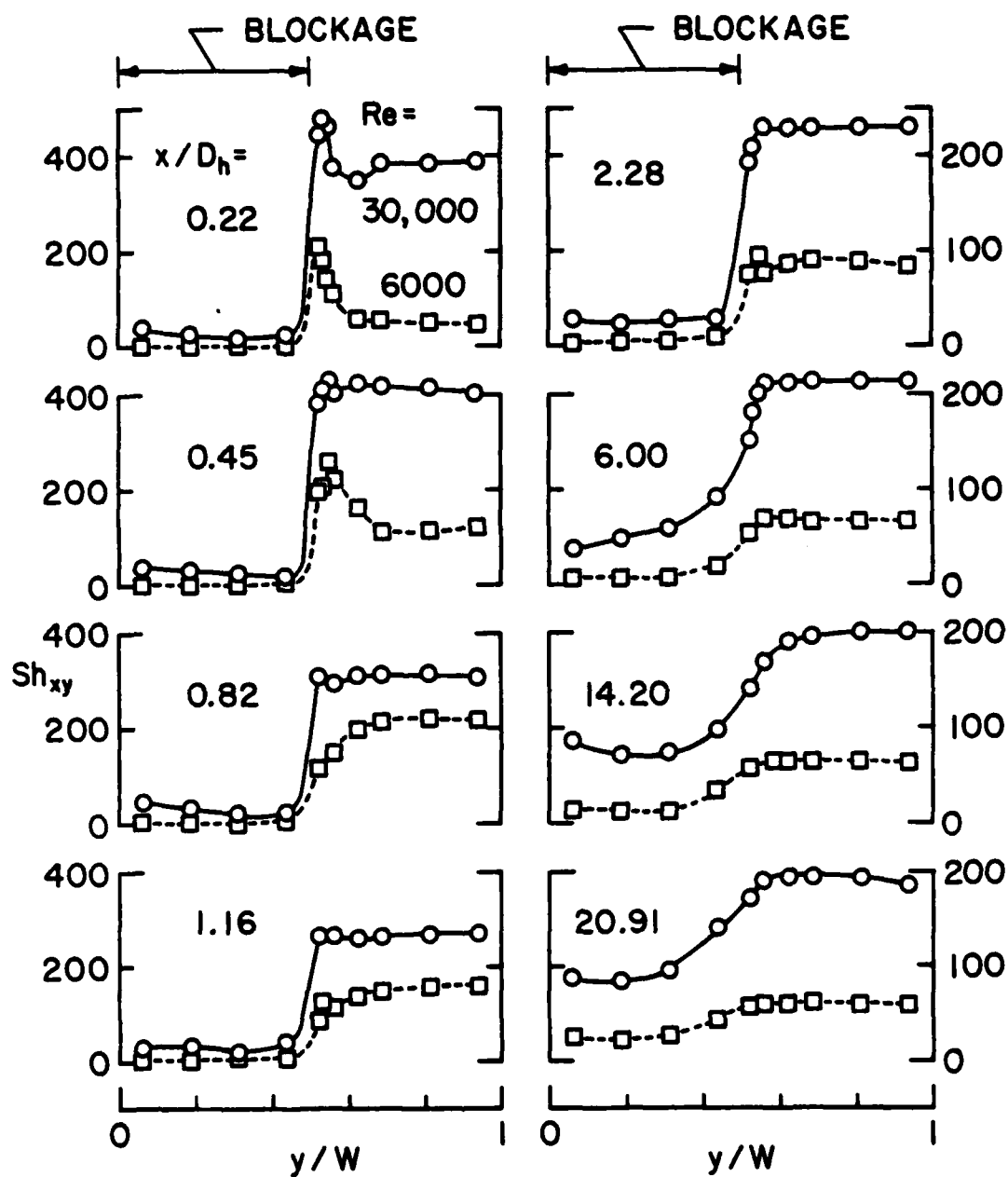


FIG. 5

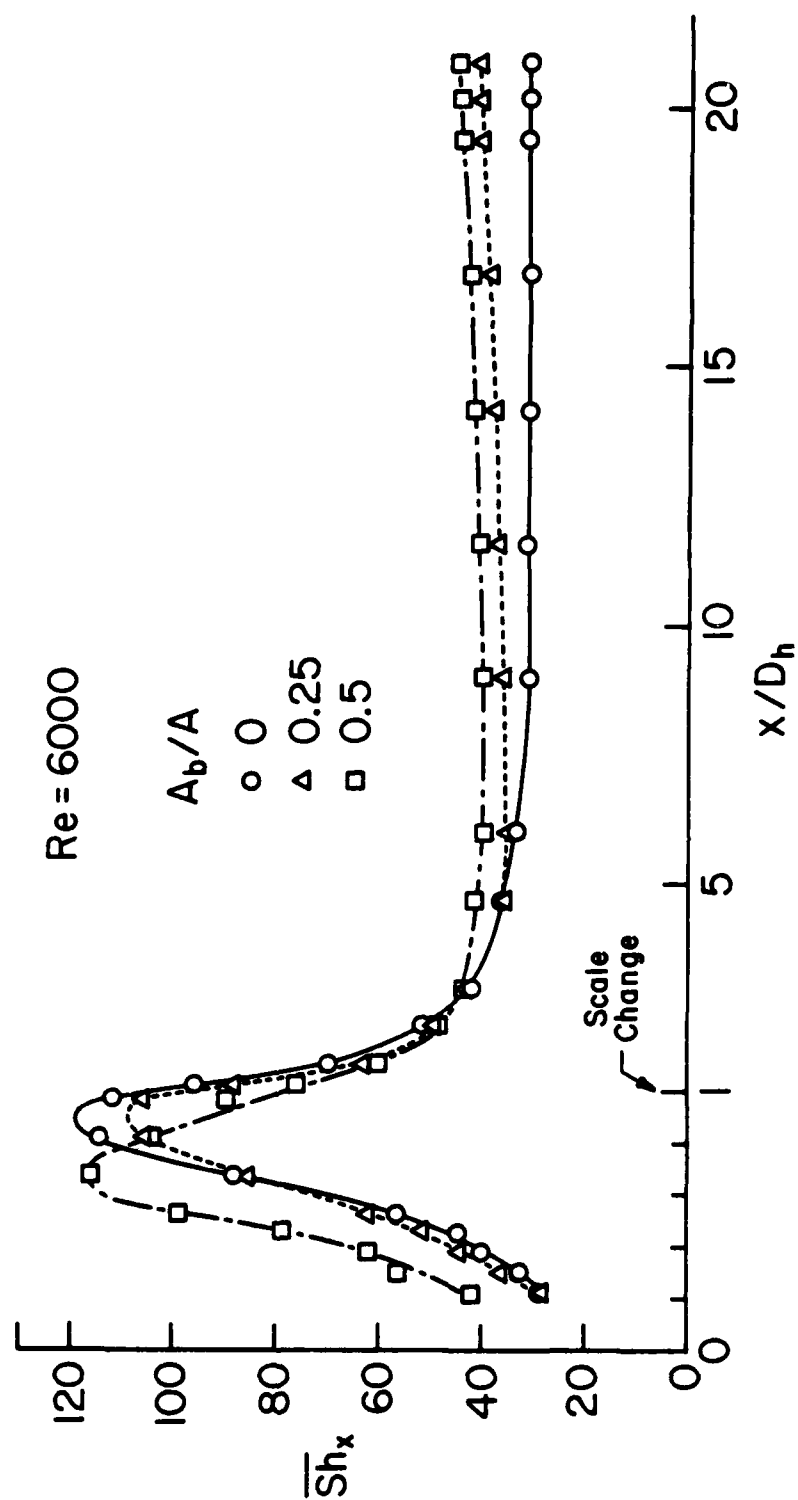


FIG. 6

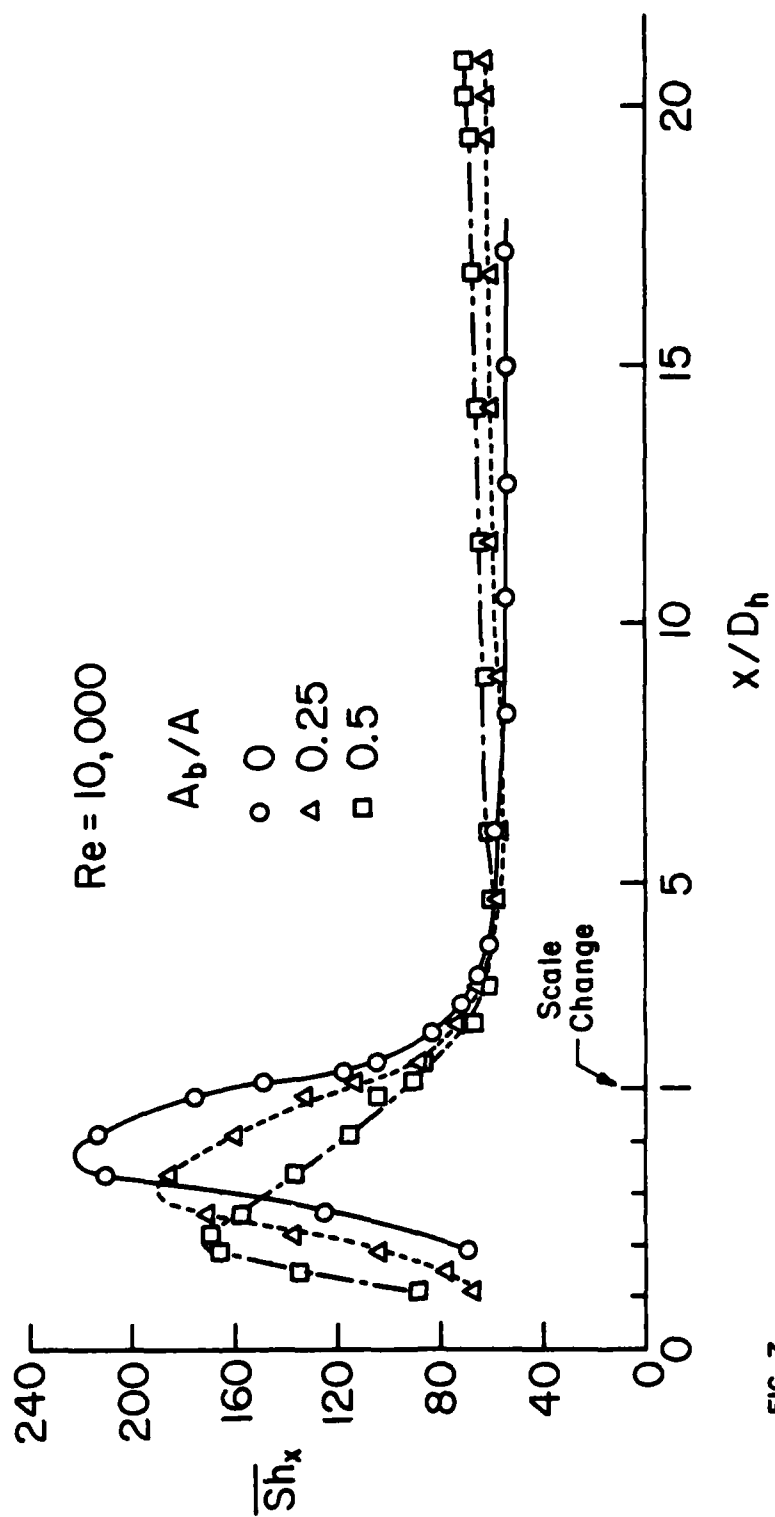


FIG. 7

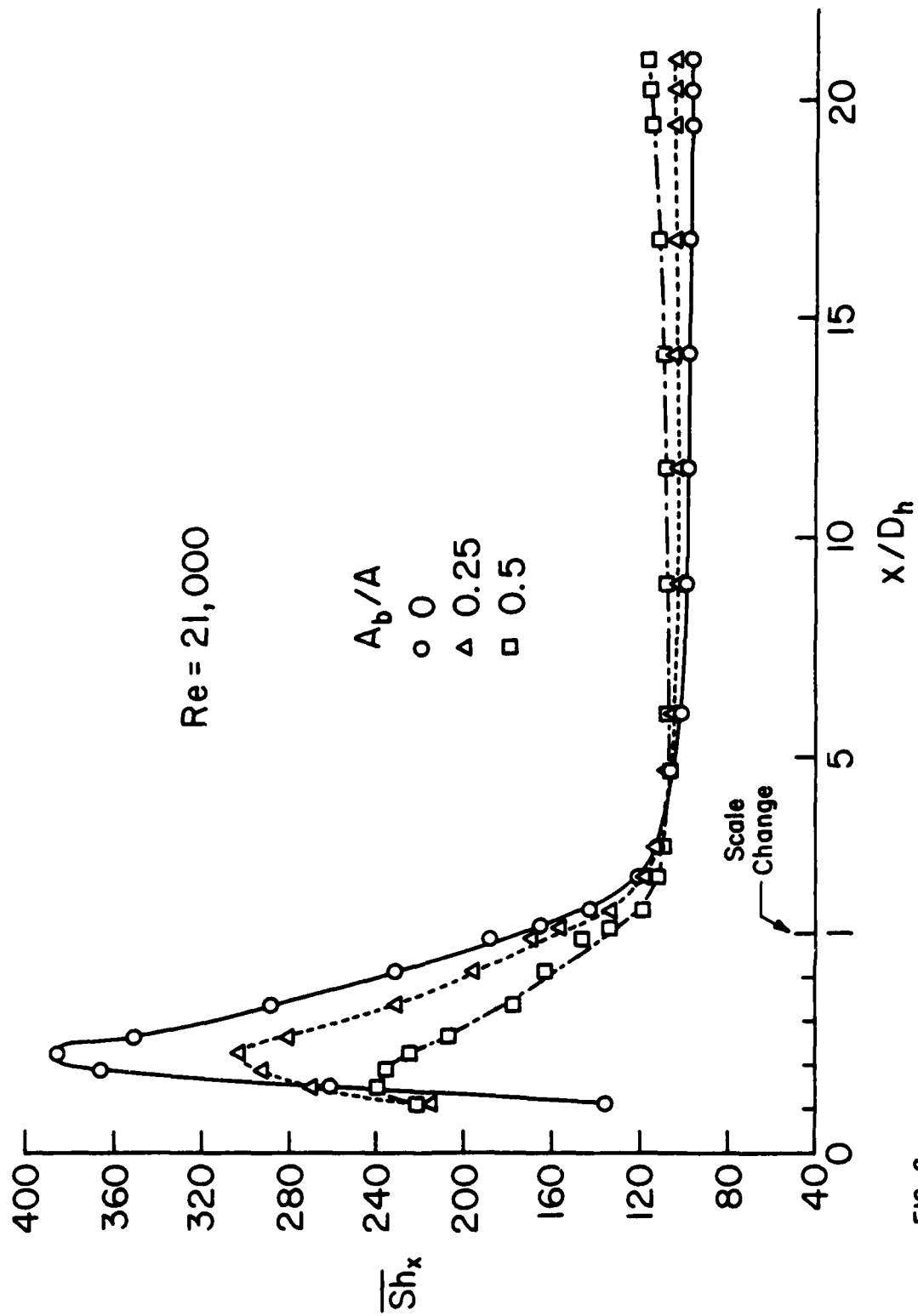


FIG. 8

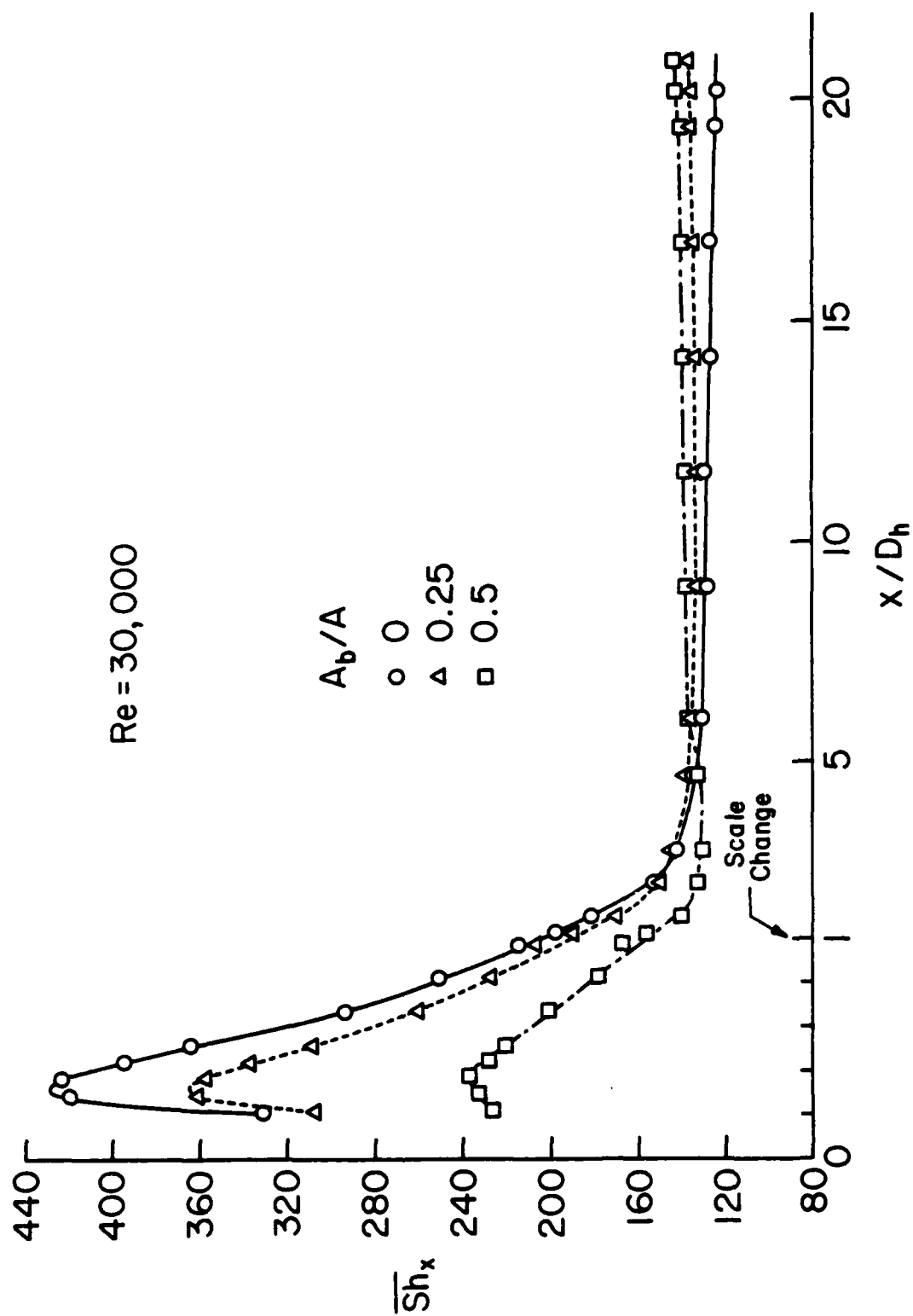


FIG. 9

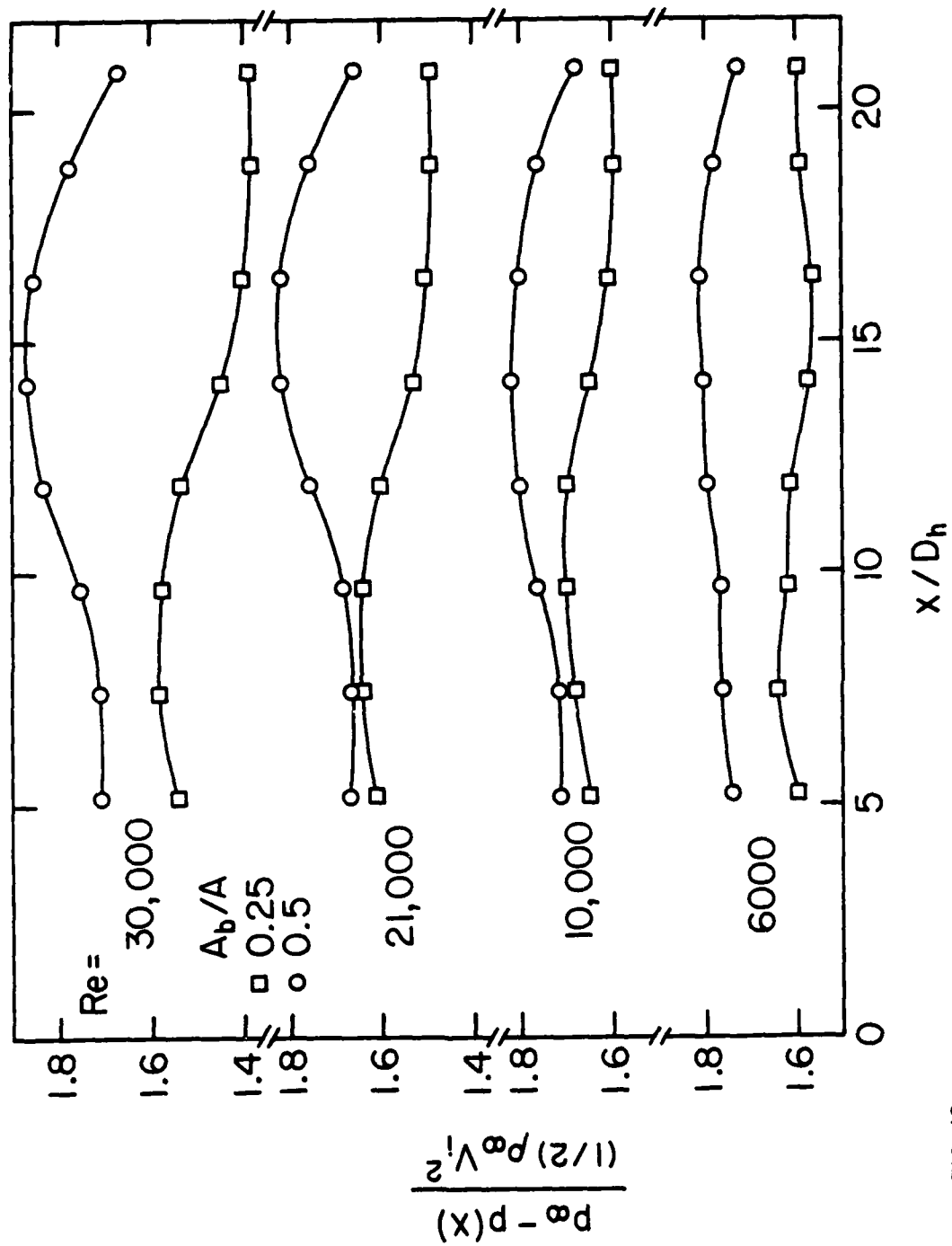


FIG. 10

DISTRIBUTION LIST

HEAT TRANSFER

One copy except
as noted

Mr. M. Keith Ellingsworth
Power Program
Office of Naval Research
800 N. Quincy Street
Arlington, VA 22203

5

Defense Documentation Center
Building 5, Cameron Station
Alexandria, VA 22314

12

Technical Information Division
Naval Research Laboratory
4555 Overlook Avenue SW
Washington, DC 20375

6

Professor Paul Marto
Department of Mechanical Engineering
US Naval Post Graduate School
Monterey, CA 93940

Professor Bruce Rankin
Naval Systems Engineering
US Naval Academy
Annapolis, MD 21402

Office of Naval Research Eastern/
Central Regional Office
Bldg 114, Section D
666 Summer Street
Boston, Massachusetts 02210

Office of Naval Research Branch Office
536 South Clark Street
Chicago, Ill. 60605

Office of Naval Research
Western Regional Office
1030 East Green Street
Pasadena, CA 91106

Mr. Charles Miller, Code 05R13
Crystal Plaza #6
Naval Sea Systems Command
Washington, DC 20362

Heat Exchanger Branch, Code 5223
National Center #3
Naval Sea Systems Command
Washington, DC 20362

Mr. Ed Ruggiero, NAVSEA 08
National Center #2
Washington, DC 20362

Dr. Earl Quandt Jr., Code 272
David Taylor Ship R&D Center
Annapolis, MD 21402

Mr. Wayne Adamson, Code 2722
David Taylor Ship R&D Center
Annapolis, MD 21402

Dr. Win Aung
Heat Transfer Program
National Science Foundation
Washington, DC 20550

Mr. Michael Perlsweig
Department of Energy
Mail Station E-178
Washington, DC 20545

Dr. W.H. Theilbahr
Chief, Energy Conservation Branch
Dept. of Energy, Idaho Operations Office
550 Second Street
Idaho Falls, Idaho 83401

Professor Ephriam M. Sparrow
Department of Mechanical Engineering
University of Minnesota
Minneapolis, Minnesota 55455

Professor J.A.C. Humphrey
Department of Mechanical Engineering
University of California, Berkeley
Berkeley, California 94720

Professor Brian Launder
Thermodynamics and Fluid Mechanics Division
University of Manchester
Institute of Science & Technology
P088 Sackville Street
Manchester M601QD England

Professor Shi-Chune Yao
Department of Mechanical Engineering
Carnegie-Mellon University
Pittsburgh, PA 15213

Professor Charles B. Watkins
Chairman, Mechanical Engineering Department
Howard University
Washington, DC 20059

Professor Adrian Bejan
Department of Mechanical Engineering
University of Colorado
Boulder, Colorado 80309

Professor Donald M. McEligot
Department of Aerospace and Mechanical Engineering
Engineering Experiment Station
University of Arizona 85721

Professor Paul A. Libby
Department of Applied Mechanics and Engineering Sciences
University of California San Diego
Post Office Box 109
La Jolla, CA 92037

Professor C. Forbes Dewey Jr.
Fluid Mechanics Laboratory
Massachusetts Institute of Technology
Cambridge, Massachusetts 02139

Professor William G. Characklis
Dept. of Civil Engineering and Engineering Mechanics
Montana State University
Bozeman, Montana 59717

Professor Ralph Webb
Department of Mechanical Engineering
Pennsylvania State University
208 Mechanical Engineering Bldg.
University Park, PA 16802

Professor Warren Rohsenow
Mechanical Engineering Department
Massachusetts Institute of Technology
77 Massachusetts Avenue
Cambridge, Massachusetts 02139

Professor A. Louis London
Mechanical Engineering Department
Bldg. 500, Room 501B
Stanford University
Stanford, CA 94305

Professor James G. Knudsen
Associate Dean, School of Engineering
Oregon State University
219 Covell Hall
Corvallis, Oregon 97331

Professor Arthur E. Bergles
Mechanical Engineering Department
Iowa State University
Ames, Iowa 50011

Professor Kenneth J. Bell
School of Chemical Engineering
Oklahoma State University
Stillwater, Oklahoma 74074

Dr. James Lorenz
Component Technology Division
Argonne National Laboratory
9700 South Cass Avenue
Argonne, Illinois 60439

Dr. David M. Eissenberg
Oak Ridge National Laboratory
P.O. Box Y, Bldg. 9204-1, MS-0
Oak Ridge, Tennessee 37830

Dr. Jerry Taborak
Technical Director
Heat Transfer Research Institute
1000 South Fremont Avenue
Alhambra, CA 91802

Dr. Simion Kuo
Chief, Energy Systems
Energy Research Laboratory
United Technology Research Center
East Hartford, Connecticut 06108

Mr. Jack Yampolsky
General Atomic Company
P.O. Box 81608
San Diego, CA 92138

Mr. Ted Carnavos
Noranda Metal Industries, Inc.
Prospect Drive
Newtown, Connecticut 06470

Dr. Ramesh K. Shah
Harrison Radiator Division
General Motors Corporation
Lockport, New York 14094

Dr. Ravi K. Sakhuja
Manager, Advanced Programs
Thermo Electron Corporation
101 First Avenue
Waltham, Massachusetts 02154

Mr. Doug Marron
Engine R&D Branch, Code 5231
NC #4
Naval Sea Systems Command
Washington, D.C. 20362
(Tel 202-692-6874)

Mr. Richard S. Carlton
Director, Engines Division, Code 523
NC #4
Naval Sea Systems Command
Washington, D.C. 20362
(Tel. 202-692-6868)

Mr. Richard F. Wyvill
Engine Design Branch, Code 5232
NC #4
Naval Sea Systems Command
Washington, D.C. 20362
(Tel 202-692-6931)

Mr. Walter Ritz
Code 033C
Naval Ships Systems Engineering Station
Philadelphia, Pennsylvania 19112
(Tel. 215-755-3841)

Dr. Simion Kuo
United Tech. Res. Center
Silver Lane
East Hartford, Conn. 06108
(Tel. 203-727-7258)

Mr. T.M. Herder
Bldg. 464-G2
General Electric Co.
1100 Western Ave.
Lynn, Massachusetts 01910
(Tel. 617-594-3360)

Mr. Ed Strain
AiResearch of Arizona
Dept. 76, Mail Stop 301-2
P.O. Box 5217
Phoenix, Arizona 85010
(Tel 602-267-2797)

Mr. Norm McIntire
Solar Turbines International
2200 Pacific Hwy.
San Diego, CA 92101
(Tel. 714-238-6527)

Mr. Robert W. Perkins
Turbotec Products, Inc.
533 Downey Drive
New Britain, Connecticut 06051

Dr. Keith E. Starner
York Division, Borg-Warner Corp.
P.O. Box 1592
York, PA 17405

Mr. Peter Wishart
C-E Power Systems
Combustion Engineering, Inc.
Windsor, Connecticut 06095

Mr. Henry W. Braum
Manager, Condenser Engineering Department
Delaval
Front Street
Florence, New Jersey 08518

Dr. Thomas Rabas
Steam Turbine-Generator Technical Operations Division
Westinghouse Electric Corporation
Lester Branch
P.O. Box 9175 N2
Philadelphia, PA 19113